Title
Satellite observations of atmosphere-ice-ocean interactions around Antarctica

Author
Adusumilli, Susheel

Publication Date
2021

UNIVERSITY OF CALIFORNIA SAN DIEGO

Satellite observations of atmosphere-ice-ocean interactions around Antarctica

A dissertation submitted in partial satisfaction
of the requirements of the degree
Doctor of Philosophy

in

Oceanography

by

Susheel Adusumilli

Committee in charge:

Helen Amanda Fricker, Chair
Adrian A. Borsa
Laurie Padman
David T. Sandwell
Fiamma Straneo
Shelley A. Wright

2021

The Dissertation of Susheel Adusumilli is approved, and it is acceptable in quality and form for publication on microfilm and electronically.

University of California San Diego

2021

TABLE OF CONTENTS

LIST OF ABBREVIATIONS

AABW	Antarctic Bottom Water
AASW	Antarctic Surface Water
AIS	Antarctic Ice Sheet
AP	Antarctic Peninsula
AR	Atmospheric River
ASL	Amundsen Sea Low
ATLAS	Advanced Topographic Laser Altimeter System
CATS	Circum-Antarctic Tidal Simulation
ERS	European Remote-Sensing Satellite
FDM	Firn Densification Model
GPS	Global Positioning System
GRACE-FO	Gravity Recovery and Climate Experiment-Follow On
GSFC	Goddard Space Flight Center
HSSW	High-Salinity Shelf Water
ICESat-2	Ice, Cloud, and land Elevation Satellite-2
IMAU	Institute for Marine and Atmospheric research Utrecht
IPCC	Intergovernmental Panel on Climate Change
IVT	Integrated Vapour Transport
IWV	Integrated Water Vapour
ISW	Ice Shelf Water
mCDW	modified Circumpolar Deep Water
mWDW	modified Weddell Deep Water
MERRA-2	Modern-Era Retrospective Analysis for Research and Applications, Version 2
MODIS	Moderate Resolution Imaging Spectroradiometer
NASA	National Aeronautics and Space Administration
OIB	Operation IceBridge
RA	Radar Altimetry
RACMO	Regional Atmospheric Climate Model
RGT	Reference Ground Track
SARIn	Synthetic Aperture Radar-Interferometric
SMB	Surface Mass Balance
SLR	Sea Level Rise
WAIS	West Antarctic Ice Sheet

LIST OF FIGURES

LIST OF TABLES

ACKNOWLEDGEMENTS

First, I would like to thank Helen Amanda Fricker, my wonderful advisor who allowed me to join her research group at Scripps. Together with my other mentors Laurie Padman, Adrian Borsa, and Fiamma Straneo, she provided me the opportunities of a lifetime. I am so glad that I was able to spend so much time with them over the past few years – every conversation, personal or professional, was insightful and illuminating. I am also grateful for the support of my committee members David Sandwell and Shelley Wright, and their enthusiasm for my work.

I am grateful for the many opportunities and resources provided by Scripps to improve all facets of my professional and personal life. In particular, I would like to thank Rob Monroe, Lauren Wood, Brittany Hook, and Chase Martin from the Scripps Communications office for supporting my research and for working to make sure that it has the highest possible impact.

Much of what I was able to learn during my PhD was from the astonishingly talented students and postdocs within the research group Helen and Fiamma have assembled at the Scripps Polar Center. I got most of what I know about altimetry from Matthew Siegfried and Fernando Paolo; science communication, policy implications, and outreach from Maya Becker and Margaret Lindeman; ice/ocean observations and modelling from Donald Slater, Cyrille Mosbeux, and Bobby Sanchez.

I am glad that I have shared my PhD journey with the fellow members of my 2015 geophysics cohort (Chloe Gustafson, Daniel Blatter, Drake Singleton, Maya, Thomas Chaparro). We had a lot of type-1/-2 fun together – although we have now moved on to a wide range of careers, I have no doubt that we have formed life-long friendships, and that there will be many reunions in our future. I am also glad that I spent a significant fraction of my working hours at Scripps in Wesley Neely's office (the Barnyard), where we had many fun conversations on every conceivable topic. 2020 was not a fun year for anyone, and I am especially grateful for the friends I was able to interact with during that time. So huge thanks to Jacob Morgan and Nick Lau, who gave me a much-needed weekly outlet through football kickabouts in the park; Ryley Hill, Hannah Peterson, and Zoe Yin, who were always up for a meet up at the park/beach; David and Wes, who were always up for a fun round of golf; and Margaret, who was always up for a walk in the neighborhood or a drink at Pannikin/the Shack.

Finally, thank you to my brother Karun for supporting my work throughout my career.

Chapter 3, in full, is a reprint of the material as it appears in the journal Geophysical Research Letters. Adusumilli, S., Fricker, H. A., Siegfried, M. R., Padman, L., Paolo, F. S., & Ligtenberg, S. R. (2018). Variable basal melt rates of Antarctic Peninsula ice shelves, 1994–2016. *Geophysical Research Letters*, 45(9), 4086-4095. The dissertation author was the primary investigator and author of this paper.

Chapter 4, in full, is a reprint of the material as it appears in the journal Nature Geoscience. Adusumilli, S., Fricker, H. A., Medley, B., Padman, L., & Siegfried, M. R. (2020). Interannual variations in meltwater input to the Southern Ocean from Antarctic ice shelves. *Nature Geoscience*, 13(9), 616-620. The dissertation author was the primary investigator and author of this paper.

Chapter 5, in full, is a reprint of the material as it appears in the journal Geophysical Research Letters. Adusumilli, S., Fish, M. A., Fricker, H. A., & Medley, B. (2021). Atmospheric river precipitation contributed to rapid increases in surface height of the West Antarctic Ice Sheet in 2019. *Geophysical Research Letters*, 48. The dissertation author was the primary investigator and author of this paper.

VITA

2014	Bachelor of Science in Physics, University of Manchester
2015	Master of Science in Mathematical Modelling and Scientific Computing, University of Oxford
2021	Ph.D. in Oceanography, Scripps Institution of Oceanography

PUBLICATIONS

Paolo, F. S., Padman, L., Fricker, H. A., **Adusumilli, S.**, Howard, S., & Siegfried, M. R. (2018). Response of Pacific-sector Antarctic ice shelves to the El Niño/Southern oscillation. *Nature geoscience*.

Adusumilli, S., Fricker, H. A., Siegfried, M. R., Padman, L., Paolo, F. S., & Ligtenberg, S. R. (2018). Variable basal melt rates of Antarctic Peninsula ice shelves, 1994–2016. *Geophysical Research Letters*.

Adusumilli, S., Borsa, A. A., Fish, M. A., McMillan, H. K., & Silverii, F. (2019). A Decade of Water Storage Changes Across the Contiguous United States from GPS and Satellite Gravity. *Geophysical Research Letters*.

Adusumilli, S., Fricker, H. A., Medley, B., Padman, L., & Siegfried, M. R. (2020). Interannual variations in meltwater input to the Southern Ocean from Antarctic ice shelves. *Nature geoscience*.

Gudmundsson, G. H., Paolo, F. S., **Adusumilli, S.**, & Fricker, H. A. (2019). Instantaneous Antarctic ice sheet mass loss driven by thinning ice shelves. *Geophysical Research Letters*.

Smith, B., Fricker, H.A., Gardner, A.S., Medley, B., Nilsson, J., Paolo, F.S., Holschuh, N., **Adusumilli, S.**, Brunt, K., Csatho, B. and Harbeck, K. (2020). Pervasive ice sheet mass loss reflects competing ocean and atmosphere processes. *Science*.

Smith, B., Fricker, H.A., Holschuh, N., Gardner, A.S., **Adusumilli, S.**, Brunt, K.M., Csatho, B., Harbeck, K., Huth, A., Neumann, T. and Nilsson, J. (2019). Land ice height-retrieval algorithm for NASA's ICESat-2 photon-counting laser altimeter. Remote Sensing of Environment, 233.

Adusumilli, S., Fish, M. A., Fricker, H. A., & Medley, B. (2021). Atmospheric River Precipitation Contributed to Rapid Increases in Surface Height of the West Antarctic Ice Sheet in 2019. *Geophysical Research Letters*.

ABSTRACT OF THE DISSERTATION

Satellite observations of atmosphere-ice-ocean interactions around Antarctica

by

Susheel Adusumilli

Doctor of Philosophy in Oceanography

University of California San Diego, 2020

Professor Helen Amanda Fricker, Chair

Ongoing increases in global sea level, projected to continue through the 21st century, have widespread impacts on coastal communities and infrastructure. Uncertainties in model projections of Antarctic Ice Sheet mass represent a major contribution to uncertainties in projected sea level rise. Many modelling studies have identified the important role of climate variability in driving ice sheet change; however, there have not been sufficient observational studies on the impact of this variability on the ice sheet.

The Antarctic Ice Sheet is vast, and remote; therefore, satellites are the only feasible instruments with which we can measure changes in ice mass. In particular, satellite radar and laser altimeter measurements of changes in ice sheet height are a valuable tool to monitor changes in mass of both grounded ice and floating ice shelves. In this dissertation, we use satellite altimetry together with other ancillary datasets to identify the influences of variability in atmospheric and oceanic conditions on ice sheet mass.

We demonstrate of how satellite radar altimetry data can be used to identify the climate drivers ice shelf change during 1994–2016 in the Antarctic Peninsula, a region that has changed rapidly during that period. In the western Antarctic Peninsula, the rates of ocean-driven basal melting exceeded values required to maintain constant mass. Extending this analysis to all Antarctic ice shelves, we find large interannual variability in the total volume flux of freshwater due to basal melting exported into the Southern Ocean, with the highest values occurring during the late 2000s from ice shelves in West Antarctica. Finally, we demonstrate how laser altimetry can be used to monitor large changes in snowfall at seasonal time scales over the grounded portion of the West Antarctic Ice Sheet during the 2019.

The results described in this dissertation together highlight the value of satellite altimetry in observing variability in ice sheet mass at seasonal to interannual time scales. We expect that they will help improve model projections of sea level rise through a better understanding of the processes driving ice sheet change, and by providing improved constraints on the current state of the atmosphere-ice-ocean system.

Chapter 1

Introduction

1.1 Motivation: the role of Antarctica in the Earth system

1.1.1 Contribution of the Antarctic Ice Sheet to global sea level rise

Global sea level has been increasing since the early 1900s (e.g., Oppenheimer et al., 2020). The largest contributions to sea level are from ocean thermal expansion (e.g., Zanna et al., 2017) and losses of land-based ice in glaciers (e.g., Zemp et al., 2019), the Greenland Ice Sheet (e.g., The IMBIE Team, 2020), and the Antarctic Ice Sheet (e.g., The IMBIE Team, 2018). Around 11% of the world's population currently live in coastal areas below 10 m of elevation, and are vulnerable to coastal flooding from sea level change (e.g., Merkens et al., 2017). There is an increasing need to develop strategies that mitigate the impact of rising sea levels on coastal communities, ecosystems, and infrastructure; for example, the city of New York was forced to initiate the implementation of an extensive coastal protection system after an extreme sea level event due to Hurricane Sandy in 2012 led to damages worth over 19 billion USD (Rosenzweig and Solecki, 2014).

Developing effective mitigation strategies for future sea level rise requires precise and accurate projections. However, projections of the 21st-century evolution of the ice sheets are highly uncertain, which translates to large uncertainties in the estimates of future rates of sea level rise that are delivered to policymakers (e.g., Oppenheimer et al., 2020). The Antarctic Ice Sheet, in particular, represents the largest source of uncertainty: a recent study on future Antarctic ice loss using a wide range of model simulations (DeConto et al., 2021) suggests a global sea-level contribution of 6 to 20 cm by 2100 under a +1.5 °C global mean warming scenario and a contribution of 5 to 45 cm under a +3°C global mean warming scenario. For context, over 150,000 California residents and 30 billion USD of property are directly impacted by flooding from a 100-year storm combined with a SLR of just 25 cm relative to the 2000 values (Barnard et al., 2019). Even modest ice sheet change, within the current best projections, therefore has severe societal consequences through both the frequency and magnitude of coastal flooding.

Unknowns in the processes driving ice gains and losses lead to high uncertainties in future projections of ice sheet change, which can be mitigated through improved observational constraints on ongoing changes. Using satellite data, we can now observe changes in the ice sheet at seasonal to decadal time scales; however, most previous studies using these data have only reported the total change that occurred over the satellite record and did not consider temporal variability. Identifying temporal variability in climate at seasonal to multidecadal time scales, and incorporating it into ice sheet models is important because variability in climate forcing amplifies uncertainty in projections of sea level rise and increases the likelihood of worse-case scenarios (Robel et al., 2019).

1.1.2 The role of Antarctic meltwater in the climate system

In addition to the future sea-level rise impacts, meltwater from Antarctic ice loss can substantially influence local and global climate and ocean processes. Changes in the production of meltwater (e.g., Jourdain et al., 2020) are not considered in the Coupled Model Intercomparison Project models, which has been shown to introduce a significant bias into the climate projections used by the IPCC (Bronselear et al., 2018). The projected increase in meltwater is expected to cool and freshen the surface of the ocean near the coast, which leads to an increase in the concentration of sea ice (e.g., Bintanja et al., 2013). However, freshening of surface waters leads to increased transport of warm water towards the continent rather than towards the surface, which can trigger feedbacks that drive further increases in melting (e.g., Bronselear et al., 2018). Variability in meltwater modulates the supply of nutrients to Antarctic continental shelf surface waters, which has a large influence on biological productivity in the Southern Ocean (e.g., Gerringa et al., 2012). As such, understanding the processes that drive ice sheet change, and ensuring their realistic representation in models, is a high priority across polar science disciplines.

1.2 Dynamics of the Antarctic Ice Sheet

1.2.1 Mass balance of the Antarctic Ice Sheet

The Antarctic Ice Sheet gains mass mostly from snowfall over its interior where the ice sheet is ‘grounded’ (i.e., the ice sheet is in contact with the bed). As the accumulated ice flows towards the coast due to gravity, some portions of the ice sheet start floating on top of the ocean; these are called ‘ice shelves’ (Figure 1). In this dissertation, the term “ice sheet” refers to the combination of grounded and floating ice. The ice sheet loses mass primarily in coastal areas due to iceberg calving at the front of ice shelves, and ocean-driven melting at the ice-shelf base.

1.2.2 Ice shelf buttressing

Ice shelves experience resistive forces through contact with their surrounding topography, which helps reduce the velocity of grounded ice flowing into them relative to the case where there is no ice shelf. This process is known as “buttressing” (e.g., Thomas, 1979; Goldberg, 2017). A reduction in ice shelf thickness or extent can lead to a decrease in buttressing and increased rates of grounded-ice flow into the ocean, adding to sea level rise (Figure 2). The impacts from reduced buttressing can be exacerbated by positive feedback mechanisms such as the marine ice sheet instability (e.g., Schoof, 2007), which can lead to rapid and sustained ice sheet retreat. The influence of ice-shelf buttressing was dramatically illustrated in the Antarctic Peninsula after the disintegration of a large fraction of Larsen B Ice Shelf in 2002, which was followed by a 2- to 6-fold increase in the speed of glaciers that were flowing to the portion of the ice shelf that collapsed (e.g., Scambos et al., 2004). In the past few decades, several ice shelves have experienced thinning (e.g., Pritchard et al., 2012; Paolo et al., 2015), and mass loss from the grounded ice sheet is highest in regions where there is ice shelf thinning downstream (Smith et al., 2020, reproduced in Figure 3). This provides further evidence for the hypothesis that reduced ice shelf buttressing has led to ongoing dynamic mass loss of grounded ice; this process has also been reproduced in modelling studies (e.g., Gudmundsson et al., 2019).

1.2.3 Drivers of ice sheet change over the past century

The highest rates of mass loss over the past few decades have been observed over the Pine Island and Thwaites Glaciers in West Antarctica (e.g., Smith et al., 2020; Figure 2). The ice shelves that these glaciers flow into have experienced thinning and reductions in extent because the rates of ocean-driven basal melting exceeded the value required to maintain constant ice shelf mass (e.g., Pritchard et al., 2012; Smith et al., 2017). Changes in basal melt rates in this sector are in part due to changes in the volume of warm circumpolar deep water (CDW) influx into the ice shelf cavities (Dutrieux et al., 2014; Nakayama et al., 2019), driven by winds over the continental shelf (e.g., Thoma et al., 2008). Changes in winds over the continental shelf primarily reflect climate variability in the tropical Pacific Ocean (Steig et al., 2012), superimposed on a longer-term trend over the last century due to anthropogenic forcing (Holland et al., 2019; reproduced in Figure 4). High rates of ice shelf thinning in the past few decades occurred during periods with anomalously strong eastward winds, hypothesised to have driven higher influx of warm CDW under ice shelf cavities; such periods are increasing in frequency due to the trend from anthropogenic forcing (Figure 4). At interannual time scales, El Niño conditions in the tropical Pacific have typically led to anomalously strong eastward winds over the continental shelf that drove increased basal melt and precipitation, while La Niña conditions led to reduced basal melt and precipitation (Dutrieux et al., 2014; Paolo et al., 2018). Therefore, changes in climate at interannual to multidecadal time scales have a major influence on the mass balance of the Antarctic Ice Sheet. Improved observational constraints on temporal variability of ice sheet change are required to identify climate drivers and to identify ways to improve model treatment of processes linking climate variability to ice sheet dynamics.

1.3 Satellite remote sensing of ice sheet change

Satellites are the only viable observational tools for measuring Antarctic-wide ice sheet change. Changes in the ice sheet are typically measured using satellite-based observations of velocity, gravity, or height. Measurements of ice velocity derived by tracking features in satellite imagery (e.g., Joughin et al., 2003) can be combined with estimates of ice thickness from airborne radar sounding to calculate ice flux (e.g., Gardner et al., 2018). The difference between the surface accumulation or runoff over any portion of the ice sheet, typically obtained from atmospheric models, and the flux of ice leaving that portion determines the regional mass imbalance. The advantage of this technique is that it can be used to estimate the dynamic contribution to mass change without additional datasets (e.g., Rignot et al., 2019). However, because of a lack of continuous observations of ice velocity and thickness, estimates of mass change covering the entire ice sheet derived using this technique are only available over basin-averaged spatial scales at annual or longer temporal sampling.

Measurements of gravity through the Gravity Recovery and Climate Experiment and its follow-on mission have been available since 2003 with a short gap during 2017–2018 (e.g., Tapley et al., 2019). These measurements can be used to estimate changes in ice mass at monthly time scales (e.g., Velicogna et al., 2019), and represent the highest temporal resolution data currently available for ice sheet wide analysis. However, they cannot be used to estimate changes in mass over the floating ice shelves, and have difficulty resolving changes over coastal areas.

Estimates of ice sheet height from satellite altimeters have been available over a large fraction of Antarctica since 1992, and three altimeters in particular (ICESat, which operated during 2003–2009, CryoSat-2, which launched in 2010 and ICESat-2,which launched in 2018) provide near complete coverage of the ice sheet. These data can be used to measure variability in the ice sheet at seasonal to decadal time scales; however, most studies that have used satellite altimetry have, with some exceptions (e.g., Paolo et al., 2018), limited analysis to the total change that occurred over the satellite record. Further details on satellite altimetry, including its strengths and weaknesses, are provided in Chapter 2.

1.4 Summary of dissertation

In this dissertation, we describe the use of satellite radar and laser altimetry data to measure temporal variability in ice sheet change between 1994 and 2020, and to identify the associated oceanic and atmospheric drivers. In Chapter 2, we describe the satellite altimeters that operated in near-polar orbits during 1994–2020 and introduce the basic data processing techniques used in our work. In Chapter 3, we combine satellite radar altimetry and airborne laser altimetry collected over ice shelves in the Antarctic Peninsula between 1994 and 2016 with models of the near-surface firn layer to identify the drivers of observed changes. We describe the techniques used to combine radar altimetry data from multiple satellite missions and to isolate the contributors to changes in ice shelf height and mass at interannual to decadal time scales. In Chapter 4, we expand these techniques to all Antarctic ice shelves, using them to estimate changes in ocean-driven basal melt rates, also at interannual to decadal time scales, between 1994 and 2018. We also develop data processing techniques to extract melt rates at high spatial resolution from CryoSat-2 radar altimetry data for the 2010–2018 period. These data provide insights into the spatial and temporal variability of freshwater fluxes into the Southern Ocean from ice-shelf melting. In Chapter 5, we used measurements of changes at the snow surface using ICESat-2 laser altimetry data to highlight the large influence of extreme precipitation on grounded ice at seasonal time scales. We focus in particular on the role of Atmospheric Rivers making landfall over the West Antarctic Ice Sheet in 2019, most of which delivered large quantities of precipitation during short time intervals. In Chapter 6, we provide a summary of the research presented in this dissertation and describe how it has contributed to our knowledge of mass balance processes of the Antarctic Ice Sheet.

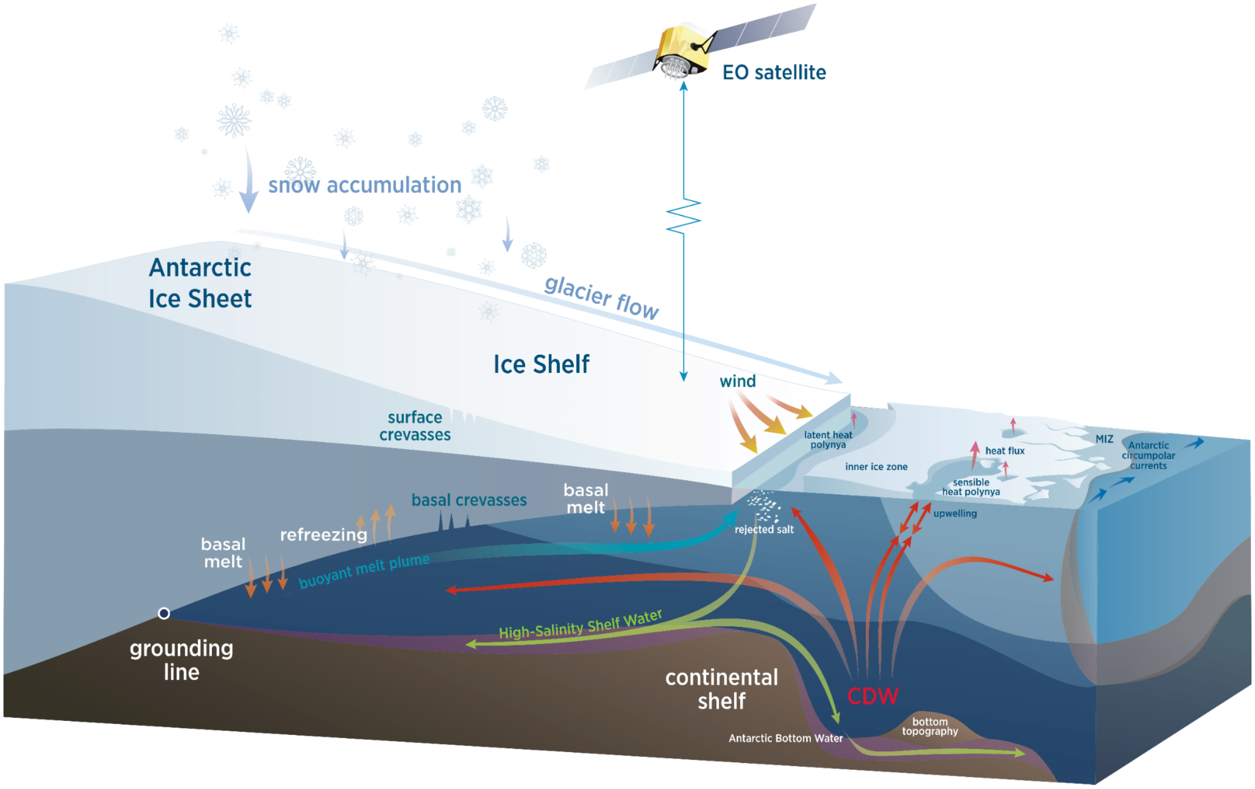

Figure 1: Schematic of the Antarctic Ice Sheet and the Southern Ocean near the coastline. The Antarctic Ice Sheet gains mass primarily from snowfall over its interior where the ice sheet is 'grounded' (i.e., the ice sheet is in contact with the bed). As the accumulated ice flows towards the coast due to gravity, some portions of the ice sheet start floating on top of the ocean; these are called 'ice shelves' (Figure 1). The ice sheet loses mass primarily in coastal areas due to iceberg calving at the front of ice shelves, and ocean-driven melting at the ice-shelf base. Changes in ice sheet mass can be estimated through observations from an earth-observing (EO) satellite. Figure by Jennifer Matthews, Scripps Institution of Oceanography.

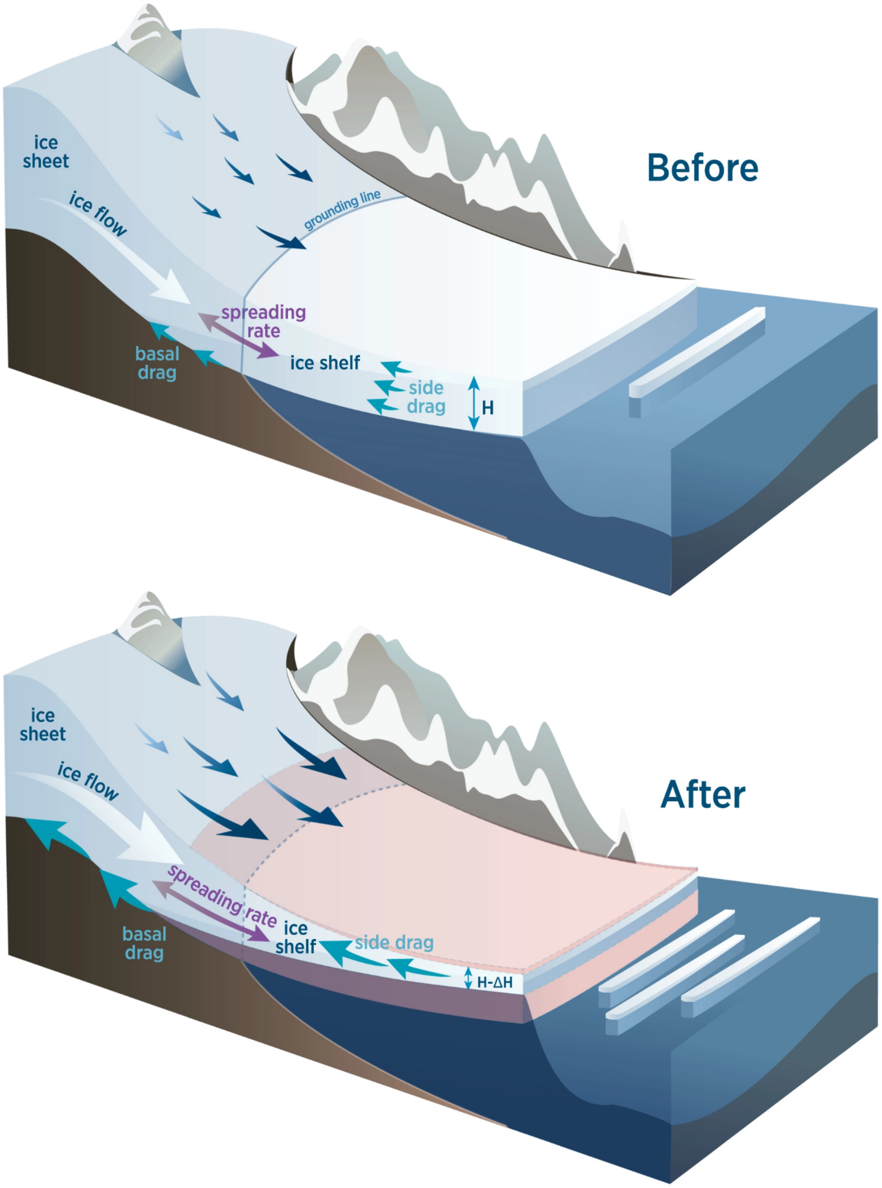

Figure 2: Reduced buttressing due to ice shelf thinning increases the rate of grounded ice discharge. Thinning of a confined ice shelf increases longitudinal stress and ice flux near the grounding line, speeding up the discharge of grounded ice into the ocean. Figure by Jennifer Matthews, Scripps Institution of Oceanography, reproduced from Gudmundsson et al., 2019.

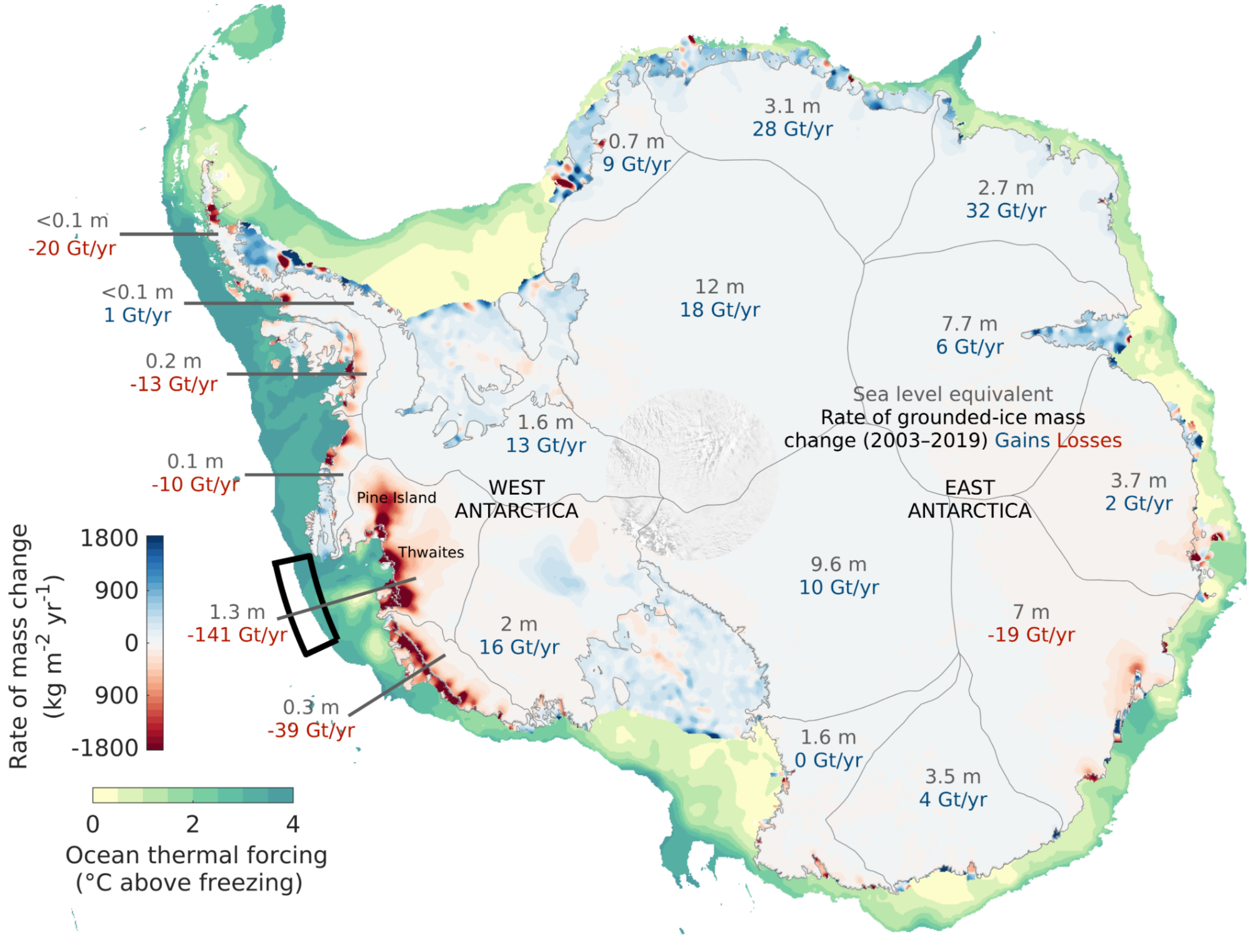

Figure 3: Rate of mass change of the Antarctic Ice Sheet during 2003–2019 (Smith et al., 2020), including integrated rate of grounded-ice mass change estimates for each basin (Mouginot et al., 2019) in Gigatons per year (Gt/y). Ocean thermal forcing (temperature above the in situ freezing point) is from Adusumilli et al., (2020). Sea level equivalents for various basins around Antarctica, representing the amount of global sea level rise if all ice were lost from the basin, are from Tinto et al., (2019). The box offshore Pine Island and Thwaites shows the location of the Pine Island/Thwaites troughs, over which we show changes in winds in Figure 4.

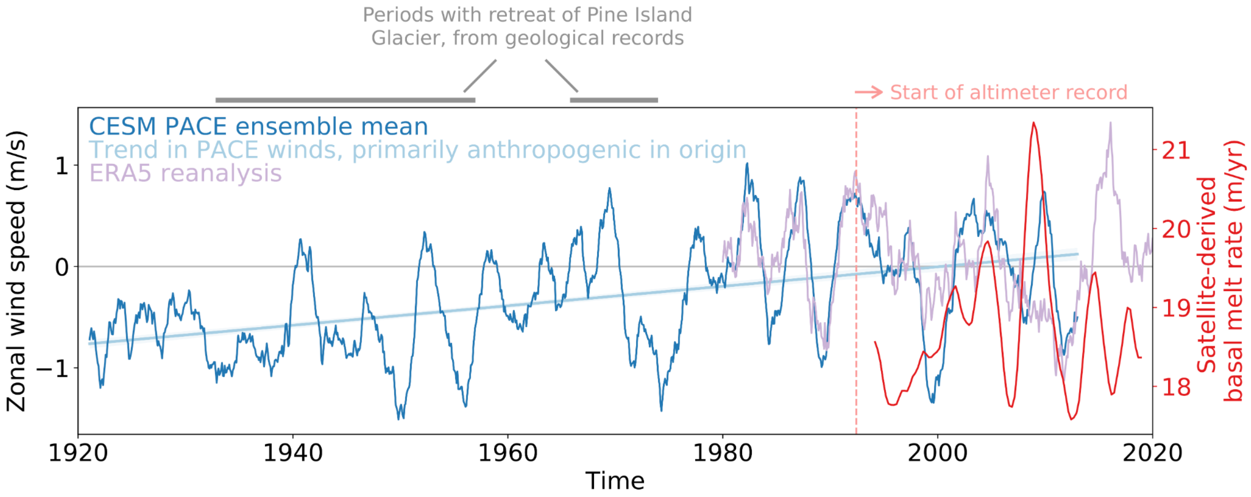

Figure 4: Changes in zonal winds due to natural variability and anthropogenic forcing drive changes over Pine Island Glacier and Thwaites ice shelves (modified from Holland et al., 2019). Changes in zonal winds are shown over Pine Island/Thwaites troughs, using a box whose location is shown in Figure 3. Winds are from: (1) The Community Earth System Model Pacific Pacemaker (CESM PACE) 20 member ensemble for 1920–2013 (Deser et al., 2017) and (2) The ERA5 reanalysis for 1979–2020 (Hersbach et al., 2020). Positive winds represent eastward winds (westerlies), which can drive a higher influx of warm circumpolar deep water (CDW) under the Pine Island and Thwaites ice shelf cavities (e.g., Thoma et al., 2008). The influence of changes in CDW on melt rates can be measured using basal melt rates using satellite altimetry, which are only available from 1994 onward, and therefore capture only a snapshot of the full temporal variability in the system. Geological evidence was used to constrain times prior to the satellite record during which Pine Island Glacier Ice Shelf retreated (Smith et al., 2017).

1.5 References

Barnard, P.L., Erikson, L.H., Foxgrover, A.C., Hart, J.A.F., Limber, P., O'Neill, A.C., van Ormondt, M., Vitousek, S., Wood, N., Hayden, M.K. &Jones, J.M. (2019). Dynamic flood modeling essential to assess the coastal impacts of climate change. *Scientific reports*, *9*(1), pp.1-13.

Bintanja, R., Van Oldenborgh, G. J., Drijfhout, S. S., Wouters, B., & Katsman, C. A. (2013). Important role for ocean warming and increased ice-shelf melt in Antarctic sea-ice expansion. Nature Geoscience, 6(5), 376-379.

Bronselaer, B., Winton, M., Griffies, S.M., Hurlin, W.J., Rodgers, K.B., Sergienko, O.V., Stouffer, R.J. and Russell, J.L. (2018). Change in future climate due to Antarctic meltwater. Nature, 564(7734), pp.53-58.

DeConto, R.M., Pollard, D., Alley, R.B., Velicogna, I., Gasson, E., Gomez, N., Sadai, S., Condron, A., Gilford, D.M., Ashe, E.L. and Kopp, R.E. (2021). The Paris Climate Agreement and future sea-level rise from Antarctica. Nature, 593(7857), pp.83-89.

Deser, C., Guo, R., & Lehner, F. (2017). The relative contributions of tropical Pacific sea surface temperatures and atmospheric internal variability to the recent global warming hiatus. Geophysical Research Letters, 44(15), 7945-7954.

Dutrieux, P., De Rydt, J., Jenkins, A., Holland, P.R., Ha, H.K., Lee, S.H., Steig, E.J., Ding, Q., Abrahamsen, E.P. and Schröder, M. (2014). Strong sensitivity of Pine Island ice-shelf melting to climatic variability. Science, 343(6167), pp.174-178.

Gardner, A. S., Moholdt, G., Scambos, T., Fahnstock, M., Ligtenberg, S., Broeke, M. V. D., & Nilsson, J. (2018). Increased West Antarctic and unchanged East Antarctic ice discharge over the last 7 years. The Cryosphere, 12(2), 521-547.

Gerringa, L.J., Alderkamp, A.C., Laan, P., Thuroczy, C.E., De Baar, H.J., Mills, M.M., van Dijken, G.L., van Haren, H. & Arrigo, K.R. (2012). Iron from melting glaciers fuels the phytoplankton blooms in Amundsen Sea (Southern Ocean): Iron biogeochemistry. Deep Sea Research Part II: Topical Studies in Oceanography, 71, pp.16-31.

Goldberg, D. N. (2016). Ice shelf buttressing. International Encyclopedia of Geography: People, the Earth, Environment and Technology: People, the Earth, Environment and Technology, 1-9.

Golledge, N. R., Keller, E. D., Gomez, N., Naughten, K. A., Bernales, J., Trusel, L. D., & Edwards, T. L. (2019). Global environmental consequences of twenty-first-century ice-sheet melt. Nature, 566(7742), 65-72.

Gudmundsson, G. H., Paolo, F. S., Adusumilli, S., & Fricker, H. A. (2019). Instantaneous Antarctic ice sheet mass loss driven by thinning ice shelves. Geophysical Research Letters, 46(23), 13903-13909.

Hersbach, H., Bell, B., Berrisford, P., Hirahara, S., Horányi, A., Muñoz-Sabater, J., Nicolas, J., Peubey, C., Radu, R., Schepers, D. & Simmons, A. (2020). The ERA5 global reanalysis. Quarterly Journal of the Royal Meteorological Society, 146(730), pp.1999-2049.

Holland, P. R., Bracegirdle, T. J., Dutrieux, P., Jenkins, A., & Steig, E. J. (2019). West Antarctic ice loss influenced by internal climate variability and anthropogenic forcing. Nature Geoscience, 12(9), 718-724.

Joughin, I., Rignot, E., Rosanova, C. E., Lucchitta, B. K., & Bohlander, J. (2003). Timing of recent accelerations of Pine Island glacier, Antarctica. Geophysical Research Letters, 30(13).

Jourdain, N. C., Asay-Davis, X., Hattermann, T., Straneo, F., Seroussi, H., Little, C. M., & Nowicki, S. (2020). A protocol for calculating basal melt rates in the ISMIP6 Antarctic ice sheet projections. The Cryosphere, 14(9), 3111-3134.

Mouginot, J., B. Scheuchl, and E. Rignot. 2017. MEaSUREs Antarctic Boundaries for IPY 2007-2009 from Satellite Radar, Version 2. Boulder, Colorado USA. NASA National Snow and Ice Data Center Distributed Active Archive Center. [Accessed Apr. 25, 2021].

Nakayama, Y., Manucharyan, G., Zhang, H., Dutrieux, P., Torres, H.S., Klein, P., Seroussi, H., Schodlok, M., Rignot, E. and Menemenlis, D. (2019). Pathways of ocean heat towards Pine Island and Thwaites grounding lines. Scientific reports, 9(1), pp.1-9.

Oppenheimer, M., Glavovic, B., Hinkel, J., van de Wal, R., Magnan, A.K., Abd-Elgawad, A., Cai, R., Cifuentes-Jara, M., Deconto, R.M., Ghosh, T. and Hay, J. (2019). Sea level rise and implications for low lying islands, coasts and communities. In: IPCC Special Report on the Ocean and Cryosphere in a Changing Climate.

Paolo, F. S., Fricker, H. A., & Padman, L. (2015). Volume loss from Antarctic ice shelves is accelerating. Science, 348(6232), 327-331.

Paolo, F. S., Padman, L., Fricker, H. A., Adusumilli, S., Howard, S., & Siegfried, M. R. (2018). Response of Pacific-sector Antarctic ice shelves to the El Niño/Southern oscillation. Nature geoscience, 11(2), 121-126.

Pritchard, H., Ligtenberg, S. R., Fricker, H. A., Vaughan, D. G., van den Broeke, M. R., & Padman, L. (2012). Antarctic ice-sheet loss driven by basal melting of ice shelves. Nature, 484(7395), 502-505.

Rignot, E., Mouginot, J., Scheuchl, B., Van Den Broeke, M., Van Wessem, M. J., & Morlighem, M. (2019). Four decades of Antarctic Ice Sheet mass balance from 1979–2017. Proceedings of the National Academy of Sciences, 116(4), 1095-1103.

Robel, A. A., Seroussi, H., & Roe, G. H. (2019). Marine ice sheet instability amplifies and skews uncertainty in projections of future sea-level rise. Proceedings of the National Academy of Sciences, 116(30), 14887-14892.

Rosenzweig, C., & Solecki, W. (2014). Hurricane Sandy and adaptation pathways in New York: Lessons from a first-responder city. Global Environmental Change, 28, 395-408.

Scambos, T., Hulbe, C., & Fahnestock, M. (2003). Climate-induced ice shelf disintegration in the Antarctic Peninsula. Antarctic Peninsula Climate Variability: Historical and Paleoenvironmental Perspectives, Antarct. Res. Ser, 79, 79-92.

Scambos, T. A., Bohlander, J. A., Shuman, C. A., & Skvarca, P. (2004). Glacier acceleration and thinning after ice shelf collapse in the Larsen B embayment, Antarctica. Geophysical Research Letters, 31(18).

Schoof, C. (2007). Ice sheet grounding line dynamics: Steady states, stability, and hysteresis. Journal of Geophysical Research: Earth Surface, 112(F3).

Smith, J.A., Andersen, T.J., Shortt, M., Gaffney, A.M., Truffer, M., Stanton, T.P., Bindschadler, R., Dutrieux, P., Jenkins, A., Hillenbrand, C.D. and Ehrmann, W. (2017). Sub-ice-shelf sediments record history of twentieth-century retreat of Pine Island Glacier. Nature, 541(7635), pp.77-80.

Smith, B., Fricker, H.A., Gardner, A.S., Medley, B., Nilsson, J., Paolo, F.S., Holschuh, N., Adusumilli, S., Brunt, K., Csatho, B. and Harbeck, K. (2020). Pervasive ice sheet mass loss reflects competing ocean and atmosphere processes. Science, 368(6496), pp.1239-1242.

Steig, E. J., Ding, Q., Battisti, D. S., & Jenkins, A. (2012). Tropical forcing of Circumpolar Deep Water inflow and outlet glacier thinning in the Amundsen Sea Embayment, West Antarctica. Annals of Glaciology, 53(60), 19-28.

Tapley, B.D., Watkins, M.M., Flechtner, F., Reigber, C., Bettadpur, S., Rodell, M., Sasgen, I., Famiglietti, J.S., Landerer, F.W., Chambers, D.P. and Reager, J.T. (2019). Contributions of GRACE to understanding climate change. Nature climate change, 9(5), pp.358-369.

The IMBIE team. (2018). Mass balance of the Antarctic Ice Sheet from 1992 to 2017. Nature, 558(7709), 219-222.

The IMBIE team. (2020). Mass balance of the Greenland Ice Sheet from 1992 to 2018. Nature, 579(7798), 233-239.

Thomas, R. H. (1979). Ice shelves: a review. Journal of Glaciology, 24(90), 273-286.

Thoma, M., Jenkins, A., Holland, D., & Jacobs, S. (2008). Modelling circumpolar deep water intrusions on the Amundsen Sea continental shelf, Antarctica. Geophysical Research Letters, 35(18).

Tinto, K. J., Padman, L., Siddoway, C. S., Springer, S. R., Fricker, H. A., Das, I., Tontini, F. C., Porter, D. F., Frearson, N. P., Howard, S. L., Siegfried, M. R., Mosbeux, C., Becker, M. K., Bertinato, C., Boghosian, A., Brady, N., Burton, B. L., Chu, W., Cordero, S. I., Bell, R. E. (2019). Ross Ice Shelf response to climate driven by the tectonic imprint on seafloor bathymetry. Nature Geoscience, 12(6), 441–449.

Velicogna, I., Mohajerani, Y., Landerer, F., Mouginot, J., Noel, B., Rignot, E., Sutterley, T., van den Broeke, M., van Wessem, M. and Wiese, D. (2020). Continuity of ice sheet mass loss in Greenland and Antarctica from the GRACE and GRACE Follow-On missions. Geophysical Research Letters, 47(8).

Zanna, L., Khatiwala, S., Gregory, J. M., Ison, J., & Heimbach, P. (2019). Global reconstruction of historical ocean heat storage and transport. Proceedings of the National Academy of Sciences, 116(4), 1126-1131.

Zemp, M., Huss, M., Thibert, E., Eckert, N., McNabb, R., Huber, J., Barandun, M., Machguth, H., Nussbaumer, S.U., Gärtner-Roer, I. and Thomson, L. (2019). Global glacier mass changes and their contributions to sea-level rise from 1961 to 2016. Nature, 568(7752), pp.382-386.

Chapter 2

Satellite altimetry over the Antarctic Ice Sheet

2.1 Basic principle of satellite altimetry

Satellite altimeters make precise measurements of the travel time for a pulse of electromagnetic radiation generated by the altimeter to reach the Earth's surface and return to the satellite. The altimeters used in this dissertation can be broadly classified into laser and radar altimeters depending on the frequency of radiation used to illuminate the target on the ground. The two-way travel time, combined with the knowledge of the altitude and pointing of the satellite relative to the Earth's surface, can be used to make precise estimates of the height of the reflecting surface in that reference frame after accounting for propagation delays in the atmosphere (for laser and radar altimeters) and the ionosphere (for radar altimeters). In this Chapter, we provide background and context for the instruments and processing techniques to identify the contributors to changes in height over the ice sheet, including the floating ice shelves, derived using radar altimetry in Chapters 3–4 and laser altimetry in Chapter 5.

2.2 Satellite altimeters operating in near-polar orbits

Although there have been several satellite missions with onboard altimeters, the orbits of many satellites do not have the inclination necessary to provide adequate coverage over the Antarctic Ice Sheet. In this dissertation, we focus on satellite altimetry data from five polar-orbiting satellites: ERS-1 (1992–1996), ERS-2 (1995–2003), Envisat (2002–2012), and CryoSat-2 (ongoing, launched 2010), ICESat (2003–2009), and ICESat-2 (ongoing, launched 2018) (Figure 1).

We do not consider data from several altimetry missions that are available over the Antarctic Ice Sheet. The Seasat operated altimeter during 1978 and its southern orbit limit was 72° S, which covered some northern parts of Antarctica (e.g., Fricker and Padman, 2012), but did not overlap in time with other altimetry data. Although it was the precursor to all altimetry over ice, we do not use it here because we focus on estimating a continuous time series of height. We also did not consider more recent altimeters like Sentinel 3A/B (e.g., McMillan et al., 2019) and Altika (e.g., Otosaka et al., 2019) that fully overlap in time with CryoSat-2, because CryoSat-2 allows for increased coverage and more accurate height retrievals over the ice sheet.

2.2.1 ERS-1, ERS-2, and Envisat

The ERS-1, ERS-2, and Envisat satellite missions operated between 1992 and 2012 and included on-board radar altimeters operating at 2.2 cm wavelength (Ku-band). These altimeters functioned by sending a radar pulse, whose duration is determined by the inverse of the bandwidth of the radar "chirp" (e.g., Rapley et al., 1985; Rees, 2013). The altimeter then received and timed the return echo from the Earth's surface. ERS-1/-2 and Envisat are "pulse-limited" altimeters, because the total area on the ground from which the pulse is reflected depends not on the width of the beam, but on the duration of the compressed pulse (Rapley, 1990). The returned power is typically shown in a power-vs-time curve, called a "waveform" (Figure 2). For surfaces covered with water, the shape of the waveform is determined mainly by surface properties and the antenna power pattern (e.g., Brown, 1977); however, for ice sheets, where the radar signal can penetrate through the snowpack, waveform shape is also influenced by sub-surface, (or volume), scattering (e.g., Ridley and Partington, 1998; Partington et al., 1989). The height of the surface is typically estimated by tracking a location on the rising slope (the “leading-edge slope”; Figure 2) of the waveform (e.g., Martin et al., 1983; Davis, 1997); this is called “retracking”. The area under the waveform, also known as the backscatter, is typically used to infer the effects of surface and volume scattering on the waveform (e.g., Wingham et al., 1998).

Longer pulse durations allow for improved retrieval over complex terrains such as ice (e.g., Rapley et al., 1983); however, the retracked height has lower resolution because the waveform is stored within the same number of echo samples, or “range gates" (e.g., Cadzow, 1973). ERS-1/-2 operated in two modes (e.g., Scott et al., 1994) and stored data in 64 range gates, with a resolution of either 3 ns (1.7 km footprint, “ocean mode”) or 12.1 ns (3.4 km footprint, “ice mode”). Envisat operated in three modes and stored data in 128 range gates, with a resolution of either 3.1 ns (“fine mode”, 1.7 km footprint), 12.5 ns (“medium mode”, 3.5 km footprint), or 50 ns (“coarse mode”, 7 km footprint). Unlike for ERS-1 and ERS-2, where mode switches were triggered through ground command, Envisat mode switches were made automatically through onboard processing (e.g., Roca et al., 2009).

The pulse repetition frequency (PRF) of an altimeter represents the number of pulses emitted by the instrument per second, and in part determines the sampling rate of the instrument in the along-track direction. ERS-1 and ERS-2 had a PRF of 1024 Hz, and Envisat had a higher PRF of 1795 Hz. Envisat collected about 75% more data than ERS-1/-2 due to the increased PRF, and sampled heights spaced at intervals of around 400 m on the surface. All three satellites were primarily in orbits with an inclination of around 98.5° (representing coverage up to 81.5°S) with a repeat period of 35 days. Exceptions to that include periods with 3-day repeats for ERS-1 (Dec. 1991 to Mar. 1992 and Dec. 1993 to Apr. 1993), with 168-day repeats for ERS-1 (Geodetic Phase, Apr. 1994 to Mar. 1995), and with an inclination drift for Envisat (after Oct.

2010). In Chapter 3, we use a time series of height changes from ERS-1, ERS-2, and Envisat provided by Paolo et al. (2015, 2016). In Chapter 4, we reprocessed data from these satellite missions to take advantage of improved datasets available through the Reprocessing of Altimeter Products for ERS (REAPER) product (Brokley et al., 2017).

2.2.2 CryoSat-2

CryoSat-2 utilises a similar Ku-band instrument as the previous radar altimeters; however, improvements in engineering and orbit allow for estimates of height changes at better accuracy, resolution, and coverage over ice shelves. The altimeter on CryoSat-2 operates in three measurement modes. Over the ocean and flat portions of the ice sheet, the altimeter operates in Low Resolution Mode (LRM), where the measurement technique is similar to that of previous, "conventional" altimeters, with a 3.1 ns pulse duration, 128 range gates, and a PRF of 1970 Hz (ESRIN/MSSL, 2013). However, in areas with more complex terrain, the altimeter operates in Synthetic Aperture Radar (SAR) mode, where it emits 64 pulses in a burst lasting 3.5 ms, with bursts spaced 11.7 ms apart. The distance between each of the 64 pulses on the ground is around 250 m in the along-track direction, and each location on the ground is measured by more than one burst (Raney, 1998); data from several bursts can be averaged using a technique called "multilooking" to reduce noise (Wingham et al., 2004). This results in a footprint that is around 250 m long in the along-track direction and pulse-limited in the across-track direction. Over even more complex terrain, CryoSat-2 uses SAR Interferometric (SARIn) mode, where return echoes are received by two antennas separated by about 1 m. The differences in the signal phases between the returns from the same 250 m strip can be used to estimate the origin of the echo within the strip, allowing for improved knowledge of the location of the satellite's point of closest approach at which height is retrieved (Galin et al., 2013). The interval between bursts is increased from 11.7 ms in SAR mode to 46.7 ms in SARIn mode, which results in a lower along-track sampling rate.

CryoSat-2 offers a large improvement in coverage over the Antarctic Ice Sheet compared to previous radar altimeters. Its inclination is 92°, allowing for coverage up to 88°S, which includes all ice shelf areas. However, due to data transfer limitations, the satellite only operated in SARIn mode over ice shelves and margins of the grounded ice sheet, but operated in LRM mode over other grounded ice regions. CryoSat-2 also had a long repeat interval (369 days), which led to closer spacing between tracks (Figure 4-S1). In Chapter 3, where we only consider ice shelves, we use SARIn data from CryoSat-2 provided through the “Baseline C” product to extend the time series of height change from ERS-1/-2 and Envisat altimetry provided by Paolo et al., (2015, 2016). In Chapter 4, where we also only consider ice shelves, we took advantage of the improved spatial coverage of CryoSat-2 to estimate height changes at high spatial resolution in a Lagrangian reference frame that advects with ice-shelf flow (e.g., Moholdt et al., 2014). A new CryoSat-2 “Baseline D” data product, which incorporates major changes that improved height retrievals over ice, is now available (Meloni et al., 2020). However, we did not use Baseline D data in this dissertation because they were not available at the time of the analyses.

2.2.3. Ice, Cloud, and land Elevation Satellite

The Ice, Cloud, and land Elevation Satellite (ICESat) operated between 2003 and 2009 and carried a laser altimeter (the Geoscience Laser Altimeter System; GLAS). GLAS used an infrared laser (1064 nm wavelength) to provide precise estimates of surface height (e.g., Zwally et al., 2002). The altimeter transmitted a pulse whose waveform resembled a Gaussian, and returns were measured using a detector and waveform digitizer that recorded the time-varying optical power as waveforms (e.g., Abshire et al., 2005). The return waveform from smooth surfaces also resembled a Gaussian in cases where there was minimal detector saturation. The PRF was 40 Hz, which represents measurements every ~170 m on the ground, and the footprint had a diameter of ~65 m (e.g., Schutz et al., 2005).

ICESat operated in a polar orbit with a 94° inclination, allowing for coverage up to 86°S, which includes all Antarctic ice shelves. One of the three lasers onboard GLAS failed after less than two months from launch, after which the altimeter was operated in “campaign mode” between Oct. 2003 and Oct. 2009 to preserve the life of the remaining two lasers. In this mode, data were acquired for 17 campaigns, with repeats 2 to 3 times per year along the ground tracks of a 33 day subcycle of the 91 day repeat orbit. Because repeats were offset by hundreds of meters in the across-track direction, studies of ice-sheet height change typically used data from several repeat tracks together to account for the impact of surface slope on height change estimates (e.g., Pritchard et al., 2009). We do not process data from ICESat in this dissertation; however, we use results from previous studies to provide context for the radar-derived height changes over ice shelves described in Chapters 3 and 4.

2.2.4. Ice, Cloud, and land Elevation Satellite-2

The Ice, Cloud and land Elevation Satellite-2 (ICESat-2), launched in 2018, carries a photon-counting laser altimeter (the Advanced Topographic Laser Altimeter System; ATLAS). ATLAS was designed to provide estimates of surface height using three pairs of green laser beams at 532 nm wavelength, split from a single laser operating with a tunable pulse energy of 250-1400μJ and a 10 kHz PRF (Sawruk et al., 2013; Martino et al., 2019). The ICESat-2 laser operates at a lower power than the ICESat laser, and is therefore expected to last longer. On the ground, the two beams within a beam pair are separated by ~90 m and each beam pair is separated by ~3.3 km (Figure 3). Each beam has a footprint of ~11 m (Magruder et al., 2020). One beam in a beam pair (the "strong" beam) is transmitted at an energy four times that of the other (the "weak" beam). The returned photons are detected using a photomultiplier tube, in which single photons will trigger a detection (Yang et al., 2019). These photons are then time-tagged and geolocated. The transmitted pulses are spaced on the ground by ~70 cm in the along-track direction; however, most data products use some form of averaging in the along-track direction to improve the signal-to-noise ratio.

ICESat-2's orbit inclination is 92°, allowing for coverage up to at least 88°S. During typical operation over Antarctica, the central beam pair straddles a reference ground track (RGT), and data are collected along the same RGTs every 91 days. Each ICESat-2 cycle constitutes data collection for all of its 1387 RGTs over a 91-day period. The accurate pointing of the altimeter to the same RGTs and the small uncertainty in the location near the ice surface from which the photons are reflected together allow for precise and accurate height change estimates (Smith et al., 2019). The six beam, repeat-track configuration allows us to estimate accurately the contribution of surface slope toward along-track height changes from three beam pairs using a single repeat, which was not possible using previous altimeters. ATLAS started pointing to the RGTs in March 2019, before the acquisition of data over RGT 1 in Cycle 3.

In Chapter 5, we use ice sheet elevations provided through the ATL06 data product (Smith et al., 2020b). ATL06 aggregates data in the along-track direction into segments 40 m long spaced at 20 m intervals (Smith et al., 2019). In regions with low surface slope, ATL06 data have been shown to be accurate to within 3 cm, with a precision less than 9 cm (Brunt et al., 2019).

2.3 Contributors to ice shelf heights and height changes

For floating ice, our goal is to isolate the contribution of ocean-driven basal melting to altimeter-derived height changes. This first requires estimating ice shelf heights relative to the ocean surface. Estimates of ice shelf height from satellite altimetry are typically provided relative to the World Geodetic System 1984 (WGS84) ellipsoid and are corrected for atmospheric delays, earth tides, pole tide, equilibrium tide, and ocean load tide. We can convert heights relative to WGS84 (h_{wgs84}) to heights relative to the ocean surface (h) using:

$$h = h_{wgs84} - h_{geoid} - h_{mdt} - h_{ot} - h_{dac}, \tag{1}$$

where $h_{geoid}$is the height of the geoid above the WGS84 ellipsoid, h_{mdt} the mean dynamic topography (MDT; the height of the time-mean sea surface relative to the geoid), h_{ot} the ocean tide, and h_{dac} the dynamic atmosphere correction (DAC).

In this dissertation, we use the EIGEN-6C4 geoid (Förste et al., 2014) and the DTU13 mean dynamic topography (Andersen et al., 2016). We use heights due to ocean tides (h_{ot}) provided by the CATS2008 circum-Antarctic tidal model (Howard et al., 2019; an update from Padman et al., 2002), which incorporates more observations over ice shelves compared to other models. We use the Mog2D Dynamic Atmosphere Correction (DAC; Carrère et al., 2016) to obtain heights due to atmospheric forcing (h_{dac}). Mog2D includes the influence of changes in atmospheric pressure through the inverse barometer effect (e.g., Padman et al., 2003) and shorter-duration (<20 day) changes due to wind forcing (Carrère and Lyard, 2003). In some data products, heights due to tides and atmospheric forcing are already accounted for in height estimates; in that case, we remove the correction already applied and replace it with the data products described here. There are other contributors to h from ocean variability, such as that from long-term sea level rise near the Antarctic margins (e.g., Rye et al., 2014). We apply a correction for sea level rise, but do not consider other sources of variability because of the lack of observations of water-column thickness changes below ice shelves.

Equation 1 is only valid for ice shelf regions that are in hydrostatic balance. Height changes over ice shelf regions that are not hydrostatically compensated, such as grounding zones (e.g., Fricker and Padman, 2006), requires both reliable models of changes in water-column thickness, and a model of the interaction between the ice shelf and water-column thickness. For grounding zones, we mitigate this challenge by not considering heights retrieved from within a fixed distance from the grounding line (Section 3.6); however, there are models of elastic flexure in the literature that can be used to estimate ice-shelf height changes due to flexure (e.g., Vaughan, 1995) that should be considered in future studies.

2.3.1 Relative magnitudes of contributions to height change and residual uncertainties

The above corrections must be made to convert the altimeter-derived estimate of height above the ellipsoid into an accurate estimate of height above the ocean surface. The relative magnitudes and uncertainties of each of these corrections, and their residual uncertainties are shown in Table 1. Some of these corrections have large magnitudes and are static in time (e.g., MDT, geoid), and can be removed using a model, and so do not contribute to temporal changes in height. Ocean tides also have large magnitude, and represent the largest contribution to height changes over short time periods. However, tide modeling is mature and outputs from tide models have smaller uncertainty compared to other contributions (Padman et al. 2018); these uncertainties can be further reduced by averaging height estimates over long periods (e.g., > 1 yr) of time.

The largest remaining unmodeled contributions to uncertainty in height changes are changes in firn air content (for radar and laser altimetry) and from biases in signal penetration into the snowpack (for radar altimetry). Uncertainties in both contributions have not yet been adequately characterized, but can exceed 1 m and have been shown to be time-dependent. Previous studies, such as Paolo et al. (2016), have shown that the depth of radar signal penetration is 4-5 times lower over ice shelves compared to the rest of the ice sheet due to warmer surface temperatures leading to larger grain sizes and the presence of melt layers. In Chapter 3, we attempt to characterize the influence of variable radar signal penetration by comparing coincident height change estimates from radar and laser altimetry over Antarctic Peninsula ice shelves. In Smith et al. (2020) and Chapter 4, we estimate the uncertainty from changes in firn air content by comparing outputs from two independent firn models, GSFC-FDM and IMAU-FDM.

2.3.2 Estimating changes in ice shelf mass

The primary goal of our ice shelf altimetry studies is to estimate the changes in ice shelf mass by correcting the altimetry-derived height changes for all other contributors. We use the ice-equivalent thickness of an ice shelf (H_i), defined as mass of the ice shelf divided by the typical ice density ρ_i= 917 kg m^{-3}, as a proxy for ice shelf mass:

$$H_i = \frac{1}{\varrho_i} \int_{base}^{surface} \varrho(z)\ dz,$$

where $\varrho(z)$ is the depth-dependent density of the ice shelf. This can be rewritten using the total ice thickness from surface to base (H) and an integral over only the firn layer:

$$H_i = H - \int_{firn} (1 - \frac{\varrho(z)}{\varrho_i})\ dz = H - h_{air},$$

where h_{air} is defined as the firn air content (e.g., Ligtenberg et al., 2011). By assuming hydrostatic equilibrium, we can estimate H_i using the corrected heights h and the firn air content using:

$$H_i = \frac{\varrho_w}{\rho_w - \varrho_i}\ (h - h_{air}),$$

where ϱ_w is the density of the ocean. Assuming that ϱ_w and ϱ_i are constant in time, we can take the derivative on both sides and rearrange to derive an expression for the various contributors of altimeter-derived changes in ice shelf height above the ocean surface in an Eulerian reference frame:

$$\frac{\partial h}{\partial t} = \frac{\partial h_{air}}{\partial t} + (\frac{\rho_w - \rho_i}{\rho_i})\frac{\partial H_i}{\partial t}. \quad (2)$$

2.3.3 Changes in firn air content

Isolating the contribution of ice-equivalent thickness changes $(\partial H_i/\partial t)$ to altimeter-derived height changes $(\partial h/\partial t)$ requires a correction for changes in the air content of the firn column ($\partial h_{air}/\partial t$; Equation 2) due to surface processes such as snowfall, snowmelt, and firn compaction. In Chapter 3, we used $\partial h_{air}/\partial t$ from the Institute for Marine and Atmospheric research Utrecht firn densification model (IMAU-FDM, Ligtenberg et al., 2011). However, outputs from IMAU-FDM were not updated in time for the analyses reported in Chapters 4 and

5. In Chapters 4 and 5, we used the Goddard Space Flight Center firn densification model (GSFC-FDM) to estimate $\partial h_{air}/\partial t$. GSFC-FDM simulates changes in $\partial h_{air}/\partial t$at 5 days temporal sampling using a calibrated Arthern et al. (2010) densification scheme implemented through the Community Firn Model (Stevens et al., 2020). The FDM is forced using precipitation minus evaporation, skin temperature, and meltwater flux from a degree-day model using outputs derived from a combination of the MERRA-2 reanalysis (Gelaro et al., 2017) and an offline 12.5-km resolution MERRA-2 "replay" (Medley et al., 2020).

2.3.4 Contributors to ice-equivalent thickness change

For Chapters 3 and 4, our main goal is to estimate mass change from ocean driven basal melting. To isolate the contribution of ocean-driven basal melting to $\partial H_i/\partial t$, we use mass conservation to decompose it into surface mass balance (m_s), basal melt rate (w_b), and flux divergence of ice-equivalent thickness $\nabla \cdot (\mathbf{v}\boldsymbol{H_i})$ (e.g., Moholdt et al., 2014):

$$\frac{\partial H_i}{\partial t} = m_s - w_b - H_i \nabla \cdot \mathbf{v} - \mathbf{v} \cdot \nabla H_i \tag{3}$$

where **v** are two-dimensional horizontal ice velocities in units of meters per year. The units of m_s and w_b are meters of ice equivalent per year. We estimate m_s using either a reanalysis model such as MERRA-2 (Gelaro et al., 2017), or a regional atmospheric model such as RACMO (van Wessem et al., 2018). Estimates of m_s use a combination of satellite altimetry and a firn model such as GSFC-FDM (Section 3.6). For **v**, we used ice surface velocities derived using a combination of optical and/or radar feature tracking (e.g., Gardner et al., 2015). We do not consider temporal variability in **v**, with the exception of the Amundsen Sea Sector where there have been large changes (e.g., Joughin et al., 2003). However, there is increasing evidence to suggest that changes in $\mathbf{v}$ could be driving changes in ice shelf thickness in other locations as well (e.g., Greene et al., 2017; Klein et al., 2020).

In a Lagrangian reference frame, which tracks an individual parcel of ice, the final term in Equation 3 describing the influence of ice advection vanishes and the material derivative of ice thickness change DH_i/Dt is given by:

$$\frac{DH_i}{Dt} = \frac{\rho_i}{\rho_w - \varrho_i}\left(\frac{Dh}{Dt} - \frac{Dh_{air}}{Dt}\right) = m_s - w_b - H_i \nabla \cdot \mathbf{v}.$$

Ice shelf height changes estimated in a Lagrangian reference frame (Dh/Dt) result in clearer spatial patterns because they account for the advection of surface features (e.g., Moholdt et al., 2014). In Chapter 4, we calculate Dh/Dt using CryoSat-2 altimetry to estimate w_b, but assume that $Dh_{air}/Dt = \partial h_{air}/\partial t$ because of the low spatial resolution of the GSFC-FDM data set compared to the spatial scales over which the material derivative is evaluated. However, interpolating the h_{air}values from the FDM directly to locations where altimeter-derived heights (h) are available (as is done in Chapter 5) can allow for $D(h - h_{air})/Dt$ to be evaluated without the need for this assumption.

2.4 Differences between height change estimates from radar and laser altimetry

Height change estimates derived from radar altimetry can be susceptible to biases from changes in volume scattering (scattering beneath the snow surface). In regions with low surface slope, heights retrieved from Envisat data were typically within 2 m of the snow surface derived from GPS measurements, and heights retrieved from CryoSat-2 SARIn data were typically within 1 m (Schroder et al., 2017). Previous studies have used waveform parameters such as the slope of the leading edge or backscatter as a proxy to determine the contribution of volume scattering (e.g., Arthern et al., 2001). In Chapters 3 and 4, we correct for the effects of volume scattering by assuming that there is a linear relationship between the altimeter-derived heights and backscattered power in dB (Section 3.6), similar to previous studies (e.g., Wingham et al., 1998; Zwally et al., 2005; Paolo et al., 2016). However, recent studies have shown that such an empirical correction can be avoided by selecting a retracker that is less sensitive to volume scattering (e.g., Nilsson et al., 2016).

Height change estimates from laser altimetry represent changes occurring closer to the snow surface. However, there are some differences between heights estimated using green (532 nm wavelength) and infrared (1064 nm wavelength) lasers, with green light scattering from deeper within the snow column compared to infrared light. Modelling studies have suggested differences in the depth of scattering of 10s of cm, but these have not yet been adequately verified by observations (Smith et al., 2018). The amount of scattering is expected to depend on the properties of the snow, with higher scattering in fresh snow compared to aged snow or snow with impurities (Gardner and Sharp, 2010). Some of the biases resulting from these differences are mitigated in the ATL06 data product through the use of a median-based estimate of surface height (Smith et al., 2016).

In this dissertation, we use radar and laser altimetry for different applications. Although we do not directly compare them over the whole ice sheet, we do perform some comparisons over various regions and timescales. In Chapter 3, we compare the radar-derived estimates of height change for Antarctic Peninsula ice shelves with laser-derived height changes from airborne and satellite platforms. We show good agreement between the two estimates for the large southern ice shelves (Figure 3-1), where differences in data sampling are not as important as they are in more northerly regions. Spatial patterns of ice shelf thickness changes derived in

Chapter 4 from radar altimetry show similar patterns to those estimated from ICESat-2 and ICESat laser altimetry (Figure 4). However, differences for height changes derived at shorter period time scales, such as those shown in Chapter 4, could be larger. The simultaneous operation of both ICESat-2 and CryoSat-2, and the new CryoSat-2 orbit designed to increase the volume of near-coincident data collected by the two missions, presents a unique opportunity for future research in reconciling height change estimates from the two independent datasets.

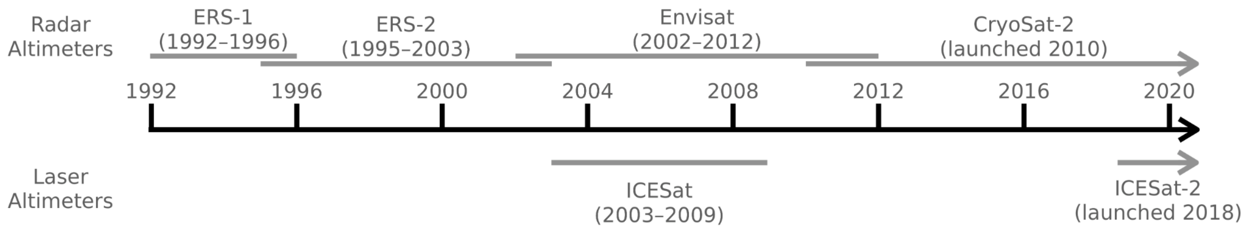

Figure 1: Timeline of the satellite radar and laser altimeters used in this dissertation. The satellite radar altimeters were operated by ESA and the laser altimeters by NASA.

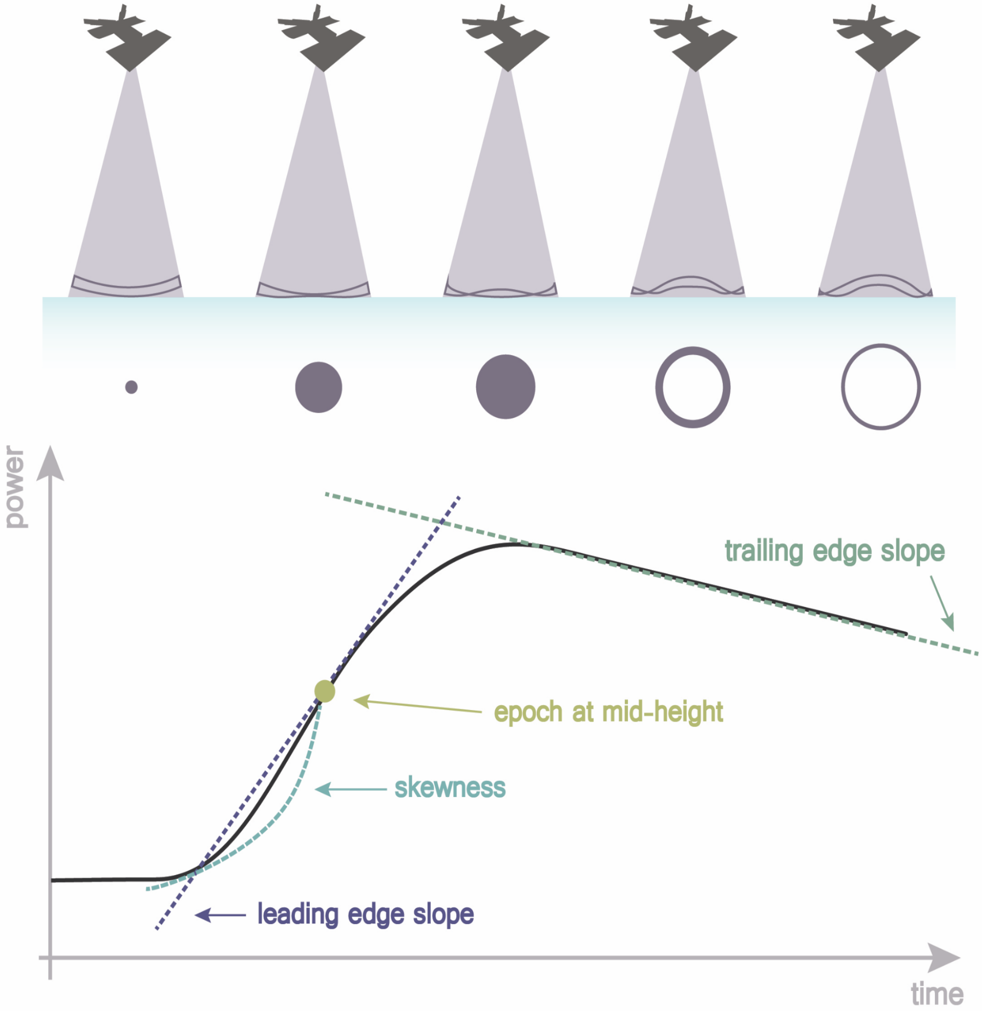

Figure 2: Illustration of a return waveform (power vs. time curve) from a flat surface for a pulse-limited radar altimeter (e.g., ERS-1/-2, Envisat). The antenna on board the altimeter records the return power from the surface as a function of time, shown as a curve called the return "waveform". The shape of the waveform is determined by characteristics of the surface and the altimeter. Modified from ESA's radar altimetry tutorial by Caroline Fleet.

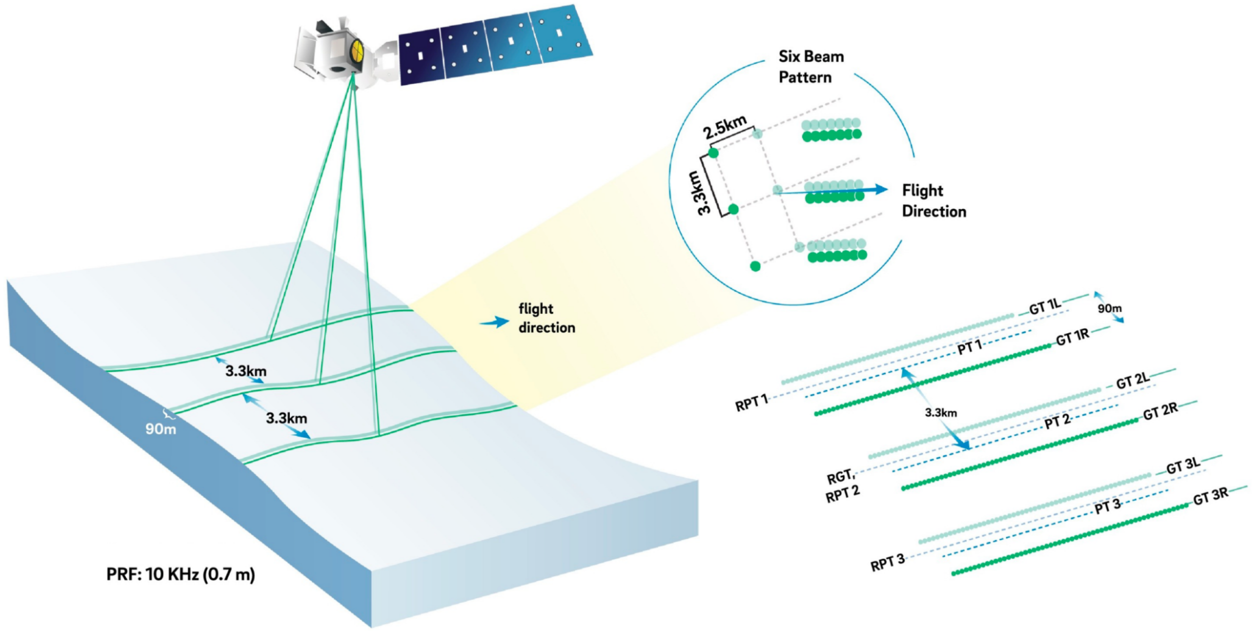

Figure 3: The 6-beam pattern of ICESat-2’s ATLAS instrument. The six beams are organised into 3 pairs. The reference pair tracks (RPTs), representing the ideal center of each beam pair, are separated by about 3.3 km. The central RPT follows the reference ground track (RGT). The measured pair tracks (PTs) observed by the satellite deviate from the RPTs because of inaccuracies in pointing, but typically fall within the two beams of the beam pair. Figure by Jenniffer Matthews, Scripps Institution of Oceanography, and reproduced from Smith et al., (2016).

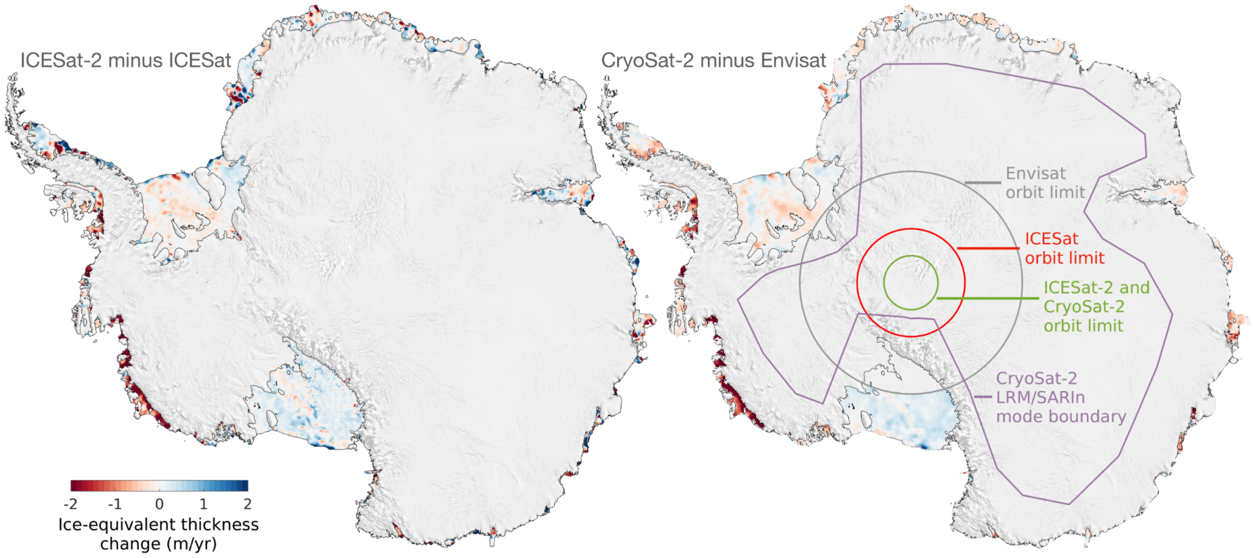

Figure 4: Differences between ice-equivalent thickness changes for Antarctic ice shelves derived using laser altimetry (ICESat-2 and ICESat; Smith et al., 2020) and radar altimetry (CryoSat-2 minus Envisat; Adusumilli et al., 2020, also Chapter 4). The ICESat-2 minus ICESat thickness changes were derived from the first 5 months of ICESat-2 data (October 2018 to February 2019) and ICESat data collected during 2003–2008. The CryoSat-2 minus Envisat thickness changes were derived from CryoSat-2 data collected during October–December 2019 and Envisat data during 2003–2008.

Table 1: Magnitude and uncertainties in contributors to heights and height changes derived using satellite altimetry over ice shelves.

Contributions to heights	Magnitude	Uncertainty	Reference	Notes	Radar	Laser
Geoid	0-70 m	~1-2 m	Förste et al. (2014)	Static in time	x	x
Mean Dynamic Topography	0-2 m	~0-50 cm	Armitage et al. (2018)	Static in time, typically extrapolated into ice shelf cavities	x	x
Instrumental errors, orbit errors, propagation delays	0-5 m	~1-10 cm			x	x
Ocean load tides	0-10 cm	~0.01-0.1 cm	Yi, Minster, and Bentley (2004)		x	x
Dynamic Atmosphere Correction	0-50 cm	~1-10 cm	Carrère and Lyard (2003)	Higher uncertainty in grounding zones	x	x
Ocean tides	0-4 m	~1-10 cm	Padman, Erofeeva, and Fricker (2008)	Higher uncertainty in grounding zones	x	x
Laser-derived height changes corrected for time-dependent contributions	0-2 m	~1-10 cm	Moholdt et al. (2018)	1-year time scale		x
Radar-derived height changes corrected for time-dependent contributions	0-2 m	~1-50 cm	Adusumilli et al. (2018)	1-year time scale	x	
Change in firn air content	0-2 m	~10 cm -1 m	Smith et al. (2020)	1-year time scale	x	x
Radar signal penetration	0-2 m	~0-2 m	Nilsson et al. (2015)	Dependent on surface conditions	x	

References

Abshire, J.B., Sun, X., Riris, H., Sirota, J.M., McGarry, J.F., Palm, S., Yi, D. and Liiva, P., (2005). Geoscience laser altimeter system (GLAS) on the ICESat mission: on-orbit measurement performance. Geophysical research letters, 32(21).

Andersen, O., Knudsen, P., & Stenseng, L. (2016). The DTU13 MSS (Mean Sea Surface) and MDT (Mean Dynamic Topography) from 20 Years of Satellite Altimetry. In S. Jin & R. Barzaghi (Eds.), IGFS 2014 (pp. 111–121). Springer International Publishing.

Arthern, R. J., Wingham, D. J., & Ridout, A. L. (2001). Controls on ERS altimeter measurements over ice sheets: Footprint-scale topography, backscatter fluctuations, and the dependence of microwave penetration depth on satellite orientation. Journal of Geophysical Research: Atmospheres, 106(D24), 33471-33484.

Arthern, R. J., Vaughan, D. G., Rankin, A. M., Mulvaney, R., & Thomas, E. R. (2010). In situ measurements of Antarctic snow compaction compared with predictions of models. Journal of Geophysical Research: Earth Surface, 115(F3).

Brockley, D. J., Baker, S., Féménias, P., Martinez, B., Massmann, F. H., Otten, M., & Visser, P. (2017). REAPER: Reprocessing 12 years of ERS-1 and ERS-2 altimeters and microwave radiometer data. IEEE Transactions on Geoscience and Remote Sensing, 55(10), 5506-5514.

Brunt, K. M., Neumann, T. A., & Smith, B. E. (2019). Assessment of ICESat-2 ice sheet surface heights, based on comparisons over the interior of the Antarctic ice sheet. Geophysical Research Letters, 46(22), 13072-13078.

Brown, G. 9. (1977). The average impulse response of a rough surface and its applications. IEEE transactions on antennas and propagation, 25(1), 67-74.

Cadzow, J.A. (1973). Discrete time systems. Prentice-Hall.

Carrère, L., & Lyard, F. (2003). Modeling the barotropic response of the global ocean to atmospheric wind and pressure forcing-comparisons with observations. Geophysical Research Letters, 30(6).

Carrère, L., Faugère, Y., & Ablain, M. (2016). Major improvement of altimetry sea level estimations using pressure-derived corrections based on ERA-Interim atmospheric reanalysis. Ocean Science, 12(3), 825-842.

Chuter, S. J., & Bamber, J. L. (2015). Antarctic ice shelf thickness from CryoSat-2 radar altimetry. Geophysical Research Letters, 42(24), 10-721.

Davis, C. H. (1997). A robust threshold retracking algorithm for measuring ice-sheet surface elevation change from satellite radar altimeters. IEEE Transactions on Geoscience and Remote Sensing, 35(4), 974-979.

European Space Research Institute (ESRIN) – European Space Agency, and Mullard Space Science Laboratory – University College London. CryoSat Product Handbook. (2013).

Förste, C., Bruinsma, S., Abrikosov, O., Flechtner, F., Marty, J.-C., Lemoine, J.-M., Dahle, C., Neumayer, H., Barthelmes, F., König, R., & others. (2014). EIGEN-6C4-The latest combined global gravity field model including GOCE data up to degree and order 1949 of GFZ Potsdam and GRGS Toulouse. EGU General Assembly Conference Abstracts, 16.

Fricker, H. A., & Padman, L. (2006). Ice shelf grounding zone structure from ICESat laser altimetry. Geophysical Research Letters, 33(15).

Fricker, H. A., & Padman, L. (2012). Thirty years of elevation change on Antarctic Peninsula ice shelves from multimission satellite radar altimetry. Journal of Geophysical Research: Oceans, 117(C2).

Galin, N., Wingham, D. J., Cullen, R., Fornari, M., Smith, W. H., & Abdalla, S. (2012). Calibration of the CryoSat-2 interferometer and measurement of across-track ocean slope. IEEE transactions on geoscience and remote sensing, 51(1), 57-72.

Gardner, A. S., & Sharp, M. J. (2010). A review of snow and ice albedo and the development of a new physically based broadband albedo parameterization. Journal of Geophysical Research: Earth Surface, 115(F1).

Gardner, A. S., Moholdt, G., Scambos, T., Fahnestock, M., Ligtenberg, S., Broeke, M. V. D., & Nilsson, J. (2018). Increased West Antarctic and unchanged East Antarctic ice discharge over the last 7 years. The Cryosphere, 12(2), 521-547.

Gelaro, R., McCarty, W., Suárez, M.J., Todling, R., Molod, A., Takacs, L., Randles, C.A., Darmenov, A., Bosilovich, M.G., Reichle, R. and Wargan, K. (2017). The modern-era retrospective analysis for research and applications, version 2 (MERRA-2). Journal of Climate, 30(14), pp.5419-5454.

Greene, C. A., Blankenship, D. D., Gwyther, D. E., Silvano, A., & van Wijk, E. (2017). Wind causes Totten Ice Shelf melt and acceleration. Science Advances, 3(11), e1701681.

Howard, S. L., Padman, L., & Erofeeva, S. Y. (2019). CATS2008: Circum-Antarctic Tidal Simulation version 2008 [Data set]. U.S. Antarctic Program (USAP) Data Center.

Joughin, I., Rignot, E., Rosanova, C. E., Lucchitta, B. K., & Bohlander, J. (2003). Timing of recent accelerations of Pine Island glacier, Antarctica. Geophysical Research Letters, 30(13).

Klein, E., Mosbeux, C., Bromirski, P. D., Padman, L., Bock, Y., Springer, S. R., & Fricker, H. A. (2020). Annual cycle in flow of Ross Ice Shelf, Antarctica: contribution of variable basal melting. Journal of Glaciology, 66(259), 861-875.

Ligtenberg, S. R. M., Helsen, M. M., & Van den Broeke, M. R. (2011). An improved semi-empirical model for the densification of Antarctic firn. The Cryosphere, 5(4), 809-819.

Magruder, L. A., Brunt, K. M., & Alonzo, M. (2020). Early ICESat-2 on-orbit Geolocation Validation Using Ground-Based Corner Cube Retro-Reflectors. Remote Sensing, 12(21), 3653.

Markus, T., Neumann, T., Martino, A., Abdalati, W., Brunt, K., Csatho, B., Farrell, S., Fricker, H., Gardner, A., Harding, D. and Jasinski, M. (2017). The Ice, Cloud, and land Elevation Satellite-2 (ICESat-2): science requirements, concept, and implementation. Remote sensing of environment, 190, pp.260-273.

Martin, T. V., Zwally, H. J., Brenner, A. C., & Bindschadler, R. A. (1983). Analysis and retracking of continental ice sheet radar altimeter waveforms. Journal of Geophysical Research: Oceans, 88(C3), 1608-1616.

Martino, A. J., Neumann, T. A., Kurtz, N. T., & McLennan, D. (2019). ICESat-2 mission overview and early performance. In Sensors, Systems, and Next-Generation Satellites XXIII (Vol. 11151, p. 111510C). International Society for Optics and Photonics.

McMillan, M., Muir, A., Shepherd, A., Roca, M., Aublanc, J., Thibaut, P., & Benveniste, J. (2019). Sentinel-3 Delay-Doppler altimetry over Antarctica. The Cryosphere, 13(2), 709-722.

Medley, B., Neumann, T. A., Zwally, H. J., & Smith, B. E. (2020). Forty-year Simulations of Firn Processes over the Greenland and Antarctic Ice Sheets. The Cryosphere Discussions, 1-35.

Meloni, M., Bouffard, J., Parrinello, T., Dawson, G., Garnier, F., Helm, V., Di Bella, A., Hendricks, S., Ricker, R., Webb, E. and Wright, B. (2020). CryoSat Ice Baseline-D validation and evolutions. The Cryosphere, 14(6), pp.1889-1907.

Moholdt, G., Padman, L., & Fricker, H. A. (2014). Basal mass budget of Ross and Filchner-Ronne ice shelves, Antarctica, derived from Lagrangian analysis of ICESat altimetry. Journal of Geophysical Research: Earth Surface, 119(11), 2361-2380.

Otosaka, I., Shepherd, A., & McMillan, M. (2019). Ice Sheet Elevation Change in West Antarctica From Ka-Band Satellite Radar Altimetry. Geophysical Research Letters, 46(22), 13135-13143.

Padman, L., Fricker, H. A., Coleman, R., Howard, S., & Erofeeva, L. (2002). A new tide model for the Antarctic ice shelves and seas. Annals of Glaciology, 34, 247-254.

Padman, L., King, M., Goring, D., Corr, H., & Coleman, R. (2003). Ice-shelf elevation changes due to atmospheric pressure variations. Journal of Glaciology, 49(167), 521-526.

Padman, L., Siegfried, M. R., & Fricker, H. A. (2018). Ocean tide influences on the Antarctic and Greenland ice sheets. Reviews of Geophysics, 56(1), 142-184.

Paolo, F. S., Fricker, H. A., & Padman, L. (2015). Volume loss from Antarctic ice shelves is accelerating. Science, 348(6232), 327-331.

Paolo, F. S., Fricker, H. A., & Padman, L. (2016). Constructing improved decadal records of Antarctic ice shelf height change from multiple satellite radar altimeters. Remote sensing of environment, 177, 192-205.

Partington, K. C., Ridley, J. K., Rapley, C. G., & Zwally, H. J. (1989). Observations of the surface properties of the ice sheets by satellite radar altimetry. Journal of Glaciology, 35(120), 267-275.

Pritchard, H. D., Arthern, R. J., Vaughan, D. G., & Edwards, L. A. (2009). Extensive dynamic thinning on the margins of the Greenland and Antarctic ice sheets. Nature, 461(7266), 971-975.

Raney, R. K. (1998). The delay/Doppler radar altimeter. IEEE Transactions on Geoscience and Remote Sensing, 36(5), 1578-1588.

Rapley, C. G., Griffiths, H. D., Squire, V. A., Lefebvre, M., Birks, A. R., Brenner, A. C., & Cowan, A. M. (1983). A study of satellite radar altimeter operation over ice-covered surfaces.

Rapley, C. G., Griffiths, H., Squire, V., Olliver, J., Birks, A., Cooper, A., & Guzkowska, M. (1985). Applications and scientific uses of ERS-1 radar altimeter data (Final Report).

Rapley, C. G. (1990). Satellite Rader Altimeters. In Microwave remote sensing for oceanographic and marine weather-forecast models (pp. 45-63). Springer, Dordrecht.

Rees, W. G. (2013). Physical principles of remote sensing, 3rd ed. Cambridge university press.

Ridley, J. K., & Partington, K. C. (1988). A model of satellite radar altimeter return from ice sheets. Remote Sensing, 9(4), 601-624.

Robin, G. de Q. (1958). Glaciology III, seismic shooting and related investigations, in Norwegian-British-Swedish Antarctic Expedition, 1949-52, Scientific Results, Vol. V, Norsk Polarinstitut, Oslo.

Roca, M., Laxon, S., & Zelli, C. (2009). The EnviSat RA-2 instrument design and tracking performance. IEEE Transactions on Geoscience and Remote Sensing, 47(10), 3489-3506.

Sawruk, N.W., Stephen, M.A., Litvinovitch, S., Edelman, J.E., Albert, M.M., Edwards, R.E., Culpepper, C.F., Rudd, W.J., Fakhoury, E. and Hovis, F.E. (2013). Space qualified laser transmitter for NASA's ICESat-2 mission. In Solid State Lasers XXII: Technology and Devices (Vol. 8599, p. 85990O). International Society for Optics and Photonics.

Schutz, B. E., Zwally, H. J., Shuman, C. A., Hancock, D., & DiMarzio, J. P. (2005). Overview of the ICESat mission. Geophysical Research Letters, 32(21).

Scott, R. F., Baker, S. G., Birkett, C. M., Cudlip, W., Laxon, S. W., Mantripp, D. R., & Wingham, D. J. (1994). A comparison of the performance of the ice and ocean tracking modes of the ERS-1 radar altimeter over non-ocean surfaces. Geophysical Research Letters, 21(7), 553-556.

Smith, B., Fricker, H.A., Holschuh, N., Gardner, A.S., Adusumilli, S., Brunt, K.M., Csatho, B., Harbeck, K., Huth, A., Neumann, T. and Nilsson, J. (2019). Land ice height-retrieval algorithm for NASA's ICESat-2 photon-counting laser altimeter. Remote Sensing of Environment, 233, p.111352.

Smith, B. E., Gardner, A., Schneider, A., & Flanner, M. (2018). Modeling biases in laser-altimetry measurements caused by scattering of green light in snow. Remote sensing of environment, 215, 398-410.

Smith, B., H. A. Fricker, A. Gardner, M. R. Siegfried, S. Adusumilli, B. M. Csathó, N. Holschuh, J. Nilsson, F. S. Paolo, and the ICESat-2 Science Team. 2020. ATLAS/ICESat-2 L3A Land Ice Height, Version 3. Boulder, Colorado USA. NASA National Snow and Ice Data Center Distributed Active Archive Center. [Accessed August 2020].

Smith, B., Fricker, H.A., Gardner, A.S., Medley, B., Nilsson, J., Paolo, F.S., Holschuh, N., Adusumilli, S., Brunt, K., Csatho, B. and Harbeck, K., 2020. Pervasive ice sheet mass loss reflects competing ocean and atmosphere processes. Science, 368(6496), pp.1239-1242.

Stevens, C. M., Verjans, V., Lundin, J., Kahle, E. C., Horlings, A. N., Horlings, B. I., & Waddington, E. D. (2020). The Community Firn Model (CFM) v1. 0. Geoscientific Model Development, 13(9), 4355-4377.

Wessem, J. M. V., Berg, W. J. V. D., Noël, B. P., Meijgaard, E. V., Amory, C., Birnbaum, G., Jakobs, C. L., Krüger, K., Lenaerts, J., Lhermitte, S. and Ligtenberg, S. R. (2018). Modelling the climate and surface mass balance of polar ice sheets using RACMO2–Part 2: Antarctica (1979–2016). The Cryosphere, 12(4), pp.1479-1498.

Vaughan, D. G. (1995). Tidal flexure at ice shelf margins. Journal of Geophysical Research: Solid Earth, 100(B4), 6213-6224.

Wingham, D. J., Phalippou, L., Mavrocordatos, C., & Wallis, D. (2004). The mean echo and echo cross product from a beamforming interferometric altimeter and their application to elevation measurement. IEEE Transactions on Geoscience and Remote Sensing, 42(10), 2305-2323.

Wingham, D. J., Shepherd, A., Muir, A., & Marshall, G. J. (2006). Mass balance of the Antarctic ice sheet. Philosophical Transactions of the Royal Society A: Mathematical, Physical and Engineering Sciences, 364(1844), 1627-1635.

Yang, G., Martino, A. J., Lu, W., Cavanaugh, J., Bock, M., & Krainak, M. A. (2019). IceSat-2 ATLAS photon-counting receiver: initial on-orbit performance. In Advanced Photon Counting Techniques XIII (Vol. 10978, p. 109780B). International Society for Optics and Photonics.

Zwally, H.J., Schutz, B., Abdalati, W., Abshire, J., Bentley, C., Brenner, A., Bufton, J., Dezio, J., Hancock, D., Harding, D. and Herring, T. (2002). ICESat's laser measurements of polar ice, atmosphere, ocean, and land. Journal of Geodynamics, 34(3-4), pp.405-445.

Chapter 3

Variable Basal Melt Rates of Antarctic Peninsula Ice Shelves, 1994–2016

Abstract

We have constructed 23-year (1994–2016) time series of Antarctic Peninsula (AP) ice-shelf height change using data from four satellite radar altimeters (ERS-1, ERS-2, Envisat, and CryoSat-2). Combining these time series with output from atmospheric and firn models, we partitioned the total height-change signal into contributions from varying surface mass balance, firn state, ice dynamics, and basal mass balance. On the Bellingshausen coast of the AP, ice shelves lost 84 ± 34 Gt a^{-1} to basal melting, compared to contributions of 50 ± 7 Gt a^{-1} from surface mass balance and ice dynamics. Net basal melting on the Weddell coast was 51 ± 71 Gt a^{-1}. Recent changes in ice-shelf height include increases over major AP ice shelves driven by changes in firn state. Basal melt rates near Bawden Ice Rise, a major pinning point of Larsen C Ice Shelf, showed large increases, potentially leading to substantial loss of buttressing if sustained.

3.1 Introduction

Ice shelves around the periphery of Antarctica connect the grounded ice sheet to the Southern Ocean and are influenced by changes in the ocean, atmosphere, and ice sheet dynamics. Confined ice shelves exert back-stresses on grounded ice, a process called buttressing (Dupont & Alley, 2005). When buttressing is reduced through ice-shelf collapse, substantial thinning, or mechanical weakening of the shear margins, ice streams and outlet glaciers that flow into it accelerate (e.g., Pritchard et al., 2012; Rignot et al., 2004; Scambos et al., 2004), contributing to sea level rise.

The Antarctic Peninsula (AP; Figure 1), the northernmost region of Antarctica, has experienced dramatic reductions in ice-shelf extent (Cook & Vaughan, 2010) and surface height (Paolo, Fricker, & Padman, 2015) in the last few decades. On the eastern (Weddell Sea) side, the collapses of Prince Gustav and Larsen A ice shelves in 1995 were followed by the rapid collapse of most of Larsen B Ice Shelf (LBIS) in 2002. On the western (Bellingshausen Sea) side, the small Müller, Jones, and Wordie ice shelves have all collapsed or substantially retreated, and Wilkins Ice Shelf (WIS) lost a significant portion of its area during large break-up events in 2008 and 2009 (Cook & Vaughan, 2010). Most remaining AP ice shelves have experienced changes in surface height, as measured by satellite altimeters (Fricker & Padman, 2012; Paolo, Fricker, & Padman, 2015; Pritchard et al., 2012), with an overall surface lowering during the time periods covered by these studies.

Declining extent and height of AP ice shelves have been attributed to a complex set of processes involving the atmosphere, ocean, and sea ice. Morris and Vaughan (2003) noted that the timing and location of major collapse events coincided with the southward migration of the mean-annual −9°C isotherm driven by regional atmospheric warming during the last half of the twentieth century; this isotherm was used as a proxy for summer surface melting that can lead to hydrofracture (Scambos et al., 2000; van den Broeke, 2005). Direct atmospheric controls on ice-shelf height include variability of surface mass balance (SMB) (e.g., Kuipers Munneke et al., 2017), density of near-surface firn (Pritchard et al., 2012), and atmospheric pressure inducing changes in ocean surface height (Padman et al., 2003). Atmospheric changes are a combination of natural variability whose role in Antarctic atmospheric state is still poorly understood (Turner et al., 2016), and anthropogenic effects including increased global greenhouse gas concentrations and changing stratospheric ozone levels (Arblaster & Meehl, 2006; Thompson & Solomon, 2002). Changes in atmospheric conditions, notably wind stress, on a wide range of scales from local to global, also alter circulation of subsurface warm water on continental shelves, which in turn drives variations in ice-shelf basal mass balance (BMB) (e.g., Dutrieux et al., 2014; Holland, Jenkins, & Holland, 2010; Paolo et al., 2018). Wind-driven changes in sea-ice concentration and thickness also alter the effect of wind stress on ocean circulation (Kim et al., 2017), ocean-atmosphere heat exchange and ocean mixing (Dinniman et al., 2012), and the production rate of deep water in coastal polynyas, which can modify ocean heat flux under ice shelves (Khazendar et al., 2013).

3.2 Previous Antarctic Peninsula Satellite Altimeter Studies

Shepherd et al. (2003) reported net surface lowering of Larsen C Ice Shelf (LCIS; see Figure 1 for location) based on satellite radar altimetry (RA) for the period 1992–2001 and attributed this lowering to basal melting in excess of the rate required for steady-state mass balance. Fricker and Padman (2012) used height differences at crossover locations between ground tracks of Seasat RA (July to October 1978) and the beginning of the ERS-1 mission (June to October 1992) to show that this surface lowering started before 1992. Pritchard et al. (2012) showed that patterns and magnitudes of time-averaged LCIS height changes derived from ICESat satellite laser altimetry from 2003 to 2008 were consistent with modeled height change from SMB and firn processes, meaning that the basal melt rate during this period was consistent with the value required for steady-state ice-shelf mass balance.

On the Bellingshausen coast, time series of inferred ice thickness (H) for individual ice shelves show substantial temporal variability in dH/dt (Paolo et al., 2015; see their Figure S1A). In particular, WIS and Stange Ice Shelf (SIS) thinned rapidly from 1994 to 2000, then remained fairly stable until 2012 (the end of the record). George VI Ice Shelf (GVIIS) showed high thinning rates throughout the period 1994–2012.

Padman et al. (2012) reported that dH/dt for WIS switched in the year 2000 from a steady decline to approximately steady state, consistent with a rapid reduction in inferred basal melt rate. They attributed the change in melt rate to retreat of the ice base upward from the thick benthic layer of warm Circumpolar Deep Water (CDW) into the cold, fresh upper layer of Winter Water. Continued melting of GVIIS throughout this period is consistent with its ice draft being much deeper than that of WIS (Figure 2a), so that its base remained in the warmer CDW layer.

3.3 Deriving Height Changes and Basal Melt Rates

We used RA data from the CryoSat-2 mission (Wingham et al., 2006) to extend the existing 18-year (1994–2012) ice-shelf height-change records developed by Paolo et al. (2015, 2016) to mid-2017, resulting in a continuous 23-year record of the changes in surface height, $h(t)$, sampled every three months. For consistency with Paolo et al. (2015, 2016), we averaged CryoSat-2 values of $h(t)$ in grid cells of 0.25° in latitude and 0.75° in longitude (~30 × 30 km) and three-month time steps (see the supporting information). We excluded all RA data less than 3 km from the grounding line; this minimized contamination from the flexural boundary layer near the grounding zone where the ice is not fully hydrostatic and tide-model corrections are not valid.

The rate of change of $h(t)$ is a combination of several processes represented by

$$\frac{dh}{dt} = \frac{(\rho_w - \rho_i)}{\rho_w}\left(\frac{M_s}{\rho_i} - \nabla \cdot (\bar{v}H) - w_b\right) + \frac{dh_s}{dt}, \tag{1}$$

where: ρ_w and ρ_i are the densities of seawater (1028±1 kg m^{-3}) and ice (917±5 kg m^{-3}); $\nabla \cdot (\bar{v}H)$ (m a^{-1}) is the sum of ice advection $(\bar{v} \cdot \nabla H)$ and divergence $(H\nabla \cdot \bar{v})$, with $\bar{v}$ being ice velocity and *H* ice-shelf thickness in meters of solid-ice equivalent; M_s (kg m^{-2} a^{-1}) is the SMB; w_b (m a^{-1}) is the basal melt rate in meters of solid-ice equivalent per year (negative for marine-ice growth); and h_s (m) is the contribution to buoyancy-corrected height from changes in density in the firn column. We obtained maps of $\bar{v}$ from Mouginot et al. (2017) and *H* from ice thicknesses derived from CryoSat-2 referenced to velocity acquisition times (see SI). We obtained M_s from the regional atmospheric model RACMO2, version 2.3p2 (Van Wessem et al, 2017), and estimated dh_s/dt from a firn densification model (IMAU-FDM; Ligtenberg et al. 2011) driven by RACMO2.3p2 output, both at 5.5 km horizontal spacing (Van Wessem et al., 2016). Using Equation 1, we then derived w_b as the residual of all other terms. At the time of writing, the IMAU-FDM simulation extends only to the end of 2016; therefore, all quantities that depend on this model are for the period 1994-2016 inclusive (i.e., 23 years). All uncertainties presented in this paper are 95% confidence intervals (unless stated otherwise). We assume that the SMB and firn model outputs have correlated errors within individual ice shelves, resulting in conservative error estimates on the ice-shelf averaged values.

3.4 Results and Discussion

3.4.1 Surface Height Time Series, Trends, and Basal Melt Rates

Most regions of AP ice shelves experienced overall surface lowering between 1994 and 2016 (Figures 1 and 2b), with rates exceeding −0.3 m a^{-1} on portions of northern LCIS, southern GVIIS, and SIS. Surface height for the northern portion of Larsen D Ice Shelf (LDIS) increased over the 23-year period (Figure 2b).

The map of the 23-year averaged basal melt rate w_b (Figure 2c), derived from equation 1, shows that the highest melt rates occur under the southern GVIIS and portions of SIS and LDIS. The ice-shelf averaged estimates of w_b likely underestimate the true values because of our exclusion of all RA data less than 3 km from the grounding line; these data are from regions of thick ice in the grounding zone, where melt rates are expected to be relatively high (Jenkins, 2011). Another potential bias is inherent to the IMAU-FDM, which requires that the net firn-height change from the beginning (1979) to the end (2016) of the simulation be zero due to the steady-state assumption made to obtain a realistic initial firn column (Ligtenberg et al., 2011). This constraint implies a zero-mean value of dh_s/dt between 1979 and 2016 (Figure S1). Over the AP ice shelves, this assumption can contribute uncertainties from ±0.8 to ±2.4 m a^{-1} in the steady state w_b estimates in individual grid cells, as derived using sensitivity tests described by Pritchard et al. (2012). The magnitude of this error over any individual grid cell primarily depends on the uncertainty in the height change due to surface melting. In the following two sections, we summarize the observed temporal variability for the major AP ice shelves and discuss relationships between this variability and forcing by the atmosphere and ocean.

3.4.2 Weddell Coast Ice Shelves

The Weddell coast of the AP is currently occupied by three ice shelves: the remnant portion of LBIS, the large LCIS, and the generally narrow LDIS. The remnant LBIS was sampled by only two ground-track crossover locations of the ERS and Envisat orbits on the freely floating ice shelf (Figure 1). There was a decrease in height at these crossover locations prior to the 2002 collapse of LBIS, followed by a short period of height increase from 2002 to 2005, and then a return to surface lowering (Figure 1). However, because of the poor sampling, we limit discussion of remnant LBIS mass balance. The broad region of northern LDIS, south of Gipps Ice Rise but north of Hearst Island, is reasonably well sampled (Figure 1), but the southern portion consists of a series of narrow, floating ice tongues with high topographic gradients, which results in a lower signal-to-noise ratio in the RA data.

The 23-year net mass balance for LCIS shows mass loss in key regions such as near Bawden Ice Rise (BIR) and the southern grounding line (Figure 2d). The ice-shelf averaged mean w_b is 0.5 ± 1.4 m a^{-1} (Table 1). This low value of w_b is consistent with ocean measurements obtained in February 2002 offshore of the northern LCIS ice front (Nicholls et al., 2004). This study showed that the subsurface layer of Ice Shelf Water flowing out of the ocean cavity beneath LCIS was sourced from cold, saline, Modified Weddell Deep Water (mWDW, with temperature $T_{ocean} < -1.5°C$) that must have been cooled to near the surface freezing point ($T_{ocean} \approx -1.9°C$) before coming into contact with the LCIS base. This cold water would not contain sufficient heat to cause substantial basal melting beyond the point of initial contact with thick ice at the grounding line (Jenkins, 2011).

The LCIS height record for 1994–2017 (Figure 1) shows substantial multiannual variability, with a cumulative surface lowering of 1.0 ± 0.3 m from 1994 to 2009 followed by a surface rising of 0.5 ± 0.3 m from 2009 to 2017. This recent surface rising of LCIS, largely occurring on the northern portion of the ice shelf (Figures 3d and 3e), is a previously undocumented change in the long-term behavior of LCIS. We considered the possibility that the height increase detected by RA may have been related to an upward migration of the radar-reflection horizon within the snowpack, as observed in Greenland (e.g., Nilsson et al., 2015; Thomas et al., 2008). To test this hypothesis, we derived an independent time series of height change on LCIS from Operation IceBridge (OIB) laser altimetry data acquired during the austral summers of 2009, 2010, 2015, and 2016. Unlike microwave-band radar, OIB's visible-band laser reflects from the top surface of the snow or firn and thus can be used to distinguish between a vertically moving internal reflector and true surface-height changes. The OIB-derived height changes were consistent, within measurement uncertainty, with the RA-derived height changes (Figure 1), and so we conclude that a rising internal radar-reflection horizon is unlikely to be the cause of the RA-derived height change in this case. Recent (2011 to 2016) RA-derived changes approximately correspond with variability in the IMAU-FDM simulated time series of hs (Figures 3f–3j and S2), suggesting that increasing firn-air content is the primary contributor to LCIS height increase in this period.

Changes in h_s over LCIS are significantly influenced by surface melting (Pritchard et al., 2012), which occurs primarily during austral summers (December to February; see Figure S1). During summers with anomalously low temperatures, surface melting is reduced, causing a smaller decrease in firn-air content through time than in an average summer; this would lead to a relative increase in h_s. The six-year averaged summer temperature anomalies (relative to the 1979–2016 mean) over LCIS were lower for the 2011–2016 epoch than for any other six-year epoch since 1995 (Figures 3k–3o), as were surface melt anomalies (Figures S2a–S2e). Similar decadal behavior is not apparent in snowfall (Figures S2f–S2j). An increase in air content, as observed over LCIS between 2011 and 2015, could allow more meltwater storage in existing pore space, reducing susceptibility to hydrofracture that can occur when melt ponds form on the surface in summer (Scambos et al., 2013).

On multiannual time scales, the largest height-change rate observed on LCIS was in the north during 1999–2008 (Figures 3b and 3c), corresponding to high w_b anomalies (Figure 4a). Near BIR, height decreased at a rate of -0.27 ± 0.08 m a^{-1} during this period (Figure 4b), averaged over the ~512 km^2 of ice shelf within the grid cell containing BIR. We estimated the time series of various components of mass balance in this region (Figure S3). Time series of w_b was temporally variable, with a maximum of 5 ± 2 m a^{-1} in 2002 (Figure 4c). Since BIR is a significant pinning point for LCIS, basal melting at this rapid rate, if sustained, would lead to reduced contact of the ice shelf with the bed and decrease the stability of LCIS (Borstad et al., 2013, 2017; Holland et al., 2015).

The spatial pattern of the melt rate anomaly for the period 1999–2008 for LCIS and northern LDIS (Figure 4a) is qualitatively similar to the map of modeled w_b reported by Mueller et al. (2012) for a tide-forced simulation with cold water (T_{ocean} of -1.9 to -1.7°C) entering the sub–ice-shelf cavity (their Figure 8). The higher melt rates around BIR during an approximately four-year period centered on 2002 (Figure 4c) are consistent with an increase in ocean temperature around BIR during this period; the model by Mueller et al. (2012) suggests that an increase in T_{ocean} of ~0.2°C would explain the increase in w_b in this region where mixing is dominated by tidal currents. This warmer water (mWDW), with $T_{ocean} \sim -1.7$°C, has been observed just offshore of the LCIS ice front (Nicholls et al., 2004). Our observations, combined with the Mueller et al. (2012) model, suggest that the period of increased w_b may be caused by local inflow of mWDW across the northern LCIS ice front. In this scenario, the subsurface layer of Ice Shelf Water observed by Nicholls et al. (2004) in February 2002 (near the time of maximum w_b around BIR) would represent a meltwater plume from deeper under LCIS where the initial source of heat to the ice is High Salinity Shelf Water ($T_{ocean} \sim -1.9$°C), while the region around BIR melted rapidly as the tidal currents mixed relatively warm mWDW ($T_{ocean} \sim -1.7$°C) to the ice base.

The 1999–2008 basal melt rate anomaly around BIR was of opposite sign to the anomalies near the deep grounding lines of the southern part of LCIS and northern LDIS (Figures 4a and 4c). We hypothesize that the approximately four-year period with high w_b around BIR corresponds to a time when relatively warm water from outside the cavity could reach the ice base around BIR because of a reduction in the flux of cold meltwater from southern LCIS and northern LDIS; see a related study of Filchner-Ronne Ice Shelf by Mueller et al. (2018).

3.4.3 Bellingshausen Coast Ice Shelves

Most large ice shelves along the Bellingshausen coast showed net surface lowering from 1994 to 2017 (Figure 2b). In general, the lowest heights were recorded near 2013, after which heights increased until 2016 (Figure 1). The average net mass balance was -1.2 ± 1.8 m a^{-1}, arising from a basal melt rate of 3.2 ± 1.9 m a^{-1}, compared with the value of 2.0 ± 0.4 m a^{-1} required to balance the sum of SMB and $\nabla \cdot (\bar{v}H)$ (Table 1). These basal melt rates, which are large relative to those for LCIS, are consistent with ocean observations showing the presence of warm CDW, with temperature above 0°C, near the two ice fronts of GVIIS (Jenkins & Jacobs, 2008) and beneath GVIIS (Potter & Paren, 1985). Basal melt rates were highest, up to 7 ± 2 m a^{-1} in the southern portion of GVIIS (Figure 2c) where the ice draft is deeper (Figure 2a). A measured increase in outlet-glacier velocities from 1992 to 2015 in this region (Hogg et al.,

2017) is consistent with sustained ice-shelf mass loss (Figure 2d) reducing buttressing of the adjacent grounded ice.

The remnant portion of WIS has experienced height changes on multiannual timescales (Figure 1), with a surface lowering of 1.1 ± 0.1 m from 1994 to 1998 followed by a period of reduced net lowering of 0.4 ± 0.1 m between 1998 and 2013, and then a more recent height increase of 1.2 ± 0.1 m. The rapid increase in surface height since 2013 recovered most of the height that was lost prior to 2013. Differences between trends in height (Figure 2b) and mass (Figure 2d) can be attributed to the contribution to height change from changes in the firn column (Figure S1).

The recent increases in surface heights of SIS, Bach Ice Shelf, and WIS appear to be mainly related to surface accumulation changes and firn variability (Figure S1). Spatial variability in basal melt rates between the Bellingshausen coast ice shelves is likely related to differences in ocean circulation. The relatively shallow ice drafts of SIS, Bach Ice Shelf, and WIS ice shelves (Figure 2a), compared with that of GVIIS, make them more susceptible to upper-ocean processes that can change on seasonal scales, with a potentially strong dependence on coastal atmospheric conditions (Padman et al., 2012).

3.5 Conclusions

We have used multi-mission satellite RA to construct time series of ice-shelf surface height change h(t) across the AP. We used h(t) records, ice velocity data, and regional atmospheric and firn modeling to estimate the various components of ice shelf mass balance between 1994 and 2016. Overall, the 23-year mean basal melt rates across the AP exceeded those required to balance mean SMB, ice advection, and ice divergence, leading to net ice mass loss. The highest excess melt rates (~1 m a^{-1} ice equivalent) occurred on the Bellingshausen coast, which we attribute to enhanced inflow of warm CDW ($T_{ocean} > 0°C$) under the ice shelves. In the Weddell Sea, where water temperatures on the continental shelf are cold, and constrained to a narrow range (about −1.9 to −1.7°C) (e.g., Pritchard et al., 2012; Schmidtko et al., 2014), the time-averaged excess basal melt rate under LCIS was ~0.4 m a^{-1}.

On shorter time scales, however, most variability in height change was driven by changes in firn height (Figure S2). The largest contribution to height change from modeled firn variability occurred on the Bellingshausen coast ice shelves, with firn height changing up to 2.5 m during the period 1994–2016. On LCIS, firn height changed up to ~1.3 m within the same period, which caused significant variations in measured h including a previously undocumented sustained increase in ice-shelf surface height after 2009. This latter period coincided with cooler summer air temperatures, which we expect would reduce the magnitude of annual firn densification due to surface melting.

Changes in height and mass of AP ice shelves have implications both for their stability and for the adjacent grounded ice. On the Bellingshausen side of the AP, mass loss from GVIIS, especially in its southern portion, appears to have produced a dynamic grounded-ice response: glaciers feeding this ice shelf have accelerated (Hogg et al., 2017; Minchew et al., 2018). On the eastern side, the basal melt rate on LCIS near BIR, an important pinning point for LCIS, can vary from negligible to 5 ± 2 m a^{-1}. If enhanced melt rates were sustained for several years, buttressing of LCIS by BIR could be substantially reduced. Given that melt rates around BIR are expected to depend primarily on ocean temperature (Mueller et al., 2012), future changes in buttressing of LCIS by BIR will depend on the changing contributions of ocean heat supply from mWDW and High Salinity Shelf Water flowing under the northern ice front, as well as cold meltwater plumes flowing from deeper under LCIS.

Previous satellite radar altimeter studies have generally only reported straight-line trends over short, single-mission observation periods. Our record, however, is sufficiently long to link ice-shelf variability to atmospheric and oceanic processes. While we have speculated on the contributions of such processes toward the variability in our derived time series, there are insufficient ocean data from near any of the major AP ice shelves to confirm the inferred relationships between ocean state and ice-shelf response. However, we expect that our new data set for basal mass balance terms will be valuable for testing current and future numerical models of ice-shelf response to climate variability in this region. Our study demonstrates the need for ongoing continuous monitoring of Antarctic ice shelves by satellite altimetry, and the importance of generating long, accurate time series so that we can fully understand the mechanisms involved in ice-shelf-ocean interaction, which will eventually enable us to confidently include this behavior in ice sheet models.

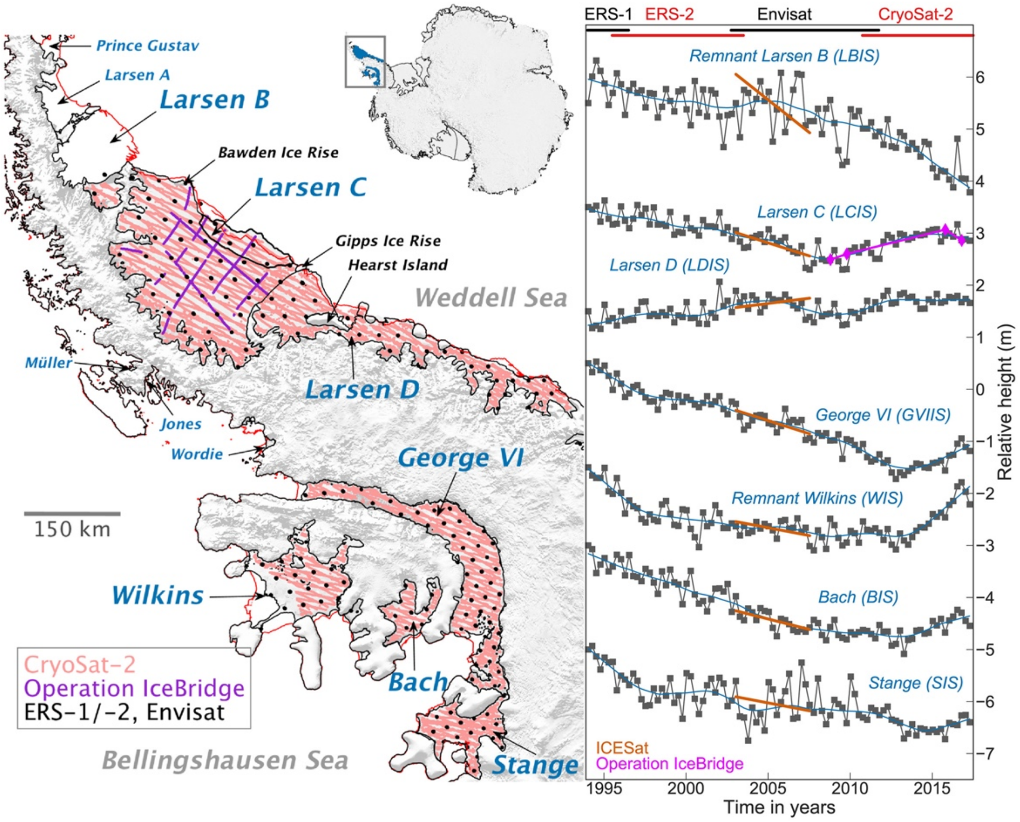

Figure 1. (left) Map of Antarctic Peninsula showing locations of radar and laser altimeter data used in this study: ground tracks for three months of CryoSat-2 (red lines), crossovers for three months of the 35-day repeat orbit of ERS-1 (Phases C and G), ERS-2, and Envisat (black dots), and NASA's Operation IceBridge flights flown in 2008, 2009, 2015, and 2016 (purple lines). Black line on Larsen C Ice Shelf shows outline of iceberg A-68 (A. Luckman, personal communication, 2017), which calved in July 2017. Red outlines show ice-shelf extent in the late 1980s (Cook & Vaughan, 2010). Background image is from the MODIS Mosaic of Antarctica (Scambos et al., 2007). (right) Ice-shelf averaged height changes over Antarctic Peninsula ice shelves, 1994–2017. Black squares show three-month averages; blue lines are three-year filtered heights; red lines are 2003–2008 height-change estimates from ICESat laser altimetry (Pritchard et al., 2012); purple lines on the Larsen C Ice Shelf time series are height-change time series from IceBridge airborne laser altimetry.

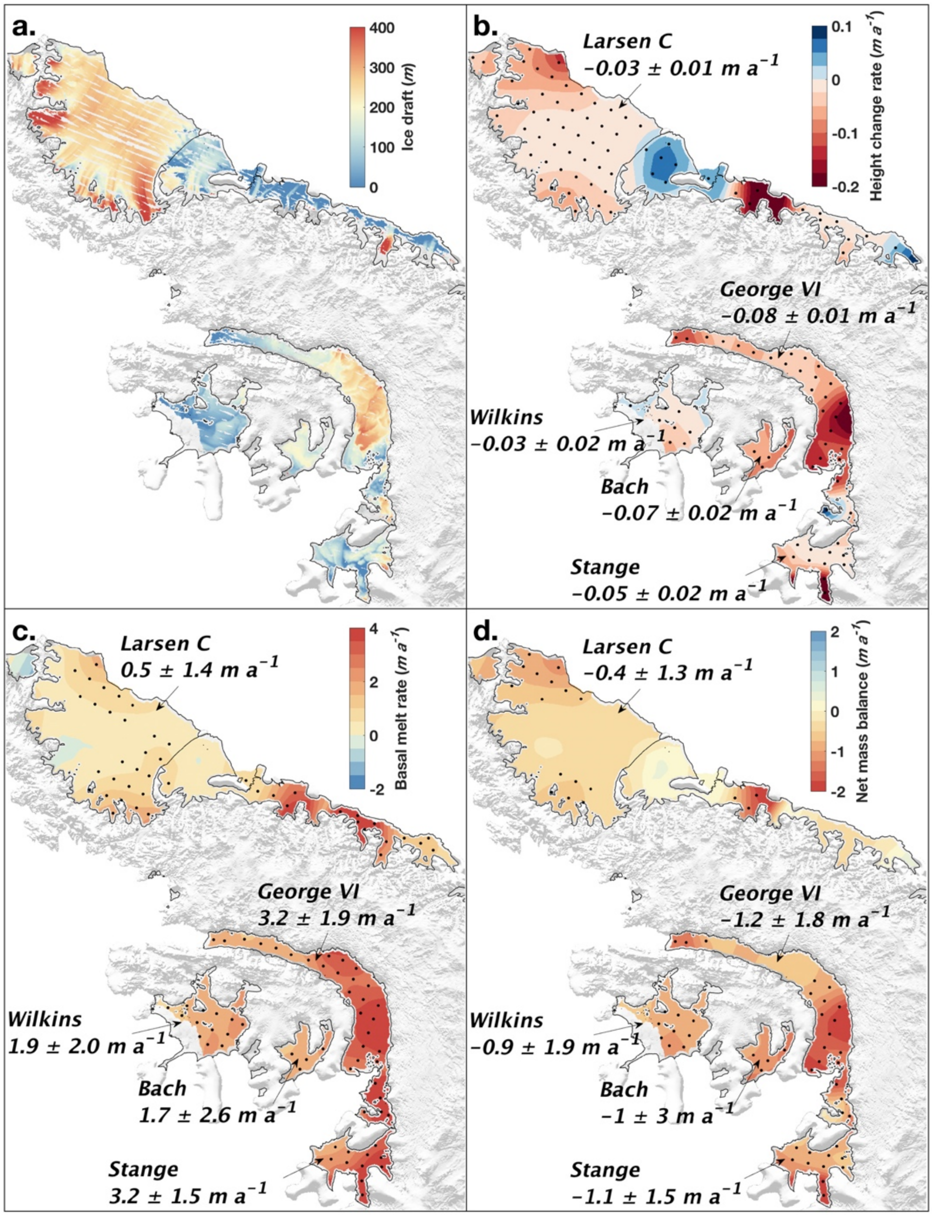

Figure 2. (a) Ice draft from CryoSat-2 at 2 km resolution. Mean values of (b) Height-change rates (*dh/dt*), (c) basal melt rates (w_b), and (d) net mass balance for the period 1994–2016 over Antarctic Peninsula ice shelves. Stippling indicates locations of grid cells with rates above the 67% confidence interval.

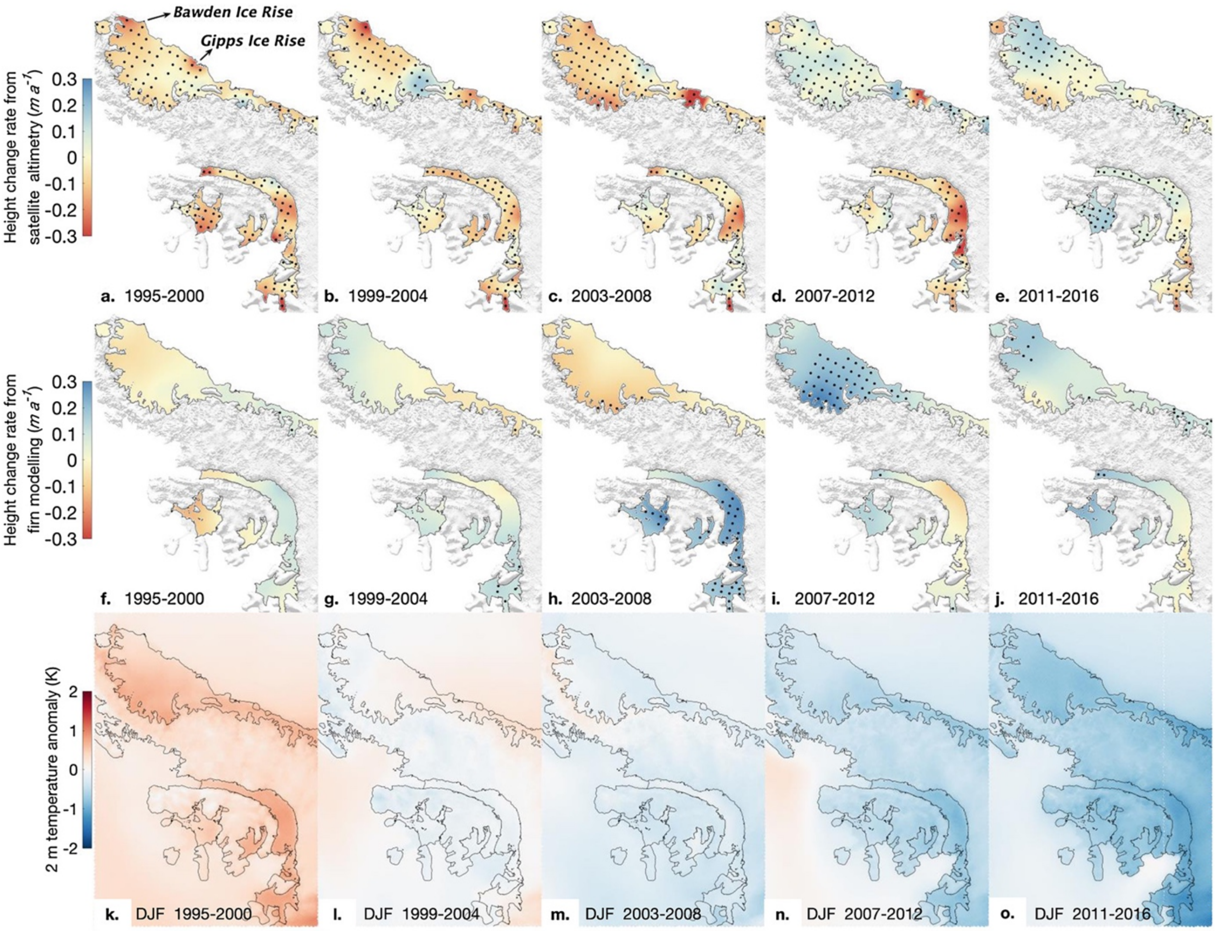

Figure 3. Spatial patterns of ice-shelf height changes for five six-year epochs between 1995 and 2016, from (a-e) satellite radar altimetry and (f-j) the IMAU-FDM firn model. Stippling indicates locations of grid cells with height change rates above their 67% confidence interval. Panels (k-o) show austral summer (December-January-February; DJF) temperature anomalies at 2 m height, relative to the 1979-2016 mean values from the regional atmospheric model RACMO2.3p2.

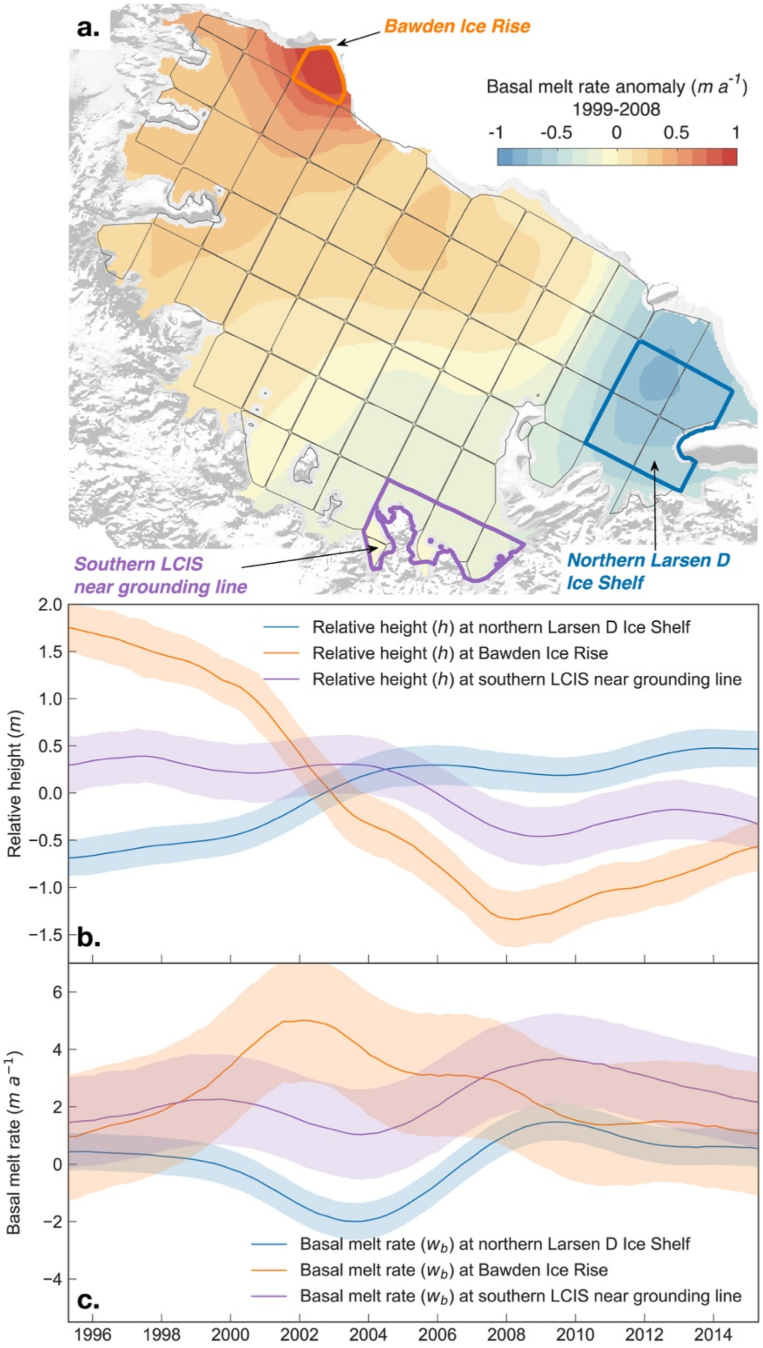

Figure 4. Spatial and temporal variability of basal melt rates for Larsen C and northern Larsen D ice shelves. (a) Average basal melt rate (m a^{-1}) for the period 1999-2008, relative to the average for 1994-2016. Time series of spatially averaged (b) heights and (c) basal melt rates for regions identified on the map by colored outlines: Bawden Ice Rise (orange), northern Larsen D Ice Shelf (blue), and near the southern Larsen C Ice Shelf grounding line (purple).

3.6 Supporting Information

Derivation of 23-year time series of height from satellite radar altimetry

We merged data from four satellite radar altimetry (RA) missions (ERS-1, ERS-2, Envisat, and CryoSat-2) to produce a continuous 23-year record of ice-shelf height in grid cells 0.25° in latitude and 0.75° in longitude at three-month temporal sampling. The procedures for processing the ERS-1, ERS-2, and Envisat RA data to produce an 18-year height record from 1994 to 2012 are described by Paolo et al. (2015, 2016). While those three satellites operated in the same 35-day-repeat orbit for most of their missions and used similar altimeter hardware, the CryoSat-2 radar altimeter (2010-present) is in a drifting orbit and uses more advanced hardware that allows for delay/Doppler processing (Raney, 1998), providing higher accuracy and precision in the derived heights and height changes of ice shelves. Over Antarctic ice shelves, CryoSat-2 operates in synthetic aperture radar-interferometric (SARIn) mode (Wingham et al., 2006), which retrieves heights at the point of closest approach (POCA) within the altimeter footprint of about 0.5 sq.km.

We processed heights from the Level-2 Baseline C CryoSat-2 data product between July 2010 and June 2017 using the following steps.

1. We subsetted data over the ice shelves, using a combination of ice-shelf boundary polygons (Depoorter et al., 2013; Mouginot et al., 2017a; SCAR Antarctic Digital Database) and removed all echoes within 3 km of each ice-shelf boundary to avoid changes related to ice-shelf flexure at the grounding line and calving front mask imperfections.

2. We corrected the heights for ocean tides using the CATS2008 circum-Antarctic tidal model (an update from Padman et al., 2002), ocean load tides using the TPXO7.2 tidal model (Egbert et

al., 1994; Egbert and Erofeeva, 2002), and height changes from atmospheric pressure variations using the Mog2D dynamic atmosphere correction (DAC).

3. We removed heights with a backscatter higher than 30dB (Siegfried et al., 2014) and corrected for a 60 m height bias in the data product in the fields flagged as 'land' or 'closed sea'.

4. We constructed height changes over 2 km grid cells at a 1 km spacing using a modified 'plane fit' model following McMillan et al. (2014). In grid cells with more than six echoes, we modeled the CryoSat-2 heights h_{cs2} as a quadratic function of surface topography (x,y), time t, backscatter g, and a satellite ascending/descending orbit term s using

$$h_{cs2} = h_0 + m_1 x + m_2 y + m_3 x^2 + m_4 y^2 + m_5 xy + m_6 t + m_7 s + m_8 g + h_r, \tag{S1}$$

where h_0 and $\{m_i$: i=1,2,…,8$\}$ are parameters derived from robust linear regression with residuals more than 15 m, or outside 3σ error bounds, removed, and h_r are the residual heights. We then constructed time series of height changes by binning $h = h_r + m_6 t$ in 3-month intervals to match the sampling times of Paolo et al. (2015, 2016).

5. We averaged the height changes in space over the 0.25° x 0.75° grid cells used by Paolo et al. (2015, 2016); there are 130 grid cells over the AP ice shelves.

6. We then combined data from the 18-year height-change record with the 7-year time series of CryoSat-2 data using a zero-median condition for the Envisat/CryoSat-2 overlapping period (2010-2011).

Height time series from Operation IceBridge airborne laser altimetry

NASA's Operation IceBridge (OIB) airborne mission flew a set of repeating swath laser altimetry surveys over LCIS during the austral summers of 2008, 2009, 2015, and 2016 (Figure 1), which provided an opportunity to validate our RA-derived time series. OIB surveyed LCIS with the Airborne Topographic Mapper (ATM; Krabill et al., 2002) in 2008, 2009, and 2016 and the Land Vegetation and Ice Sensor (LVIS; Blair et al., 1999) in 2015. We subsetted the data (Blair and Hofton, 2010; Studinger, 2017) to a region defined as the intersection of the four ATM and LVIS swaths and corrected for ocean tides using CATS2008 (an update from Padman et al., 2002). We then divided this region in 100 m along-track segments centered every 50 m along the ad hoc centerline and used a plane-fitting technique to solve for the height for each survey (h_{2008}, h_{2009}, h_{2015}, and h_{2016}) at the center of each segment. This leverages the entire swath for the resulting height estimate and provides a robust uncertainty estimate. For each segment, we then derived a height change time series $h(t)$ for the four years using

$$\begin{bmatrix} 1 & 0 & 0 & 0 \\ -1 & 1 & 0 & 0 \\ -1 & 0 & 1 & 0 \\ -1 & 0 & 0 & 1 \\ 0 & -1 & 1 & 0 \\ 0 & -1 & 0 & 1 \\ 0 & 0 & -1 & 1 \end{bmatrix} \begin{bmatrix} h(1) \\ h(2) \\ h(3) \\ h(4) \end{bmatrix} = \begin{bmatrix} 0 \\ h_{2009} - h_{2008} \\ h_{2015} - h_{2008} \\ h_{2016} - h_{2008} \\ h_{2015} - h_{2009} \\ h_{2016} - h_{2009} \\ h_{2016} - h_{2015} \end{bmatrix}, \tag{S2}$$

where $h(1)$ was zero by definition. We estimated $h(t)$ and its associated uncertainties using robust regression, corrected it for atmospheric pressure changes using the DAC, and derived the ice-shelf averaged time series (Figure 1) by taking the uncertainty-weighted mean value over the ice shelf.

Derivation of basal melt rates

We used Equation 1 to derive time-varying basal melt rates over the ice shelves. We estimated the height change rates *dh*/*dt* by smoothing the 23-year record of RA-derived heights h using a three-year moving average, taking a gradient, and smoothing the final height-change-rate time series *dh*/*dt* using the same three-year moving average filter. We used a three-year timescale to reduce the impact of high-frequency variability in h and h_s on w_b. We measured the uncertainties in our method for calculating *dh*/*dt* using a bootstrap technique (similar to the technique used in Paolo et al. 2015, 2016): integrating *dh*/*dt* to produce a smoothed time series of heights, computing the residuals between the smoothed heights and h, and resampling the residuals 1000 times to produce an ensemble of heights from which to calculate an ensemble of height change rates. The standard deviation of *dh*/*dt* was then estimated as the standard deviation of this ensemble. We applied the same technique to derive the uncertainties of dh_S/dt and combined them with the uncertainty due to the steady-state assumption used to spin-up the firn model, as described by Pritchard et al. (2012).

Ice thickness, advection, and divergence

From CryoSat-2-derived heights referenced to the WGS84 ellipsoid using the h_0 term in Equation S1, we calculated the freeboard, i.e., the height of the ice shelf above mean sea level (h_{msl}) using:

$$h_{msl} = h_0 - h_g - h_{mdt} - h_f - h_c, \tag{S3}$$

where h_g was the height of the EIGEN-6C4 geoid (Förste et al., 2014), h_{mdt} was mean dynamic topography from the DTU12MDT (an update of the model from Knudsen and Andersen, 2012), h_f was the firn air content using the IMAU firn densification model (Ligtenberg et al., 2011, 2014) coupled to RACMO 2.3p2 (Van Wessem et al., 2017) at 5.5 km horizontal spacing (Van

Wessem et al., 2016), and h_c was a correction using the 23-year RA height change record to reference h_{msl} to any given year. From this we derived the ice thickness H using

$$H = \frac{\rho_w h_{msl}}{\rho_i - \rho_w}, \tag{S4}$$

and the ice draft D using

$$D = \frac{\rho_w h_{msl}}{\rho_i - \rho_w} - h_{msl}. \tag{S5}$$

For $\bar{v}$, we used annual velocity mosaics from 2005 to 2015 derived from optical imagery from the Landsat-8 satellite and Synthetic Aperture Radar from the Sentinel-1, RADARSAT-2, ALOS-PALSAR, and TerraSAR-X satellites (Mouginot et al., 2017b,c). Within each grid cell used in the RA record, we constructed $\bar{v}H$ for each year where velocity data were available by referencing H to the acquisition time of $\bar{v}$. We obtain $\nabla \cdot (\bar{v}H)$ by fitting a plane to $\bar{v}H$ using

$$v_x H = a_{xx}x + a_{xy}y + \varepsilon \text{ and } v_y H = a_{yx}x + a_{yy}y + \varepsilon, \tag{S6}$$

from which $\nabla \cdot (\bar{v}H)$ within the grid cell was $a_{xx} + a_{yy}$, where the uncertainties in a_{xx} and a_{yy} are the uncertainties in the linear regression. We calculated the mean value from all years where $\nabla \cdot (\bar{v}H)$ was available, and the uncertainty in this steady-state assumption was the standard deviation between the annual values. We found that $\nabla \cdot (\bar{v}H)$ was relatively constant through time, even in regions with considerable changes in $\bar{v}$ (Figure S3). Therefore, while $\nabla \cdot (\bar{v}H)$ was a significant contributor to steady-state ice-shelf mass balance (Figure S3; Figure S4; Table 1), the impact of the steady-state assumption on derived time-variable melt rates (Figure 4; Figure S3) was minimal.

Surface mass balance

We defined M_s as a three-year moving average of surface mass balance (SMB) as simulated by the regional climate model RACMO2, version 2.3p2 (van Wessem et al., 2017) at 5.5 km horizontal spacing (Van Wessem et al., 2016), and we assumed a standard deviation of 15 percent of the SMB values. The standard deviation was determined from comparisons of RACMO2.3p2 SMB with in situ and radar-derived observations of SMB from Kuipers Munneke et al. (2017).

Basal melt rates

We then estimated basal melt rates w_b using

$$w_b = \frac{M_s}{\rho_i} - \frac{\rho_w}{(\rho_w - \rho_i)}\left(\frac{dh}{dt} - \frac{dh_s}{dt}\right) - \nabla \cdot (\bar{v}H), \tag{S7}$$

and the net mass balance M_{net} (in kg m^{-2} a^{-1}) using

$$M_{net} = \frac{\rho_w \rho_i}{(\rho_w - \rho_i)}\left(\frac{dh}{dt} - \frac{dh_s}{dt}\right). \tag{S8}$$

We reduced noise in the space domain by smoothing using a Gaussian filter with two-sigma dimensions equal to one RA grid cell size (Figures S4a-d), and calculated uncertainties by propagating the errors (Figures S5a-d). Mean values of mass balance in Table 1 are from the data shown in Figures S4a-d averaged over each ice shelf, with the associated variances being the ice-shelf averaged variances from the data shown in Figures S5a-d.

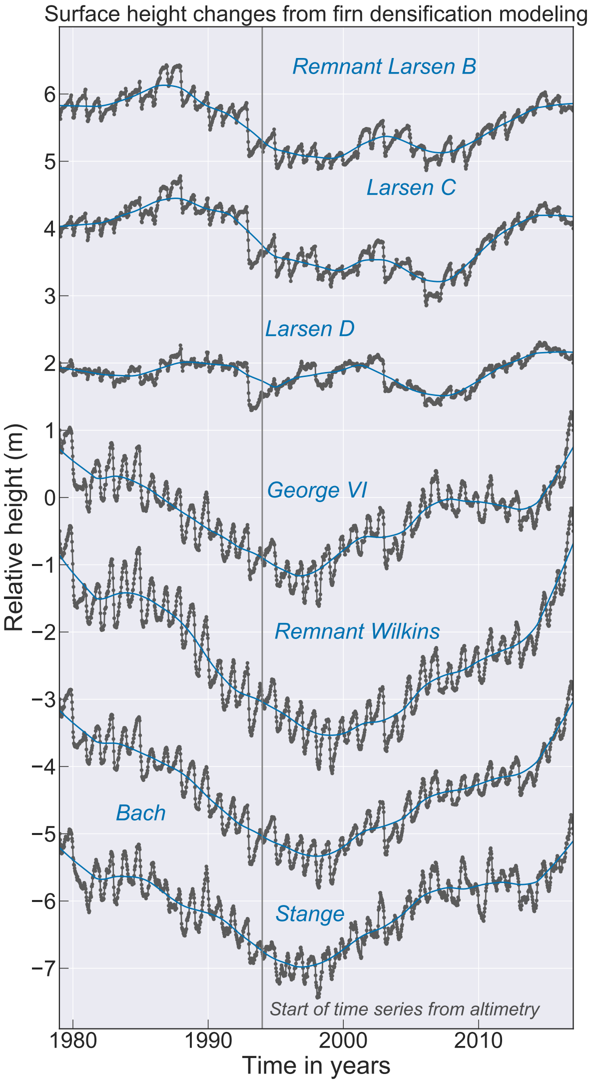

Figure S1. Surface height changes (in black) due to time-dependent changes in firn state as simulated by the IMAU-FDM firn model. Blue lines are three-year filtered averages. Vertical line in 1994 marks the start of RA height records. The firn densification model required that the net height change from the beginning (1979) to the end (2016) of the simulation be zero due to the steady-state assumption made to obtain a realistic initial firn column (Ligtenberg et al., 2011).

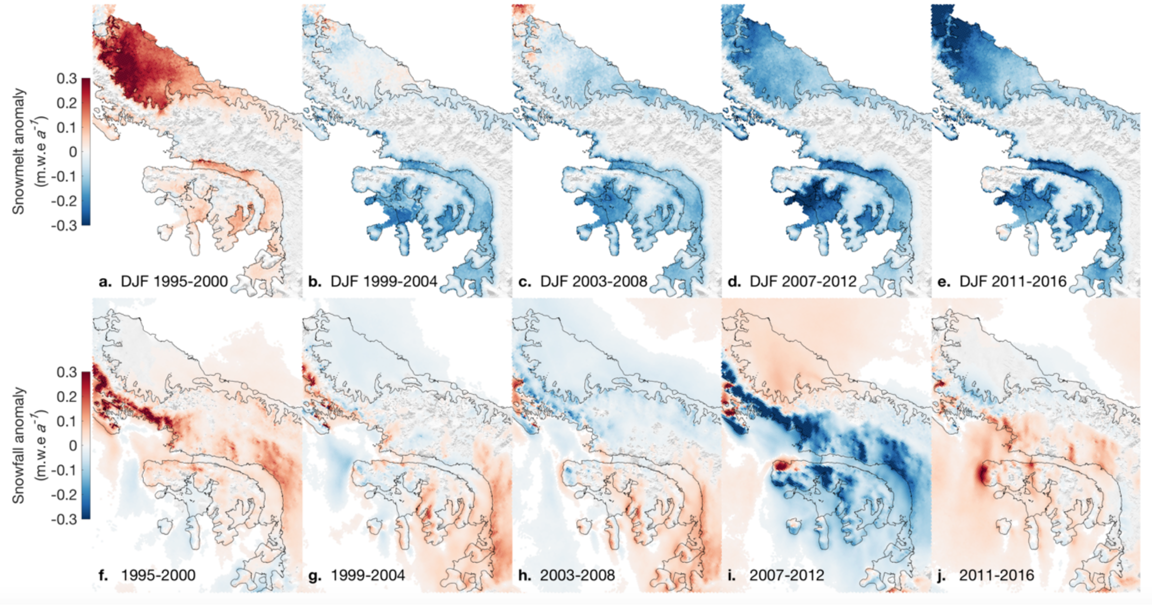

Figure S2. (a-e) Austral summer (December-January-February; DJF) surface melt anomalies and (f-j) annual snowfall anomalies, both relative to their 1979-2016 monthly-mean values, from the regional atmospheric model RACMO2.3p2 at 5.5 km horizontal spacing (Van Wessem et al., 2016).

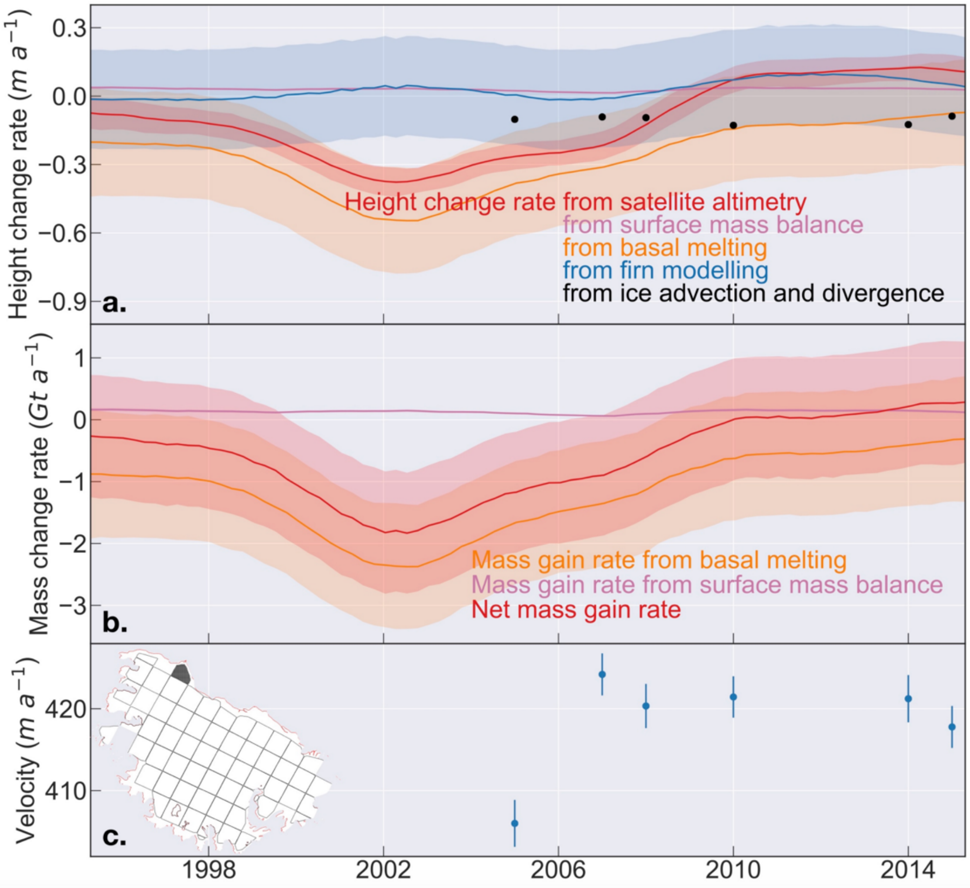

Figure S3. (a) Contributions of each ice-column process component to observed surface-height changes in the grid cell near Bawden Ice Rise (BIR; gray region in inset indicates location). The confidence intervals on the surface mass balance and on the ice advection and divergence components cannot be resolved in this plot. (b) Contributions of each component to mass changes at BIR. Shaded regions for (a) and (b) indicate 95% confidence intervals. (c) Velocities at BIR using annual velocity mosaics from Mouginot et al. (2017b,c). Error bars show 95% bounds on the median velocity variability within the BIR grid cell.

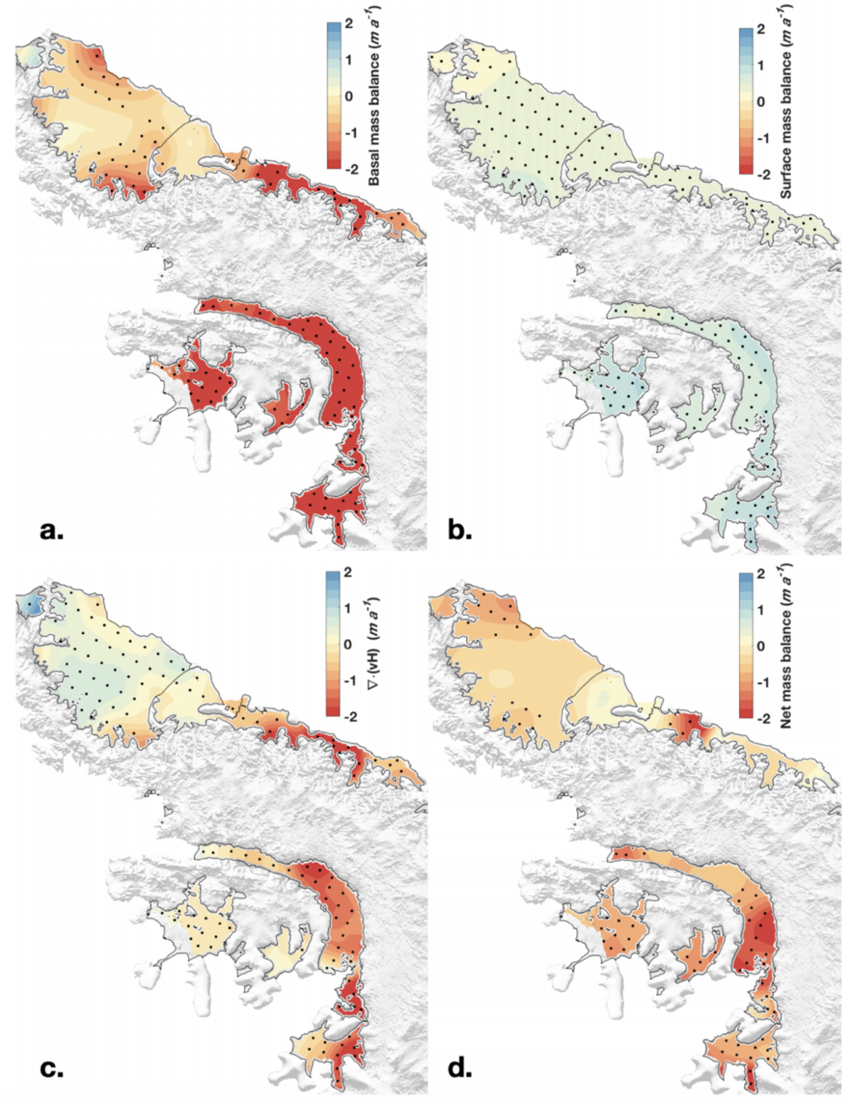

Figure S4. Components of Antarctic Peninsula ice-shelf mass balance, for the period 1994-2016. (a) Basal mass balance, same as Figure 2b, (b) surface mass balance, (c) ice advection and divergence, and (d) net mass balance, same as Figure 2c. Ice-shelf-averaged values are in Table 1. Stippling indicates locations of grid cells with rates above the 67% confidence interval.

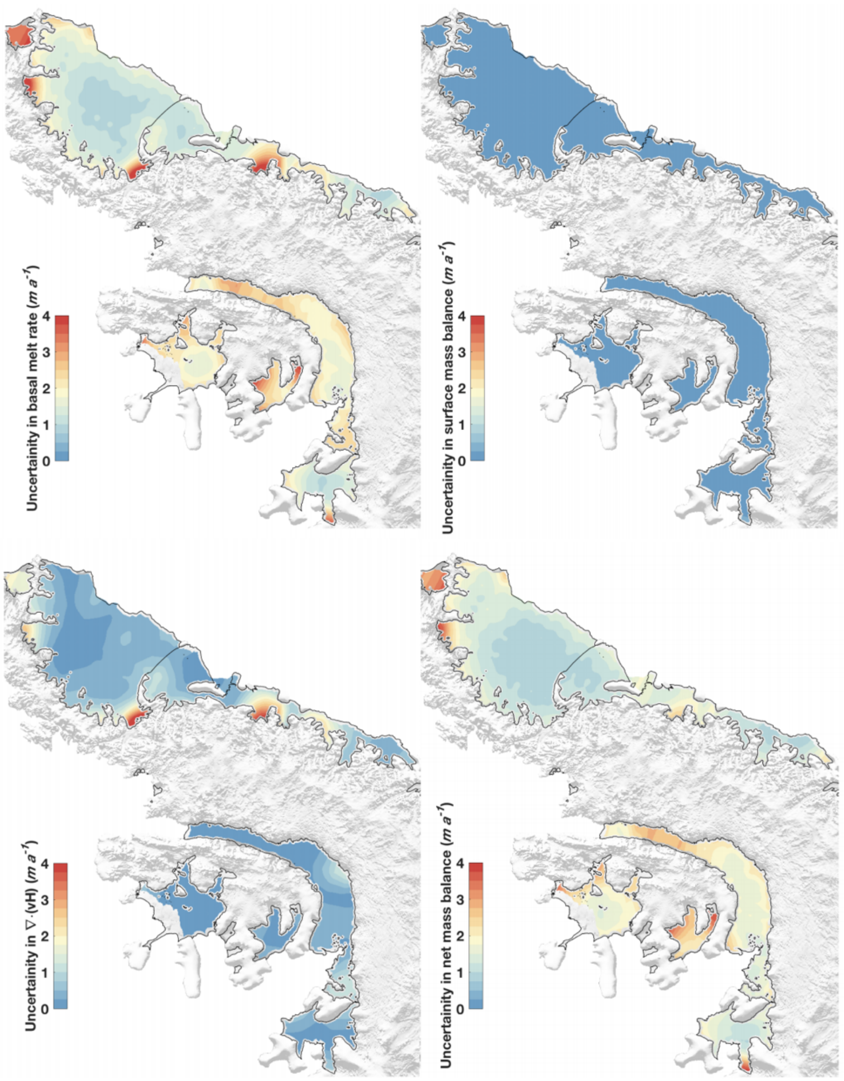

Figure S5. Uncertainties (95% confidence intervals) on the derived (a) basal melt rate and (b) surface mass balance (c) ice advection and divergence, and (d) net mass balance terms shown in Figure S4.

Table 1: Contributors to net ice-shelf mass budgets between 1994 and 2016. The area of each ice shelf was the net area covered by the grid cells used in this study, as defined by Paolo et al. (2015, 2016), which was smaller than the actual area of each ice shelf. Mass changes expressed as averaged values in m a^{-1} are based on an ice density of ρ_i=917 kg m^{-3}. The largest contributor to errors in the basal mass balance and net mass balance terms was the uncertainty in the net surface height change from firn variability.

Name	Area (sq. km)	Rate of mass change in Gt a^{-1} (m a^{-1}) for 1994-2016			
		Basal mass balance	Surface mass balance	Ice advection + divergence	Net
Larsen B	1880	0.8 ± 6 (0.4 ± 3.5)	0.18 ± 0.04 (0.11 ± 0.03)	2.3 ± 2.9 (1.3 ± 1.7)	-1.3 ± 5.4 (-0.8 ± 3)
Larsen C	44665	-21 ± 61 (-0.5 ± 1.4)	15 ± 2 (0.35 ± 0.05)	12 ± 34 (0.3 ± 0.8)	-18 ± 52 (-0.4 ± 1.3)
Larsen D	24228	-31 ± 36 (-1.4 ± 1.6)	8.5 ± 1.3 (0.38 ± 0.06)	-18 ± 25 (0.8 ± 1.1)	-5.5 ± 28 (-0.2 ± 1.3)
George VI	14686	-42 ± 26 (-3.2 ± 1.9)	9 ± 1 (0.7 ± 0.1)	-17 ± 6 (-1.3 ± 0.4)	-16 ± 25 (-1.2 ± 1.8)
Remnant Wilkins	6480	-11 ± 12 (-1.9 ± 2.0)	5.1 ± 0.7 (0.9 ± 0.1)	-0.7 ± 0.7 (-0.1 ± 0.1)	-5 ± 11 (-0.9 ± 1.9)
Bach	4579	-7 ± 11 (-1.7 ± 2.6)	2.4 ± 0.5 (0.6 ± 0.1)	-0.03 ± 0.24 (-0.1 ± 1.0)	-5 ± 11 (-1 ± 3)
Stange	8104	-24 ± 14 (-3.2 ± 1.5)	6.5 ± 0.8 (0.9 ± 0.1)	-9 ± 3 (-1.2 ± 0.4)	-9 ± 14 (-1.1 ± 1.5)

Chapter 3, in full, is a reprint of the material as it appears in the journal Geophysical Research Letters. Adusumilli, S., Fricker, H. A., Siegfried, M. R., Padman, L., Paolo, F. S., & Ligtenberg, S. R. (2018). Variable basal melt rates of Antarctic Peninsula ice shelves, 1994–2016. *Geophysical Research Letters*, 45(9), 4086-4095. The dissertation author was the primary investigator and author of this paper.

3.7 References

Arblaster, J. M., and G. A. Meehl (2006), Contributions of external forcings to southern annular mode trends, *Journal of Climate*, *19*(12), 2896–2905.

Blair, J. B., D. L. Rabine, and M. A. Hofton (1999), The Laser Vegetation Imaging Sensor: a medium-altitude, digitisation-only, airborne laser altimeter for mapping vegetation and topography, *ISPRS Journal of Photogrammetry and Remote Sensing*, *54*(2), 115–122.

Blair, J. B. and M. Hofton. 2010, updated 2016, *IceBridge LVIS L2 Geolocated Surface Elevation Product, Version 1*, Boulder, Colorado USA, NASA National Snow and Ice Data Center Distributed Active Archive Center. (Date Accessed: August 2017).

Borstad, C., E. Rignot, J. Mouginot, and M. Schodlok (2013), Creep deformation and buttressing capacity of damaged ice shelves: theory and application to Larsen C ice shelf, *The Cryosphere*, *7*(6).

Borstad, C., D. McGrath, and A. Pope (2017), Fracture propagation and stability of ice shelves governed by ice shelf heterogeneity, *Geophysical Research Letters*, *44*(9), 4186– 4194.

Cook, A. J., and D. G. Vaughan (2010), Overview of areal changes of the ice shelves on the Antarctic Peninsula over the past 50 years, *The Cryosphere.*, *4*(1), 77–98.

Dee, D.P., Uppala, S.M., Simmons, A.J., Berrisford, P., Poli, P., Kobayashi, S., Andrae, U., Balmaseda, M.A., Balsamo, G., Bauer, D.P. and Bechtold, P. (2011). The ERA‐Interim reanalysis: Configuration and performance of the data assimilation system. Quarterly Journal of the royal meteorological society, 137(656), pp.553-597.

Depoorter, M. A., J. L. Bamber, J. Griggs, J. T. M. Lenaerts, S. R. M. Ligtenberg, M. R. van den Broeke, and G. Moholdt (2013), Synthesized grounding line and ice shelf mask for Antarctica, doi:10.1594/PANGAEA.819151.

Dinniman, M. S., J. M. Klinck, and E. E. Hofmann (2012), Sensitivity of Circumpolar Deep Water transport and ice shelf basal melt along the west Antarctic Peninsula to changes in the winds, *J. Climate*, *25*(14), 4799-4816.

Dinniman, M. S., J. M. Klinck, and W. O. Smith (2011), A model study of Circumpolar Deep Water on the West Antarctic Peninsula and Ross Sea continental shelves, *Deep Sea Research Part II: Topical Studies in Oceanography*, *58*(13), 1508–1523.

Dupont, T., and R. Alley (2005), Assessment of the importance of ice-shelf buttressing to ice-sheet flow, *Geophysical Research Letters*, *32*(4).

Dutrieux, P., J. De Rydt, A. Jenkins, P. R. Holland, H. K. Ha, S. H. Lee, E. J. Steig, Q. Ding, E. P. Abrahamsen, and M. Schröder (2014), Strong sensitivity of Pine Island ice-shelf melting to climatic variability, *Science*, *343*(6167), 174-178.

Egbert, G. D., and S. Y. Erofeeva (2002), Efficient inverse modeling of barotropic ocean tides, *Journal of Atmospheric and Oceanic Technology*, *19*(2), 183–204.

Egbert, G. D., A. F. Bennett, and M. G. Foreman (1994), TOPEX/POSEIDON tides esti- mated using a global inverse model, *Journal of Geophysical Research: Oceans*, *99*(C12), 24,821–24,852.

Fricker, H. A., and L. Padman (2012), Thirty years of elevation change on Antarctic Peninsula ice shelves from multimission satellite radar altimetry, *Journal of Geophysical Research: Oceans*, *117*(C2).

Hogg, A. E., and G. H. Gudmundsson (2017), Impacts of the Larsen-C Ice Shelf calving event, *Nature Climate Change*, *7*(8), 540–542.

Hogg, A.E., Shepherd, A., Cornford, S.L., Briggs, K.H., Gourmelen, N., Graham, J.A., Joughin, I., Mouginot, J., Nagler, T., Payne, A.J. and Rignot, E. (2017). Increased ice flow in Western Palmer Land linked to ocean melting. Geophysical Research Letters, 44(9), pp.4159-4167.

Holland, P. R., A. Jenkins, and D. M. Holland (2010), Ice and ocean processes in the Bellingshausen Sea, Antarctica, *Journal of Geophysical Research: Oceans*, *115*(C5).

Holland, P. R., H. F. Corr, H. D. Pritchard, D. G. Vaughan, R. J. Arthern, A. Jenkins, and M. Tedesco (2011), The air content of Larsen ice shelf, *Geophysical Research Letters*, *38*(10).

Holland, P. R., A. Brisbourne, H. F. J. Corr, Daniel Mcgrath, K. Purdon, J. Paden, H. A. Fricker, F. S. Paolo, and A. H. Fleming (2015), Oceanic and atmospheric forcing of Larsen C Ice-Shelf thinning, *The Cryosphere*, *9*,1005-1024.

Holt, T., N. Glasser, H. Fricker, L. Padman, A. Luckman, O. King, D. Quincey, and M. Siegfried (2014), The structural and dynamic responses of Stange Ice Shelf to recent environmental change, *Antarctic Science*, *26*(6), 646–660.

Holt, T. O., N. F. Glasser, D. J. Quincey, and M.R. Siegfried (2013), Speedup and fracturing of George VI Ice Shelf, Antarctic Peninsula, *The Cryosphere*, *7*(3), 797.

Jenkins, A. (2011), Convection-driven melting near the grounding lines of ice shelves and tidewater glaciers, *Journal of Physical Oceanography*, *41*(12), 2279–2294.

Khazendar, A., M.P. Schodlok, I. Fenty, S.R.M. Ligtenberg, E. Rignot, and M.R. van den Broeke (2013), Observed thinning of Totten Glacier is linked to coastal polynya variability. *Nature communications*, *4*(2857), 1-9.

Khazendar, A., C. P. Borstad, B. Scheuchl, E. Rignot, and H. Seroussi (2015), The evolving instability of the remnant Larsen B Ice Shelf and its tributary glaciers, *Earth and Planetary Science Letters*, *419*, 199–210.

Kim, T., H. Ha, A. Wåhlin, S. Lee, C. Kim, J. Lee, and Y. Cho (2017), Is Ekman pumping responsible for the seasonal variation of warm circumpolar deep water in the Amundsen Sea?, *Continental Shelf Research*, *132*, 38–48.

Knudsen, P., and B. Andersen (2012), A global mean ocean circulation estimation using GOCE gravity models - The DTU12MDT mean dynamic topography model.

Krabill, W., W. Abdalati, E. Frederick, S. Manizade, C. Martin, J. Sonntag, R. Swift, R. Thomas, and J. Yungel (2002), Aircraft laser altimetry measurement of elevation changes of the Greenland ice sheet: Technique and accuracy assessment, *Journal of Geodynamics*, *34*(3), 357–376.

Kuipers Munneke, P., S. R. Ligtenberg, M. R. Van Den Broeke, and D. G. Vaughan (2014), Firn air depletion as a precursor of Antarctic ice-shelf collapse, *Journal of Glaciology*, *60*(220), 205–214.

Kuipers Munneke, P., D. McGrath, B. Medley, A. Luckman, S. Bevan, B. Kulessa, D. Jansen, A. Booth, P. Smeets, B. Hubbard, D. Ashmore, M. Van den Broeke, H. Sevestre, K. Stef- fen, A. Shepherd, and N. Gourmelen (2017), Observationally constrained surface mass balance of Larsen C ice shelf, Antarctica, *The Cryosphere*, *11*(6), 2411–2426.

Ligtenberg, S., M. Helsen, and M. Van den Broeke (2011), An improved semi-empirical model for the densification of Antarctic firn, *The Cryosphere*, *5*(4), 809.

Ligtenberg, S., P. Kuipers Munneke, and M. Van den Broeke (2014), Present and future variations in Antarctic firn air content, *The Cryosphere*, *8*(5), 1711–1723.

McMillan, M., A. Shepherd, A. Sundal, K. Briggs, A. Muir, A. Ridout, A. Hogg, and D. Wingham (2014), Increased ice losses from Antarctica detected by CryoSat-2, *Geo- physical Research Letters*, *41*(11), 3899–3905.

Morris, E. M., and D. G. Vaughan (2003), Spatial and temporal variation of surface temperature on the Antarctic Peninsula and the limit of viability of ice shelves, *Antarctic Research Series*, *79*, 61-68, doi:10.1029/AR079p0061.

Mouginot, J., B. Scheuchl, and E. Rignot (2017a), Measures Antarctic boundaries for IPY 2007-2009 from satellite radar, version 2., Ice Shelf Polygons.

Mouginot, J., E. Rignot, B. Scheuchl, and R. Millan (2017b), Comprehensive Annual Ice Sheet Velocity Mapping Using Landsat-8, Sentinel-1, and RADARSAT-2 Data, *Remote Sensing*, *9*(4), 364.

Mouginot, J., B. Scheuchl, and E. Rignot (2017c), MEaSUREs Annual Antarctic Ice Velocity Maps 2005-2017, Version 1, Boulder, Colorado USA, NASA National Snow and Ice Data Center Distributed Active Archive Center. (Last accessed September 2017).

Mueller, R. D., T. Hattermann, S. L. Howard, and L. Padman (2018), Tidal influences on a future evolution of the Filchner-Ronne Ice Shelf cavity in the Weddell Sea, Antarctica, *The Cryosphere*, *12*(2), 453-476, doi:10.5194/tc-2017-110.

Nicholls, K., C. Pudsey, and P. Morris (2004), Summertime water masses off the northern Larsen C Ice Shelf, Antarctica, *Geophysical Research Letters*, *31*(9).

Nilsson, J., P. Vallelonga, S. B. Simonsen, L. S. SÃÿrensen, R. Forsberg, D. Dahl-Jensen, M. Hirabayashi, K. Goto-Azuma, C. S. Hvidberg, H. A. Kjãęr, and K. Satow (2015), Greenland 2012 melt event effects on CryoSat-2 radar altimetry, *Geophysical Research Letters*, *42*(10), 3919–3926, doi:10.1002/2015GL063296.

Padman, L., H. A. Fricker, R. Coleman, S. Howard, and L. Erofeeva (2002), A new tide model for the Antarctic ice shelves and seas, *Annals of Glaciology*, *34*(1), 247–254.

Padman, L., M. King, D. Goring, H. Corr, and R. Coleman (2003), Ice-shelf elevation changes due to atmospheric pressure variations, *Journal of Glaciology*, *49*(167), 521–526.

Padman, L., Costa, D.P., Dinniman, M.S., Fricker, H.A., Goebel, M.E., Huckstadt, L.A., Humbert, A., Joughin, I., Lenaerts, J.T., Ligtenberg, S.R. and Scambos, T. (2012). Oceanic controls on the mass balance of Wilkins Ice Shelf, Antarctica. Journal of Geophysical Research: Oceans, 117(C1).

Paolo, F. S., H. A. Fricker, and L. Padman (2015), Volume loss from Antarctic ice shelves is accelerating, *Science*, *348*(6232), 327–331.

Paolo, F. S., H. A. Fricker, and L. Padman (2016), Constructing improved decadal records of Antarctic ice shelf height change from multiple satellite radar altimeters, *Remote Sensing of Environment*, *177*, 192–205.

Paolo, F. S., L. Padman, H. A. Fricker, S. Adusumilli, S. Howard, and M. R. Siegfried, (2018). Response of Pacific-sector Antarctic ice shelves to the El Niño/Southern Oscillation. *Nature Geoscience*, *11*, 121-126.

Pritchard, H. D., R. J. Arthern, D. G. Vaughan, and L. A. Edwards (2009), Extensive dynamic thinning on the margins of the Greenland and Antarctic ice sheets, *Nature*, *461*(7266), 971–975.

Pritchard, H., S. Ligtenberg, H. Fricker, D. Vaughan, M. Van den Broeke, and L. Padman (2012), Antarctic ice-sheet loss driven by basal melting of ice shelves, *Nature*, *484*(7395), 502–505.

Raney, R. K. (1998), The delay/Doppler radar altimeter, *IEEE Transactions on Geoscience and Remote Sensing*, *36*(5), 1578–1588.

Rignot, E., G. Casassa, P. Gogineni, W. Krabill, A. Rivera, and R. Thomas (2004), Accelerated ice discharge from the Antarctic Peninsula following the collapse of Larsen B ice shelf, *Geophysical Research Letters*, *31*(18).

Rignot, E., S. Jacobs, J. Mouginot, and B. Scheuchl (2013), Ice-shelf melting around Antarctica, *Science*, *341*(6143), 266–270.

Scambos, T. A., Hulbe, C., Fahnestock, M., & Bohlander, J. (2000), The link between climate warming and break-up of ice shelves in the Antarctic Peninsula, *Journal of Glaciology*, *46*(154), 516-530.

Scambos, T. A., J. Bohlander, C. U. Shuman, and P. Skvarca (2004), Glacier acceleration and thinning after ice shelf collapse in the Larsen B embayment, Antarctica, *Geophysical Research Letters*, *31*(18).

Scambos, T., T. Haran, M. Fahnestock, T. Painter, and J. Bohlander (2007), MODIS-based Mosaic of Antarctica (MOA) data sets: Continent-wide surface morphology and snowgrain size, *Remote Sensing of Environment*, *111*(2), 242–257.

Scambos, T., Fricker, H.A., Liu, C.C., Bohlander, J., Fastook, J., Sargent, A., Massom, R. and Wu, A.M., 2009. Ice shelf disintegration by plate bending and hydro-fracture: Satellite observations and model results of the 2008 Wilkins ice shelf break-ups. *Earth and Planetary Science Letters*, *280*(1-4), pp.51-60.

Schmidtko, S., K.J. Heywood, A.F. Thompson, and S. Aoki (2014), Multidecadal warming of Antarctic waters, *Science* 346, no. 6214, 1227-1231.

Siegfried, M. R., H. A. Fricker, M. Roberts, T. A. Scambos, and S. Tulaczyk (2014), A decade of West Antarctic subglacial lake interactions from combined ICESat and CryoSat-2 altimetry, *Geophysical Research Letters*, *41*(3), 891–898.

Shepherd, A., D. Wingham, T. Payne, and P. Skvarca (2003), Larsen ice shelf has progressively thinned, *Science*, *302*(5646), 856–859.

Studinger, M. S. 2013, updated 2017, *IceBridge ATM L1B Elevation and Return Strength, Version 2*, Boulder, Colorado USA, NASA National Snow and Ice Data Center Distributed Active Archive Center. (Date Accessed: August 2017).

Thomas, R., C. Davis, E. Frederick, W. Krabill, Y. Li, S. Manizade, and C. Martin (2008), A comparison of Greenland ice-sheet volume changes derived from altimetry measurements, *Journal of Glaciology*, *54*(185), 203–212.

Thompson, D. W., and S. Solomon (2002), Interpretation of recent Southern Hemisphere climate change, *Science*, *296*(5569), 895–899.

Turner, J., H. Lu, I. White, J. C. King, T. Phillips, J. S. Hosking, T. J. Bracegirdle, G. J. Marshall, R. Mulvaney, and P. Deb (2016), Absence of 21st century warming on Antarctic Peninsula consistent with natural variability, *Nature*, *535*(7612), 411–415.

Van Wessem, J. M., S.R.M. Ligtenberg, C.H. Reijmer, W.J. van de Berg, M.R. van den Broeke, N.E. Barrand, E.R. Thomas, J. Turner, J. Wuite, T.A. Scambos, and E. van Meijgaard (2016), The modelled surface mass balance of the Antarctic Peninsula at 5.5 km horizontal resolution, *The Cryosphere, 10*(1), 271-285.

Wessem, J.M.V., Berg, W.J.V.D., Noël, B.P., Meijgaard, E.V., Amory, C., Birnbaum, G., Jakobs, C.L., Krüger, K., Lenaerts, J., Lhermitte, S. and Ligtenberg, S.R. (2018). Modelling the climate and surface mass balance of polar ice sheets using RACMO2–Part 2: Antarctica (1979–2016). The Cryosphere, 12(4), pp.1479-1498.

Wingham, D.J., Francis, C.R., Baker, S., Bouzinac, C., Brockley, D., Cullen, R., de Chateau-Thierry, P., Laxon, S.W., Mallow, U., Mavrocordatos, C. and Phalippou, L. (2006). CryoSat: A mission to determine the fluctuations in Earth's land and marine ice fields. Advances in Space Research, 37(4), pp.841-871.

Chapter 4

Interannual variations in meltwater input to the Southern Ocean from Antarctic ice shelves

Abstract

Ocean-driven basal melting of Antarctica's floating ice shelves accounts for about half of their mass loss in steady state, where gains in ice-shelf mass are balanced by losses. Ice-shelf thickness changes driven by varying basal melt rates modulate mass loss from the grounded ice sheet and its contribution to sea level, and the changing meltwater fluxes influence climate processes in the Southern Ocean. Existing continent-wide melt-rate datasets have no temporal variability, introducing uncertainties in sea level and climate projections. Here, we combine surface height data from satellite radar altimeters with satellite-derived ice velocities and a new model of firn-layer evolution to generate a high-resolution map of time-averaged (2010–2018) basal melt rates and time series (1994–2018) of meltwater fluxes for most ice shelves. Total basal meltwater flux in 1994 (1,090 ± 150 Gt yr^{-1}) was similar to the steady-state value (1,100 ± 60 Gt yr^{-1}), but increased to 1,570 ± 140 Gt yr^{-1} in 2009, followed by a decline to 1,160 ± 150 Gt yr^{-1} in 2018. For the four largest 'cold-water' ice shelves, we partition meltwater fluxes into deep and shallow sources to reveal distinct signatures of temporal variability, providing insights into climate forcing of basal melting and the impact of this melting on the Southern Ocean.

4.1 Introduction

The mass budget of the Antarctic Ice Sheet is controlled primarily by mass gain from net snow accumulation and mass loss from basal melting and iceberg calving of its floating ice shelves. These mass loss processes act to maintain the ice shelf in steady state; however, many ice shelves are experiencing net mass loss (e.g., Pritchard et al., 2012) and thinning (e.g., Paolo et al., 2015) due to ocean-driven basal melting in excess of the steady-state values. Confined ice shelves reduce the speed of grounded ice flowing into them by exerting back-stress from sidewall friction and basal pinning points, a process called “buttressing” (e.g., Thomas et al., 1979). Excess basal melting in recent decades has reduced buttressing and increased dynamic mass loss of grounded ice, which has increased Antarctica’s contribution to sea level rise (e.g., Jenkins et al., 2018; Nerem et al., 2018).

Ice shelf melting has been categorized into three modes corresponding to distinct oceanographic processes (e.g., Jacobs et al., 1992). Mode 1 melting occurs at the deep grounding lines of ‘cold-water’ ice shelves, and is driven by inflows of cold, dense High Salinity Shelf Water (HSSW) that is produced through sea ice formation on the continental shelf (e.g., Nicholls, 1997). Rising plumes of buoyant and potentially supercooled meltwater (referred to as Ice Shelf Water; ISW) formed from Mode 1 melting can lead to refreezing downstream, creating a layer of marine ice on the ice shelf base (e.g., Lewis & Perkin, 1986). Mode 2 melting occurs at ‘warm-water’ ice shelves where a subsurface layer of warm Circumpolar Deep Water (CDW) or modified CDW (mCDW) is transported into the ice-shelf cavity. Mode 3 melting occurs near the ice front where seasonally warmed Antarctic Surface Water (AASW) can be transported under shallow ice by tides and other ocean variability. The relative contributions of these modes to total melting are highly variable around Antarctica, both in space and time, since each mode is influenced by several external processes including regional atmospheric and oceanic conditions and the production and transport of sea ice (e.g., Rintoul, 2018; Turner et al., 2017).

The changing net fluxes and distribution of freshwater from ice shelf basal melting influence other components of the climate system through processes such as the production and extent of sea ice, which modifies the exchange of heat, freshwater, and gases (e.g., CO_2) between the atmosphere and Southern Ocean (Merino et al., 2018; Pauling et al., 2017); formation of Antarctic Bottom Water that is a major driver of the global ocean overturning circulation (Fogwill et al., 2015); and generation of nearshore coastal currents that advect freshwater and other tracers to connect different regions around Antarctica (Moffat et al., 2008; Nakayama et al., 2014). Despite the projected impacts of changes in ice shelf melting on Southern Ocean dynamics and global climate variability (Golledge et al., 2019), the current generation of global climate models such as those used in the Coupled Model Intercomparison Project (Eyring et al., 2016) do not include realistic representations of meltwater fluxes (Jourdain et al., 2019).

4.2 Satellite-derived estimates of basal melt rates

Currently, the best available circum-Antarctic datasets for ice shelf basal melt rate are derived from Ice, Cloud and land Elevation Satellite (ICESat) laser altimetry acquired during 2003-2008 (Depoorter et al., 2013; Rignot et al., 2013). These estimates are six-year averages for the satellite's operational period, with no information about temporal variability. Although ICESat's orbit to 86°S sampled all Antarctic ice shelves, it had relatively wide cross-track spacing, particularly for the northerly ice shelves (Figure S1). Existing data therefore cannot capture critical properties of meltwater fluxes from ice shelves, such as small spatial scales of melting in channels (Dutrieux et al., 2013; Gourmelen et al., 2017) or the large decadal variability inferred from oceanographic observations in West Antarctica (Jenkins et al., 2018).

A sequence of four European Space Agency satellite missions carrying radar altimeters have continuously acquired ranging data that allow us to estimate surface height change over Antarctica's ice shelves from 1994 to 2018: ERS-1, ERS-2, and Envisat (1992–2010) to 81.5°S and CryoSat-2 (2010–) to 88°S. CryoSat-2 samples all ice shelf areas, with higher track density than prior altimeters (Figure S1). Together with its innovative Synthetic Aperture Radar-Interferometric (SARIn) mode of operation (Wingham, 2002), the orbit for CryoSat-2 allows for estimating height change with higher spatial resolution and accuracy than the previous radar altimeters (Gourmelen et al., 2017). Here, we estimate time-averaged (over eight years; 2010–2018) basal melt rates at high spatial resolution (500-m grid cells) for all ice shelves where sufficient data are available by combining height changes from CryoSat-2 radar altimetry with satellite-derived ice velocities and a new model of surface mass balance and firn state variability (Methods). We then use the continuous height record from the four altimetry missions to estimate basal melt rates in 10-km grid cells for every year from 1994 to 2018 for all Antarctic ice shelf regions where sufficient data are available.

4.3 Spatial distribution of basal melt rates

The spatial distribution of time-averaged ice-shelf melt rates around Antarctica during 2010–2018 (Figure 1) shows large differences between cold- and warm-water ice shelves. Cold-water ice shelves (such as Ross, Ronne, Filchner and Amery) show high melt rates under deep ice drafts near grounding lines and shallower ice drafts near ice fronts (Figure 1, ice draft shown in Figure S2) separated by zones of refreezing. Warm-water ice shelves such as those in the

Amundsen and Bellingshausen seas typically have high melt rates, consistent with the higher values of thermal forcing (temperature above the pressure-dependent, in situ freezing point of seawater) found near their ice fronts.

Area-integrated meltwater fluxes binned by ice draft for four cold-water and two warm-water ice shelves (Figure 2) provide further insight into the different modes of melting occurring at different locations. Melting for regions of deep ice draft under the large cold-water ice shelves is dominated by Mode 1 processes. In steady state, refreezing rates can be high, and about half of all Mode 1 meltwater produced under Ronne Ice Shelf and about a fifth of all meltwater produced under Amery Ice Shelf is subsequently refrozen as marine ice. The predicted thickness of marine ice estimated from our refreezing rates for Ronne and Amery ice shelves agrees well with independent estimates from airborne radar sounding and satellite radar altimetry (Figure S3). Refreezing typically starts at ice drafts that are around 50% of the grounding line depth, consistent with predictions from idealized models that use buoyant plume theory (Holland et al., 2007; Lane-Serff, 1995). The ranges of ice draft for regions with refreezing (Figure 2) also correspond with the approximate depths for the subsurface plumes of cold ISW found along ice fronts (Foldvik, 2004; Herraiz-Borreguero et al., 2016; Smethie & Jacobs, 2005), which subsequently contribute to the formation of AABW (Schlosser et al., 1990).

Cold-water ice shelves also have regions of relatively high basal melt rates under shallower ice along the ice fronts (Figure 1, 2), primarily due to Mode 3 melting. Unlike regions undergoing Mode 1 melting that are close to the deep grounding lines where ice shelf thinning could substantially reduce buttressing (Goldberg et al., 2019; Reese et al., 2018), regions of Mode 3 melting are typically within the “passive ice zones” (Fürst et al., 2016) that provide little buttressing to grounded ice. However, the elevated melt rates contribute to increased ocean stratification along the ice front that influences cross-front exchanges of ocean heat (Malyarenko et al., 2019) and the seasonal cycle of sea ice formation close to the ice front (Porter et al., 2019), both of which feed back into the seasonal cycle of ice-shelf melt (Stewart et al., 2019; Tinto et al., 2019).

Under warm-water ice shelves, high melt rates are associated with subsurface flows of CDW and mCDW (Mode 2 melting). Melting in excess of steady state caused rapid thinning of several warm-water ice shelves in the Amundsen and Bellingshausen Sea sectors during 2010–2018 (Figure S4). For some ice shelves in these sectors (e.g., George VI, Wilkins, and Dotson) the highest rates of thinning occurred in narrow basal channels with high melt rates. Getz Ice Shelf, the largest single source of meltwater from the Antarctic ice shelves (Table 1), shows excess melting at depths between 250 m and 700 m (Figure 2). Warm-water ice shelves outside the Amundsen and Bellingshausen seas sector, such as Totten Ice Shelf in East Antarctica, show insignificant rates of excess melting.

4.4 Variations in ice shelf melt rates between 1994 and 2018

Our estimate for net mass loss from all of Antarctica’s ice shelves from 1994 to 2018 is 3960±1100 Gt (Figure 3a; error range is the 95% confidence interval, Methods). Most of this mass loss was from the Pacific Ocean Sector ice shelves. For reference, the net loss of grounded ice from the Antarctic Ice Sheet during 1992–2017 was 2,660 ± 560 Gt (The IMBIE Team, 2018). The total meltwater flux, based on the area-integrated basal melt rate over all Antarctic ice shelves averaged over 1994–2018, was 1,260 ± 150 Gt/yr, which was 160 ± 150 Gt/yr higher than the steady-state rate of 1,100 ± 60 Gt/yr (Figure 3b). Meltwater fluxes varied substantially with time: an increase of 480 ± 210 Gt/yr, from 1,090 ± 150 Gt/yr at the start of the record in

1994 to 1,570 ± 140 Gt/yr in 2009, was offset by a subsequent decrease of 410 ± 210 Gt/yr to 1,160 ± 150 Gt/yr in 2018. Our estimate of time-averaged meltwater flux for the ICESat-era (2003–2008) is 1,500 ± 140 Gt/yr, which is consistent with two previous ICESat-based estimates of 1,500 ± 240 Gt/yr (Rignot et al., 2013) and 1,450 ± 170 Gt/yr (Depoorter et al., 2013). The ICESat-era estimate of meltwater flux exceeds our 25-yr average by 240 ± 210 Gt/yr and exceeds our steady-state estimate by 400 ± 160 Gt/yr, highlighting the importance of long, continuous records to provide context to results from individual missions (Pritchard et al., 2012) or between two non-overlapping missions (Smith et al., 2020).

We examined the temporal variability in melt rates from different modes for the four largest cold-water ice shelves by calculating spatial averages over select regions (Figure 4a-d) of deep ice draft (Mode 1) and shallow draft (mostly Mode 3). For Ross Ice Shelf, the timing of the minimum in Mode 1 melt rates in Byrd Inlet near 2015 is consistent with the 2013-2014 minimum in HSSW salinity on the Ross Sea continental shelf (Castagno et al., 2019) and the time scale for advection of HSSW to Byrd Glacier (Tinto et al., 2019). Lower salinity for HSSW reduces the negative buoyancy driving HSSW under the ice front and downslope to the deep grounding line of Byrd Glacier, weakening the circulation of HSSW into Byrd Inlet and the resulting melting. Mode 1 melting of Filchner and Ronne ice shelves has been hypothesized to have increased following the formation of an exceptionally large polynya during the 1997–1998 austral summer (Nicholls & Østerhus, 2004). This hypothesis was based on a sharp decline in ocean temperatures at an instrumented site (Site 5; Figure S5) on Ronne Ice Shelf near the southwestern Berkner Island coast between 2000 and 2003, attributed (Nicholls & Østerhus, 2004) to increased ISW formation following a period of high Mode 1 melting. Our data also support this hypothesis, with increased melt rates at deep ice drafts under Filchner Ice Shelf during 1999-2000 and decreased melt rates (including a short-lived transition to refreezing) at Site 5 between 2000 and 2004 (Figure S5). Melt rates of Amery Ice Shelf, spatially averaged for deep ice drafts, varied from near 0 to 6.5 m yr^{-1} with particularly high values between 2003 and 2007. We speculate that this maximum could be associated with a continuous drainage of a ~0.8 km^3 subglacial lake under Lambert Glacier between 2003 and 2006 (Smith et al., 2009); subglacial discharge is known to drive energetic plumes (Motyka et al., 2013; Washam et al., 2019) that increase basal melt rates near grounding lines.

For Amundsen Sea ice shelves, melt rates showed substantial variability, with the highest sustained rates occurring in the late 2000s (Figure 4e). Variability in Mode 2 melting of Amundsen Sea ice shelves has been previously identified in ocean observations and linked to variability in the tropical Pacific at both interannual (Dutrieux et al., 2014; Paolo et al., 2018) and decadal (Jenkins et al., 2018) time scales. The magnitude of variability in our estimated melt rates of Dotson Ice Shelf (around 60 Gt/yr peak to trough) is consistent with the variability in independent estimates of meltwater flux from repeated oceanographic sections along the ice-shelf front (Jenkins et al., 2018) (Figure S6) but is larger than the variability expected from an ocean model that used atmospheric forcing from the same period (Kimura et al., 2017). Excess basal melting and changes in ice shelf extent (Figure S8, Table 1) in the Amundsen Sea sector between 1994 and 2018 could be due to a longer-term increase in the thickness of CDW incursions under ice shelf cavities associated with atmospheric and oceanic responses to anthropogenic forcing (Holland et al., 2019).

4.5 Summary

Our new estimates of time-varying melt rates allows assessment of whether ocean circulation models are adequately representing the complex feedbacks between water-mass production and conversion processes acting under the ice shelves and over the continental shelves offshore. The large temporal variability of melting in all three modes (Figure 4) will contribute to changes in the distribution of different water masses over the Antarctic continental shelf seas and into the global ocean. The ISW produced through Mode 1 melting contributes to the formation of particularly cold, dense forms of AABW (Budillon et al., 2011; Foldvik, 2004; Williams et al., 2016). Changes in Mode 2 and Mode 3 melting modify the fluxes of meltwater into the upper ocean in adjacent coastal regions (Nakayama et al., 2014; Porter et al., 2019). Increased ocean stratification from shallow sources of cold, buoyant water alters the seasonal cycle of sea ice (Petty et al., 2014) and decreases the potential for deep convection that drives production of Dense Shelf Water types including HSSW. Changes in relative strengths of these melt modes modify the geostrophic ocean circulation over the Antarctic continental shelf seas, feeding back into the transport of ocean heat between coastal sectors and into the sub-ice-shelf cavities (Nicholls, 1997).

We have produced two new datasets of basal melt rates for nearly all of Antarctica's ice shelves. One dataset provides melt rates at high spatial resolution (500 m grid) for most ice-shelf areas, averaged over the period 2010–2018. The second dataset allows for the evaluation of annual estimates of basal melt rates at lower spatial resolution (>10 km) for the period 1994–2018. Together, these datasets reveal large variability in total meltwater fluxes from individual Antarctic ice shelves, with distinct, regionally variable, signatures of temporal variability for different modes of ocean-driven melting. Our data provide insights into the glaciological and climate drivers of processes that modulate current ice-sheet mass loss, and improved metrics for calibration and validation of melt rates used in both ice–ocean and Earth-system models.

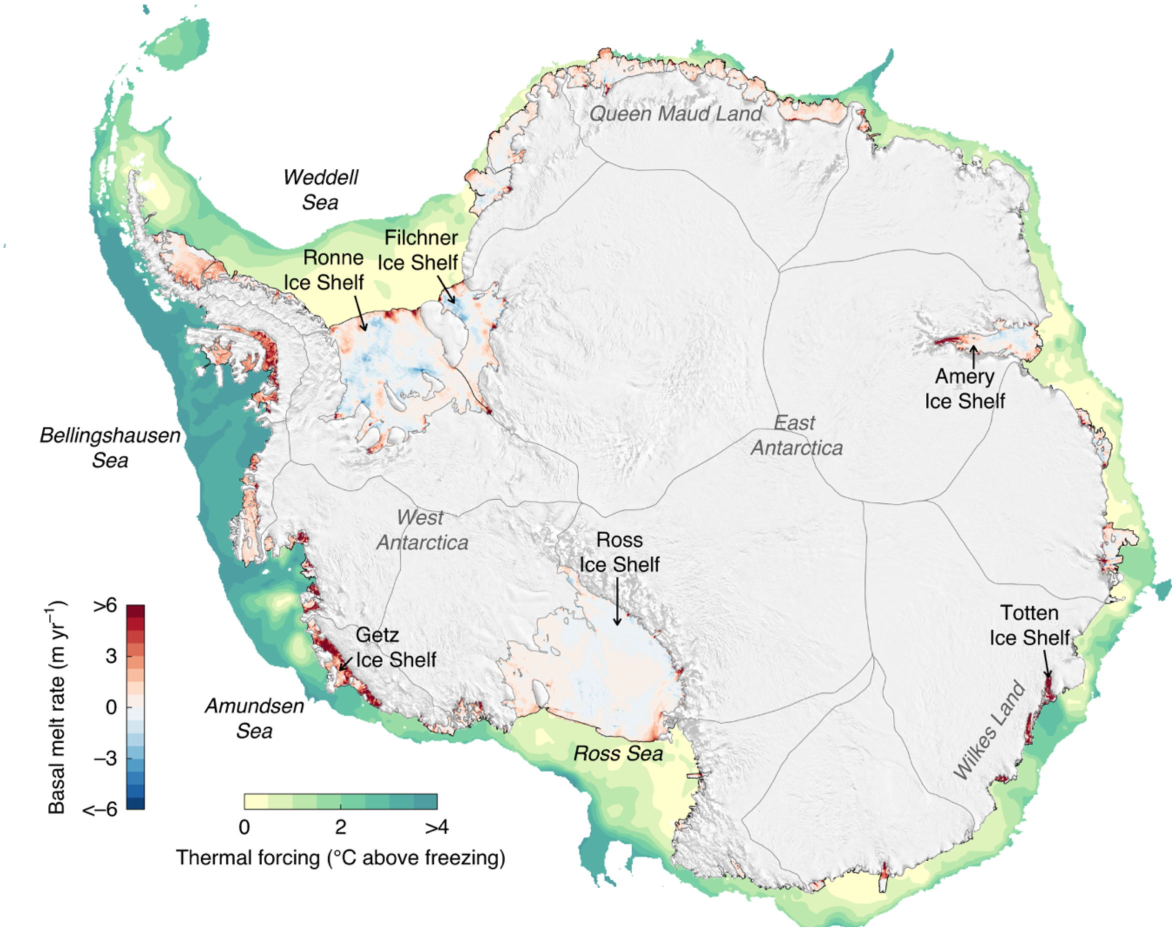

Figure 1. Basal melt rates of Antarctic ice shelves estimated using CryoSat-2 altimetry. Rates are averaged over 2010–2018. The units are m of ice equivalent per year, assuming an ice density of 917 kg m^{-3}. The thermal forcing, defined as the temperature above the in situ freezing point of seawater, is mapped for water depths <1,500 m. For water depths less than 200 m, the seafloor thermal forcing is shown, and for water depths >200 m, the maximum thermal forcing between 200 m and 800 m is shown (Methods).

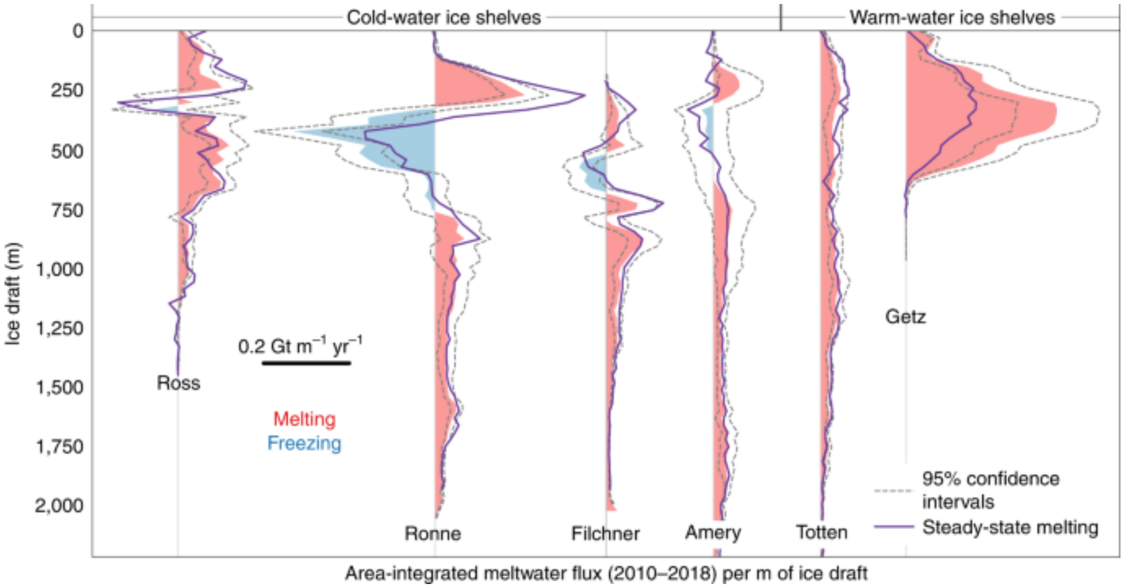

Figure 2. Vertical structure of melting and refreezing rates for selected ice shelves. Depth dependence of area-integrated meltwater flux (2010–2018) per m of ice-shelf draft (depth of the ice-shelf base below sea level) for six ice shelves (locations shown in Fig. 1). The scale for the horizontal axis is shown by the solid black line within the figure. The shaded regions in red and blue represent the mean values, and the dashed lines represent 95% confidence intervals. The purple lines are hypothetical steady-state meltwater fluxes (that is, the meltwater fluxes required to maintain constant ice-shelf mass). Warm-water ice shelves are distinguished from cold-water ice shelves by their higher average rates of meltwater production driven by intrusions of warm CDW or mCDW into the ice-shelf cavity.

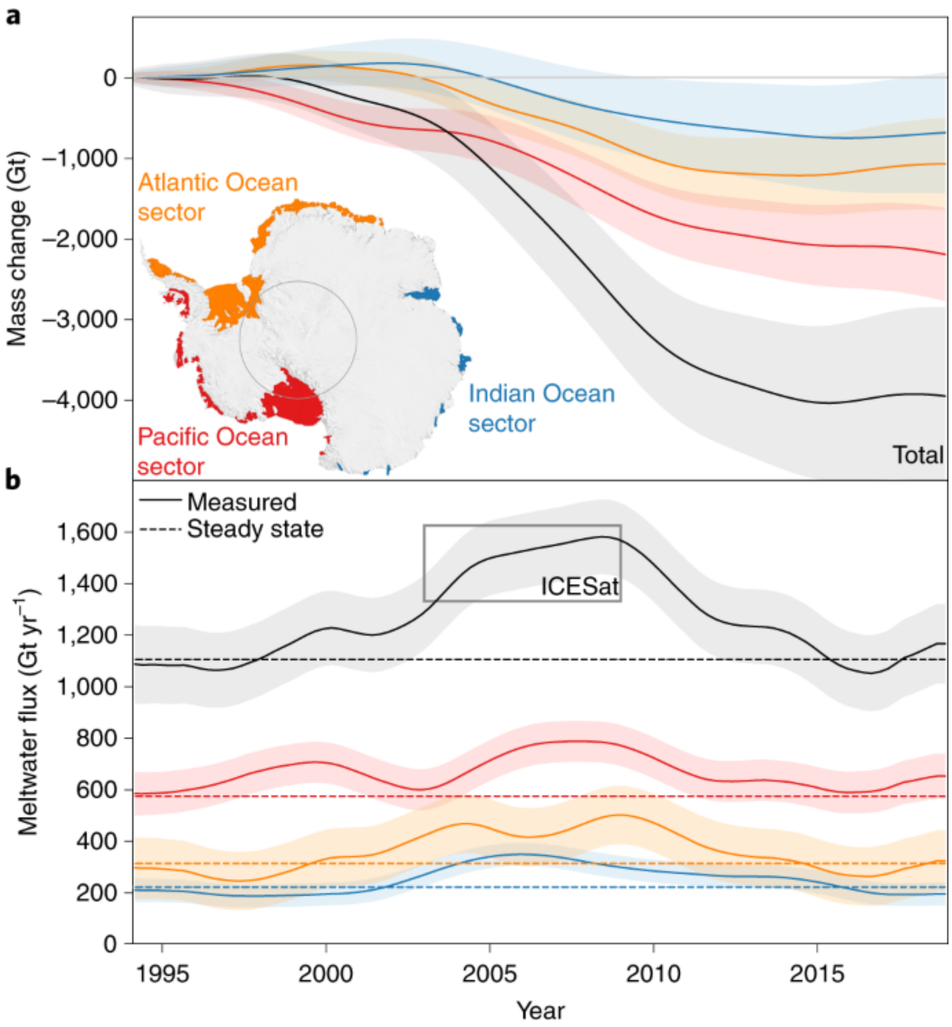

Figure 3. Cumulative ice-shelf mass change between 1994 and 2018 for the Pacific (red), Atlantic (orange), and Indian (blue) ocean sectors of Antarctica, with shading showing 95% confidence intervals. The region definitions are shown on the inset map, and the combined total for all ice shelves is shown in black. b, Meltwater fluxes for 1994–2018 from ocean-driven ice-shelf basal melting for the same regions. Dashed lines represent meltwater fluxes in steady state, where the mass of the ice shelves is constant through time. Total meltwater flux estimates for the ICESat era (grey box) are averaged between two studies (Rignot et al., 2013; Depoorter et al., 2013) (width indicates time period, height indicates 95% confidence interval).

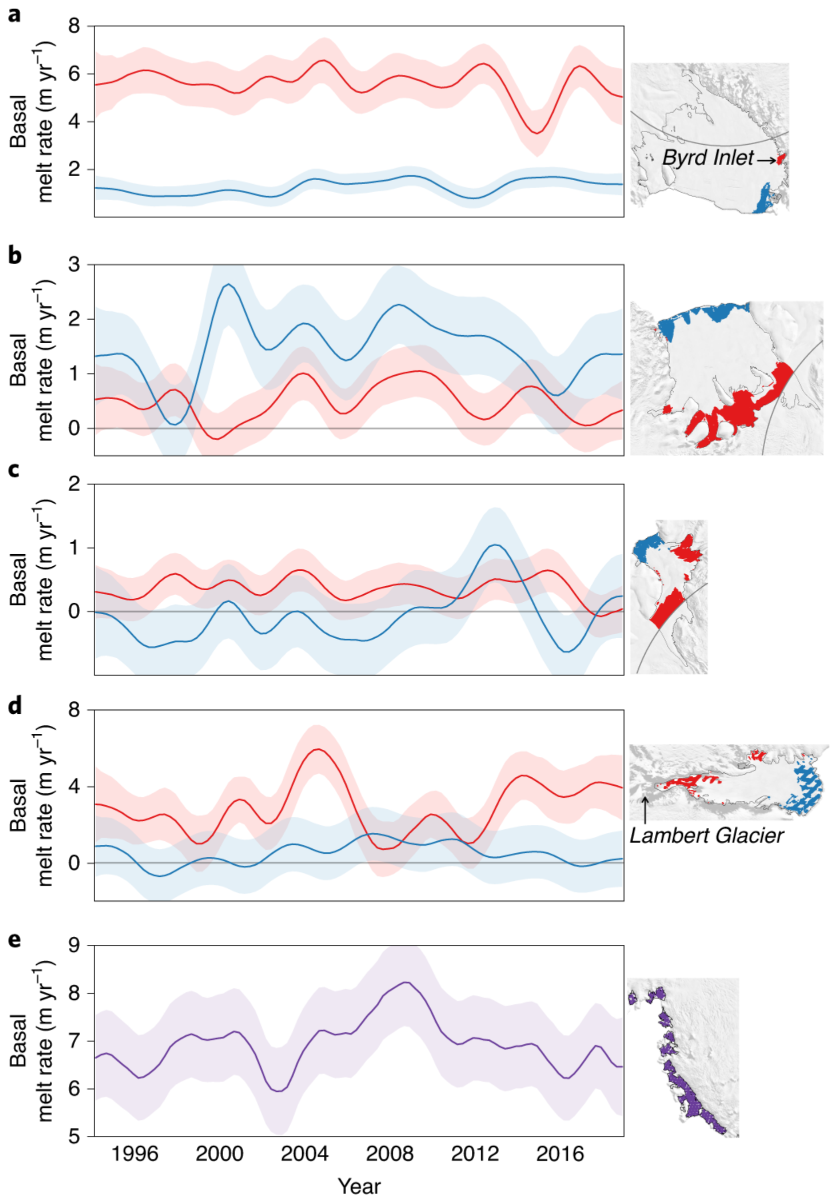

Figure 4. a–d, Area-averaged basal melt rates (in m of ice equivalent per year) for selected regions within the four largest Antarctic ice shelves. a, Ross. b, Ronne. c, Filchner. d, Amery. Regions shown in red experience melting predominantly from cold HSSW inflows at deep ice drafts (Mode 1), while regions shown in blue typically experience melting from intrusions of AASW at shallow ice drafts (Mode 3). e, Basal melt rates for Amundsen Sea ice shelves, which experience melting from inflows of warm CDW (Mode 2). Gaps in the spatial coverage reflect the sampling of the altimeters before CryoSat-2.

4.6 Methods

Melt rates from Lagrangian CryoSat-2 analysis, 2010–2018

In a Lagrangian reference frame (following a parcel of ice), and assuming that the ice shelf is floating in hydrostatic balance, the net ice shelf height change observed using satellite altimetry (Dh/Dt), where h is the ice shelf surface height relative to the height of the ocean surface h_{ocean}, is related to the surface mass balance (M_s; kg/(m^2 yr)), basal melt rate (w_b; m of ice equivalent per year), ice shelf divergence ($H_i \nabla \cdot \mathbf{v}$; in m of ice equivalent per year) and changes in firn air content (h_{air}; m) (Moholdt et al., 2014):

$$\frac{Dh}{Dt} = \frac{(\rho_w - \rho_i)}{\rho_w}\left(\frac{M_s}{\rho_i} - H_i \nabla \cdot \mathbf{v} - w_b\right) + \frac{Dh_{air}}{Dt}, \tag{S1}$$

where $\mathbf{v}$ is the two-dimensional grid of ice surface velocity vectors (m/yr), H_i is ice shelf thickness in units of m of ice equivalent, ρ_w is the density of ocean water (assumed to be 1028 kg/m^3), and ρ_i is the density of ice (assumed to be 917 kg/m^3). Here, H_i is given by $H_i = H - h_{air}$, where H is the total ice shelf thickness (surface to base). In the following four sections we describe the various datasets used in our estimation of w_b through Equation S1.

Height of the ocean surface

We estimated the height of ocean surface h_{ocean} as

$$h_{ocean} = h_{geoid} + h_{mdt} + h_{ot} + h_{ibe} + h_{lt} + h_{slr}, \tag{S2}$$

where h_{geoid} is the height of the EIGEN-6C4 geoid (Förste et al., 2014), h_{mdt} is mean dynamic topography from DTU13MDT (Andersen et al., 2016), h_{ot} is the ocean tide from the CATS2008 tide model (Howard et al., 2019) (an update to the model described by Padman et al., 2002), h_{ibe} is a correction for the inverse barometer effect due to atmospheric pressure variability and is obtained from the MOG2D Dynamic Atmosphere Correction (Carrère & Lyard, 2003), h_{lt} is the ocean load tide estimated using the TPXO7.2 model (Egbert & Erofeeva, 2002), and h_{slr} is the increase in mean sea-level around the Antarctic coast reported by Rye et al. (2014). Of the terms on the right-hand side of Equation S2, we only considered temporal variability of h_{ot}, h_{ibe}, and h_{lt}, and h_{slr}.

Lagrangian height changes

We derived Dh/Dt, following Moholdt et al. (2014), by first advecting the locations of CryoSat-2 footprints, initially at $\mathbf{x}_{t_0}$, to their 2015 locations $\mathbf{x}$ using

$$\mathbf{x} = \mathbf{x}_{t_0} + \sum_{t_0}^{2015} \mathbf{v}_{2015}\ \Delta t, \tag{S3}$$

where Δt is 0.01 years. For $\mathbf{v}_{2015}$, we used ice velocities from a 2015 mosaic derived from Landsat-8 feature tracking at 300 m posting (Gardner et al., 2018). For the ice shelves where the southern limit of these velocity data (82.4°S) did not include the entire area (Filchner, Ronne and Ross), we filled in data gaps in the 2015 mosaic using 1996-2016 mean values from Rignot et al. (2017). The velocity data were adjusted to reflect velocities in the Antarctic Polar Stereographic projection with a standard parallel of 71° and a standard longitude of 0°. We converted latitudes and longitudes of CryoSat-2 data into $\mathbf{x}$ using the same projection. Using the advected CryoSat-2 data, we estimated Dh/Dt and associated uncertainties in grid cells at 500 m spacing and 1 km resolution using the ‘plane fit’ technique described by Adusumilli et al. (2018) (their Section S1). We discarded data in a grid cell when the uncertainty in Dh/Dt estimated from the plane fit was greater than 0.5 m/yr.

Thickness change due to ice shelf divergence ($H_i \nabla \cdot \mathbf{v}$)

We estimated the $H_i \nabla \cdot \mathbf{v}$ term in Equation S1 using ice thickness (H_i) estimated from CryoSat-2 data following Adusumilli et al. (2018) but using the advected footprint locations as described above. For $\nabla \cdot \mathbf{v}$, we used strain rate estimates and associated uncertainties from Alley et al. (2018), based on velocity data collected between 2013 and 2016 north of 82.4°S. Over Filchner, Ronne and Ross ice shelves these data did not extend to their southern limits. Therefore, we used values of $\nabla \cdot \mathbf{v}$ provided by Moholdt et al. (2014) for Filchner, Ronne, and Ross ice shelves.

Surface mass balance (M_s) and height changes from firn processes (dh_{air}/dt)

For the M_s term, we used NASA’s global Modern-Era Retrospective analysis for Research and Applications, Version 2 (MERRA-2; Gelaro et al., 2017), which we combined with an offline high-resolution MERRA-2 ‘replay,’ denoted M2R12K (Smith et al., 2020), to derive a hybrid product referred to as ‘MERRA-2 Hybrid.’ M2R12K is a high-resolution MERRA-2 run (12.5 km) specifically targeted over the Antarctic and spanning 2000-2014. To maintain the fine spatial resolution of the M2R12K, it’s mean seasonal cycle is combined with the seasonal residuals from the full MERRA-2 period (1980-2019). Thus, MERRA-2 Hybrid combines the fine spatial resolution from M2R12K with the longer time record from MERRA-2. We used

MERRA-2 Hybrid forcings (precipitation minus evaporation, skin temperature, and meltwater flux from a degree-day model) for simulations of the firn column using the densification equations described in Arthern et al. (2010) implemented in the Community Firn Model (CFM; Stevens et al., 2020) to estimate dh_{air}/dt (Smith et al., 2020). We refer to this firn densification model as GSFC-FDMv0, which is calibrated with ~200 firn depth-density profiles from both the Greenland and Antarctic Ice Sheets and includes both dry and wet firn processes. We assume that $Dh_{air}/Dt = dh_{air}/dt$ because of the low spatial resolution of the firn model output compared to the distances over which the CryoSat-2 footprints were advected in the Lagrangian framework. GSFC-FDMv0 provides dh_{air}/dt values at 12.5 km spatial posting and 5-day temporal sampling (Smith et al., 2020). We interpolated these data in space to the grid cells at 500 m spacing used to derive Dh/Dt. Details regarding GSFC-FDMv0 are within the Supplementary Materials of Smith et al. (2020).

Steady-state basal melt rates

We estimated the "steady-state" basal melt rate, $w_{b,steady}$, required to keep ice shelves in steady-state mass balance (equivalent to assuming that there is no net change in H_i) using

$$w_{b,steady} = \frac{\langle M_s \rangle}{\rho_i} - \langle \nabla \cdot (H_i \, \mathbf{v}) \rangle, \tag{S4}$$

where $\langle\cdot\rangle$ represents the time-average value. There is no temporal variability in our estimates of $w_{b,steady}$: we used the 1994–2018 mean values from the MERRA-2 Hybrid (precipitation minus evaporation: P-E) for $\langle M_s \rangle$ and assumed that outside the Amundsen Sea sector there was no change in $\nabla \cdot (H_i \, \mathbf{v})$ in time during our observation period.

Depth dependent, area-integrated meltwater fluxes

We estimated the ice shelf draft, D_i, the depth of the ice shelf base below mean sea level, using $D_i = \rho_i H_i / \rho_w$. For grid cells in which we were not able to estimate H_i, we used values estimated using BedMachine (Morlighem et al., 2020) data (Figure S2e). We obtain the dependence of area-integrated meltwater fluxes on ice shelf draft D_i (Figure 2) by integrating w_b in discrete bins of D_i at 30 m spacing.

Ocean thermal forcing

We define thermal forcing, ΔT (Figure 1), as the temperature above the in situ freezing point of seawater, T_f. We obtained profiles of ocean temperature (T) and salinity (S) from the World Ocean Database 2018 (Boyer et al., 2018), then estimated the values of $T_f = f(T, P)$, where P is pressure, from the function described by McDougall et al. (2014) and implemented in the Gibbs SeaWater Oceanographic Toolbox of TEOS-10 (McDougall & Barker, 2011). We only used profiles that satisfied one of the following criteria: (i) profile extends to at least 800 m in water depth z_b deeper than 800 m; or (ii) profile extends to within 150 m of the seabed (evaluated from Rtopo2; Schaffer et al., 2016) for $z_b < 800$ m. We then determined maximum thermal forcing as the maximum value of ΔT in the depth range 200-min(z_b, 800) m. The limit of 200 m is designed to exclude summer-warmed Antarctic Surface Water and focus on deeper water masses on the continental shelf that have access to the cavities under ice shelves; i.e., primarily Mode 1 and Mode 2 melting. For $z_b < 200$ m, we take the value of ΔT at the deepest point in the profile. The values of ΔT were then interpolated to a 25-km uniform polar stereographic grid, with standard latitude and longitude of 71°S, 0°E, using a bi-cubic distance weighting scheme, modified to increase weightings along isobath and lower weightings across isobaths, consistent with known strong barotropic control of circulation over Antarctica's continental shelves and along the shelf break (Dinniman et al., 2011; Dunn & Ridgway, 2002).

Time series of height change from Eulerian ERS-1, ERS-2, Envisat, and CryoSat-2 analysis

In addition to 2010–2018 mean values of w_b from Lagrangian analysis of CryoSat-2 data, we also estimated time-varying melt rates derived using Eulerian analysis of height change derived from ERS-1, ERS-2, Envisat, and CryoSat-2 altimetry. We used consistent 10 km grid cells at 1 km posting for all missions, and data were averaged in time to three-month intervals. To merge height change data from all four missions to produce a continuous time series spanning 1992–2018, we only considered grid cells where there were sufficient data from all four missions, as described below.

We obtained ERS-1, ERS-2, and Envisat height data ($h_{ERS/Env}$) from Brockley et al. 2017) and Soussi et al. (2018). We corrected $h_{ERS/Env}$ for change in the ocean surface h_{ocean}using Equation S2. We first derived height changes for each mission separately. For each grid cell, we estimated height changes for each mission if there were at least 15 data points spanning at least 3 years using:

$$h_{ERS/Env} = h_0 + f(x,y) + m_6 t + m_7 s + m_8 b + m_9 f + h_r(t), \tag{S5}$$

where $f(x,y) = m_1 x + m_2 y + m_3 x^2 + m_4 y^2 + m_5 xy$ represents surface topography, t is time in decimal years, s is a satellite ascending/descending binary flag (0 or 1), b is backscatter, and f is a binary mode flag that is only applied to data from ERS-1 or ERS-2, based on whether the heights were from ocean-mode or ice-mode data. The parameters in Equation S5 (h_0, m_{1-10}) were estimated using a robust linear regression where outliers outside the $min(3\sigma$,10 m) range were discarded in 10 iterations. We estimated standard errors of the regression for each of the parameters in Equation S5, and discarded grid cells with an error greater than 0.3 m/yr in m_6, The residuals in the linear regression $h_r(t)$ were binned in three-month intervals and contain any temporal signal that is not included in a linear trend as well as noise.

The height-change rate (dh/dt) estimate for an ice shelf for each individual mission was then

$$\frac{dh}{dt} = m_6 + \frac{dh_r}{dt}. \tag{S6}$$

We processed CryoSat-2 data using the Eulerian ‘plane-fit’ technique described in Adusumilli et al. (2018) (their Section S1) after applying the same geophysical corrections used for ERS-1, ERS-2, and Envisat data.

To avoid biases from different spatial sampling, we discarded data from all grid cells which did not contain height change measurements from all four missions. For grid cells where sufficient data were available, we then merged the height change time series from the four radar altimeters by ensuring that height-change rate during the time periods with overlapping data was equal to the average of the height-change rates estimated from each altimeter. Therefore, we imposed $dh/dt = (dh_{ERS-1}/dt + dh_{ERS-2}/dt)/2$ during 1995–1996, $dh/dt = (dh_{ERS-2}/dt + dh_{Env}/dt)/2$ during 2002–2003, and $dh/dt = (dh_{ERS-2}/dt + dh_{Env}/dt)/2$ during 2010–2011.

Influence of surface melting on radar-derived height changes

We found large decreases in RA-derived height changes between 1992 and 1994 across Antarctica. In some previous studies (Paolo et al., 2015; Paolo et al., 2016), data from this period were excluded due to this anomalous signal. Using surface melt data from RACMO and a positive degree day model based on MERRA-2 (Smith et al., 2020), we found that this change in RA-derived height change was primarily due to a large circum-Antarctic surface melt event in December 1991. This melt event likely created a bright radar reflector, and its burial following subsequent snowfall was tracked by the radar altimeter, which caused a downward trend in estimated height. Due to the large effect of this event across several ice shelves around Antarctica, we excluded this period in our analysis.

For Ross Ice Shelf, we found large changes in height following anomalous surface melt events during the austral summers of 1991–1992, 2002–2003, and 2015–2016. Two of these (1991–1992 and 2015–2016) were the largest surface melt events over the ice shelf during the 1980–2016 MERRA-2 period (Nicolas et al., 2017). We accounted for the radar response following such events by estimating a time series of h_{air} using height changes measured over grounded ice adjacent to the floating ice shelf, following the methodology of Moholdt et al. (2014). We derived height changes over grounded ice up to 100 km from the ice shelf boundary in grid cells at 5 km spacing using the plane-fit technique described by McMillan et al. (2014). Each grid cell had at least 15 data points spanning a time interval of at least 3 years. We discarded grid cells with an uncertainty in estimated dh/dt greater than 0.3 m/yr. Since there were too few data to apply a spatially variable correction over the ice shelf, we followed Moholdt et al. (2014) to use a single time series for the entire ice shelf.

Time series of melt rates

From the merged multi-mission Eulerian height-change rate time series $dh(t)/dt$ spanning 1994–2018, we derived time series of basal melt rate anomalies ($w_{b,anom}$, relative to the 2010–2018 mean) using:

$$w_{b,anom}(t) = \frac{M_{s,anom}}{\rho_i} - \frac{\rho_w}{\rho_w - \rho_i}\left(\frac{dh_{anom}}{dt} - \frac{dh_{air,anom}}{dt}\right) - \nabla \cdot (H_i\,\mathbf{v})_{anom}, \tag{S7}$$

where $M_{s,anom}$, dh_{anom}/dt, and $dh_{air,anom}/dt$ are anomalies (relative to the 2010–2018 mean) in rates of altimeter-derived height change, firn-air content from GSFC-FDMv0, and MERRA-2 *P-E* data, respectively, smoothed to three-month time scales using a moving average filter. We only considered anomalies in $\nabla \cdot (H_i\,\mathbf{v})$ for the Amundsen Sea sector, for which we used time-variable estimates of $\mathbf{v}$ from Mouginot et al. (2014) for the 1994–2013 period and from Mouginot et al. (2017) for the 2014–2017 period. Gaps in the time series of $\nabla \cdot (H_i\,\mathbf{v})_{anom}$ were filled using linear interpolation. We produced time series of basal melt rates, $w_b(t)$, by adding high resolution melt rates from CryoSat-2 analysis to the time series of melt rate anomalies $w_{b,anom}(t)$. We assume that there was no change in w_b in regions south of 81.5°S, the orbit limit of the ERS-1, ERS-2 and Envisat satellites.

Uncertainty estimation

We compared GSFC-FDMv0 estimates of dh_{air}/dt with previously published estimates from an atmospheric model (RACMO2.3p2; Wessem et al., 2018) and the associated firn densification model (IMAU-FDM; Ligtenberg et al., 2011) between 1979 and 2016 (the time period available for RACMO and IMAU-FDM). Using this comparison, we derived an uncertainty estimate using the combination of: (a) sensitivity tests to quantify uncertainties from the assumption of steady state climate that is used to spin up a firn densification model (Pritchard et al., 2012) (Figure S7a); and (b) standard deviations of differences between GSFC-FDMv0 and IMAU-FDM estimates of dh_{air}/dt values during 1980–2016 at GSFC-FDMv0 grid cell locations (these values are shown in Figure S7b for annual time scales, but they are smaller for the longer time scales typically considered in this study). We assumed that these uncertainties were Gaussian and uncorrelated, and added them in quadrature.

We estimated uncertainties for all terms in Equation S5 as the uncertainties from the linear regression, and propagated these to $h(t)$ in Equation S6. Uncertainties in $h_r(t)$ were estimated as the standard deviation of heights from the residuals of Equation S5 within each quarterly bin. Uncertainties in $H_i \nabla \cdot \mathbf{v}$ were provided by Alley et al. (2018), uncertainties in M_s were estimated using a moving standard deviation at annual time scales, and the uncertainties in the advection of heights from Lagrangian processing were not considered; compared to previously described uncertainty sources, the three sources here represent a substantially smaller component of total uncertainty.

We propagated these uncertainties to the filtered time series of basal melt rate using a bootstrap approach. For each ice shelf (or in the case of the top four panels of Figure 4, for regions within large ice shelves), we applied a filter to the average $h(t)$ time series that included both a gradient and a smoothing operator to estimate dh/dt. The residuals from the filtered time series were resampled 100 times, and each sample was combined with Gaussian random noise from the error sources described previously. These samples were added back to dh/dt and integrated to produce 100 resampled time series $h_{samp}(t)$, which were used to produce 100 time series of dh_{samp}/dt. The standard deviation of dh_{samp}/dt provided the final uncertainty in

dh/dt. We estimated uncertainties in melt rates in the eight sectors around Antarctica by summing the uncertainties from all ice shelves in each sector in quadrature (Table 1).

Estimates of marine ice thickness

We estimated thickness of marine ice (H_{ma}) under Ronne and Amery ice shelves from our steady-state basal melt rate estimates, $w_{b,steady}$ (Joughin & Vaughan, 2004):

$$\frac{dH_{ma}}{ds} = \frac{w_{b,steady} - H_{ma}\nabla\cdot\mathbf{v}}{|\mathbf{v}|}, \tag{S8}$$

where $H_{ma} \geq 0$ and s represents the distance along a flowline. Here, we use $w_{b,steady}$ instead of the time-stamped estimate (w_b) because the value of H_{ma} is a function of the accumulation and strain rates of an ice shelf at decadal to centennial time scales. We generated flowlines for Ronne and Amery ice shelves, and solved Equation S8 using $\Delta s = |\mathbf{v}|\,\Delta t$ with $\Delta t = 1$ year, assuming $H_{ma} = 0$ at the beginning of the flowline. Our estimated values of H_{ma} for both ice shelves show good agreement with independent estimates derived by differencing thicknesses derived from satellite altimetry and from radar sounding (Fricker et al., 2001; Lambrecht et al., 2007) (Figure S3).

Changes in iceberg calving rates

We have so far only considered temporal variability in ice-shelf mass and meltwater flux due to changes in ice-shelf basal melt rates relative to steady-state values. However, ice-shelf hydrofracture in the Antarctic Peninsula (Cook and Vaughan, 2010) and excess iceberg calving rates due to long-term dynamic thinning of Amundsen Sea (MacGregor et al., 2012) have also contributed to net ice-shelf mass loss and increases in meltwater export to the upper ocean in recent decades. We estimated net mass loss due to changes in ice shelf extent from ice shelf thickness estimates generated using elevations from the ERS-1 geodetic phase (1994–1995) for regions where ice shelf areas decreased; these were excluded from previous thickness estimates (Griggs & Bamber, 2011). We estimate a net mass loss of 1650±200 Gt from Antarctic Peninsula ice shelves during our record (Figure S7) due to the hydrofracture-induced collapse of Larsen A, Larsen B, and sections of Wilkins ice shelves (Scambos et al., 2004; Scambos et al., 2009). In addition, net retreat of Thwaites, Pine Island and Getz ice shelves in the Amundsen Sea contributed to a combined net mass loss of 1,230 ± 70 Gt. The combined mass loss from excess calving of Antarctic Peninsula and Amundsen Sea sector ice shelves was 2,880 ± 210 Gt, which is comparable to our circum-Antarctic mass loss estimate of 3,960 ± 1,100 Gt from thinning ice shelves (Figure 3a).

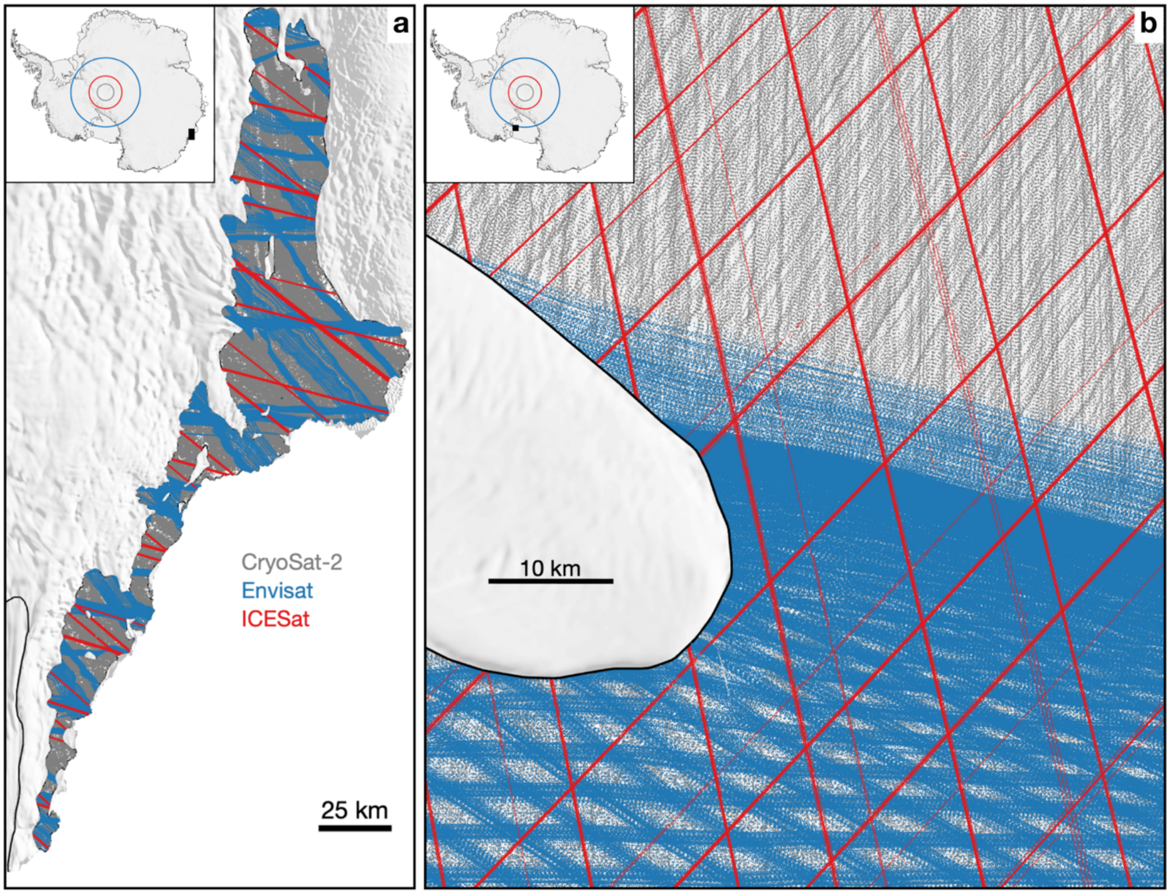

Figure S1: Spatial sampling of satellite laser and radar altimeters. Spatial sampling of heights measured using CryoSat-2 (2010–present), Envisat (2002–2012), and ICESat (2003–2009) altimetry over (a) Totten Ice Shelf, East Antarctica, and (b) Ross Ice Shelf. The southern orbit limit of Envisat is visible in (b), and the orbit limits for the three altimeters are shown in the inset figures, with locations of each site shown by the black box. Some Envisat tracks sampled areas slightly south of its nominal orbit limit (81.5°S) during Phase 3 from 2010 until the end of its mission in 2012.

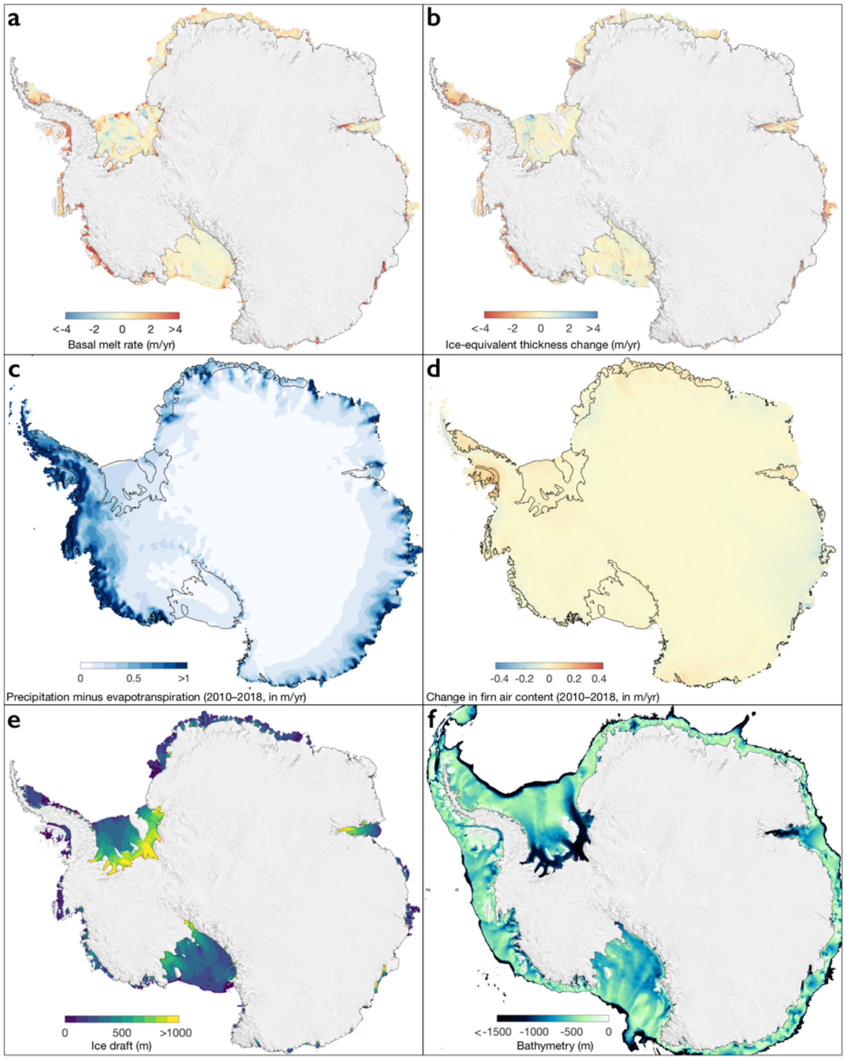

Figure S2: Key ice observations across Antarctic ice shelves. Panels (a–e) are for the CryoSat-2 (2010–2018) period. (a) High resolution ice shelf basal melt rates in m of ice equivalent per year (same values as Figure 1, with a different color scale); (b) ice-equivalent thickness change in m of ice equivalent per year; (c) precipitation minus evapotranspiration in m of ice equivalent per year; (d) change in firn air content in m of air per year; (e) ice draft from CryoSat-2 with data gaps filled in using BedMachine (Morlighem et al., 2020); and (f) bathymetry around Antarctica from BedMachine. Color range for (d) is scaled to be consistent with the scale for (a,b) after hydrostatic adjustment (red values indicate a positive change in firn air content).

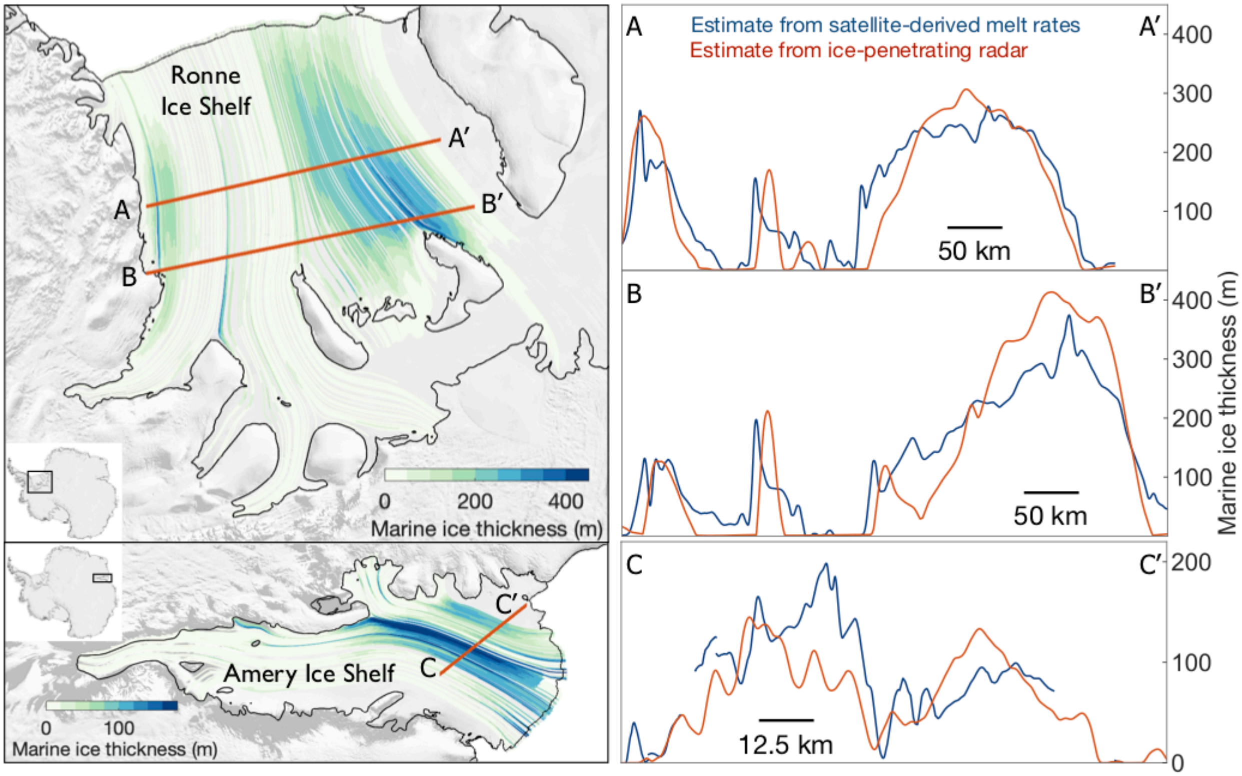

Figure S3: Estimates of marine-ice thickness. Marine-ice thickness under Ronne and Amery ice shelves estimated using satellite-derived steady-state basal melt rates (left) using the methodology of Joughin and Vaughan, (2004) described in Methods. We used bicubic interpolation to extract values along three profiles (A-A’, B-B’, C-C’) to compare them against independent estimates from airborne radar sounding (Fricker et al., 2001; Lambrecht et al., 2007).

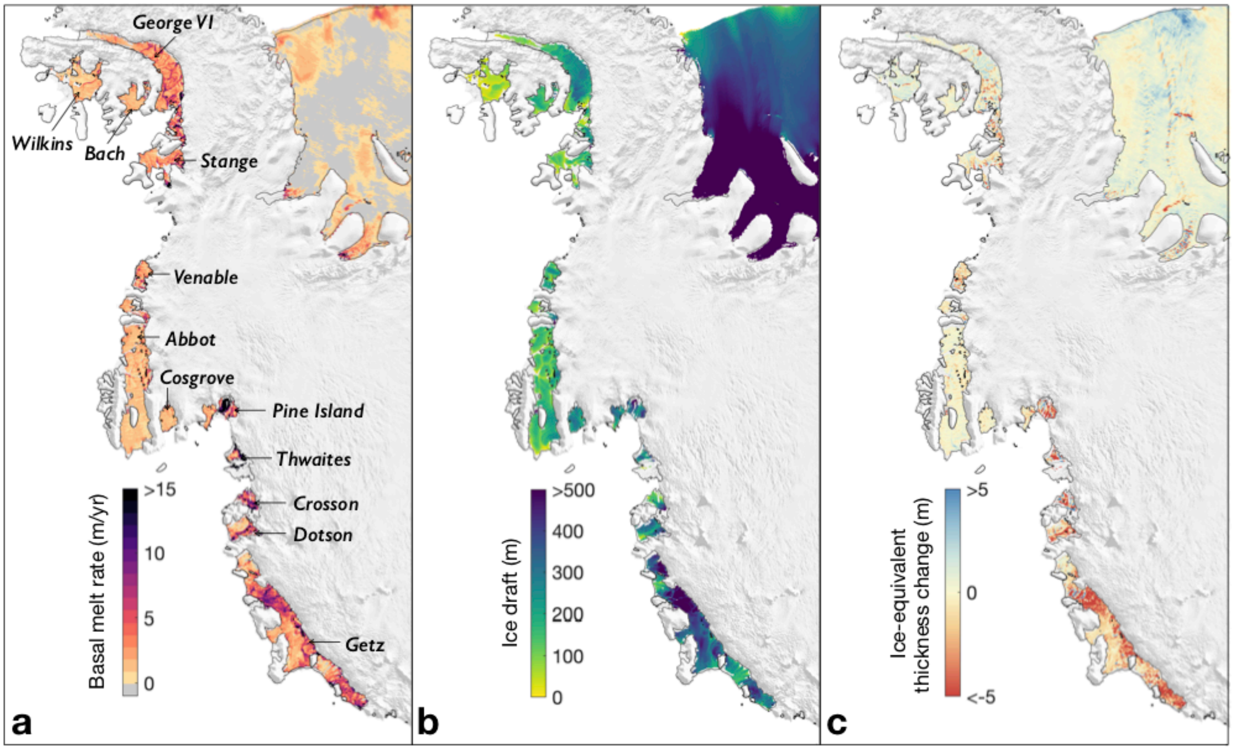

Figure S4. Key ice observations of Amundsen and Bellingshausen Sea ice shelves. Amundsen Sea and Bellingshausen Sea ice shelf (a) basal melt rates in m of ice equivalent per year, (b) ice draft, and (c) thickness change in m of ice equivalent per year for the CryoSat-2 period (2010–2018). Individual ice shelves are identified on panel (a).

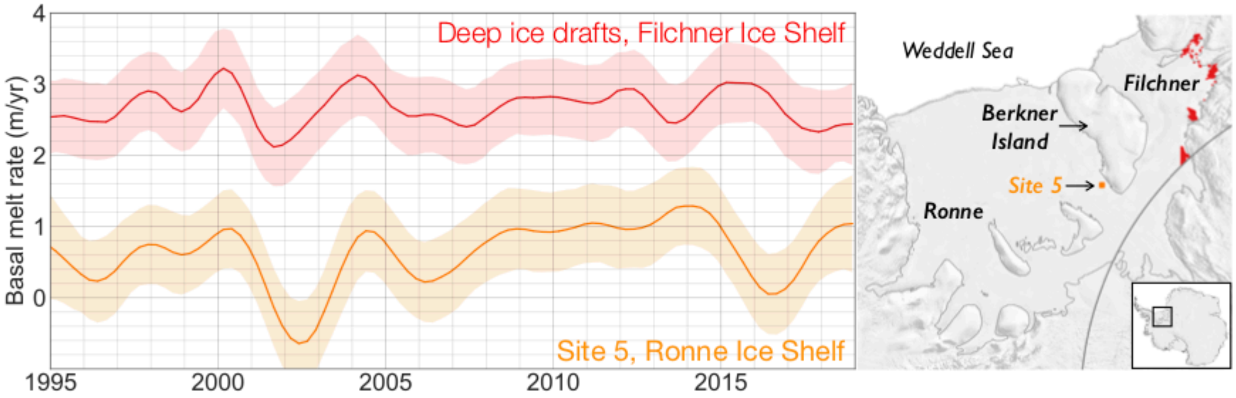

Figure S5. Basal melt rates at Site 5, Ronne Ice Shelf. Basal melt rates at deep ice drafts for Filchner Ice Shelf and at observation Site 5 near the southwestern Berkner Island coast of Ronne Ice Shelf. Temporal variations of basal melting in both regions are influenced by processes in the Weddell Sea north of the ice shelves, but are not directly linked (Nicholls et al., 2003). Time series are smoothed with a low-pass filter with a three-year cutoff.

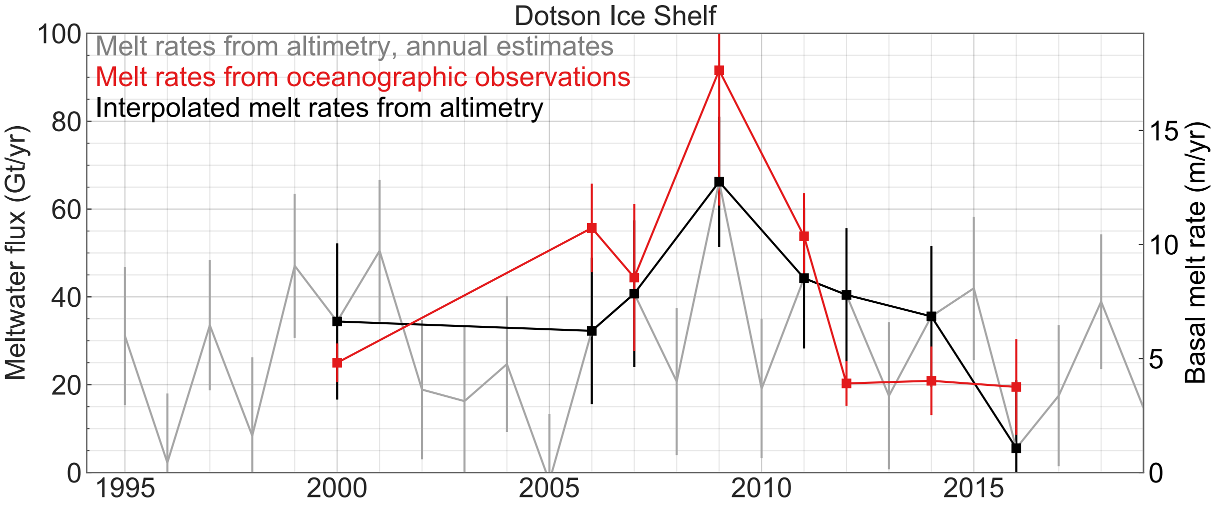

Figure S6. Basal melt rates for Dotson Ice Shelf. Satellite-derived annual basal melt rates (in gray) for Dotson Ice Shelf (see Figure S4a for location) from this study compared to estimates from eight oceanographic sections near the ice front (in red) (Jenkins et al., 2018). To aid visual comparison, we interpolated (in black) the raw time series to the timestamps of the oceanographic measurements.

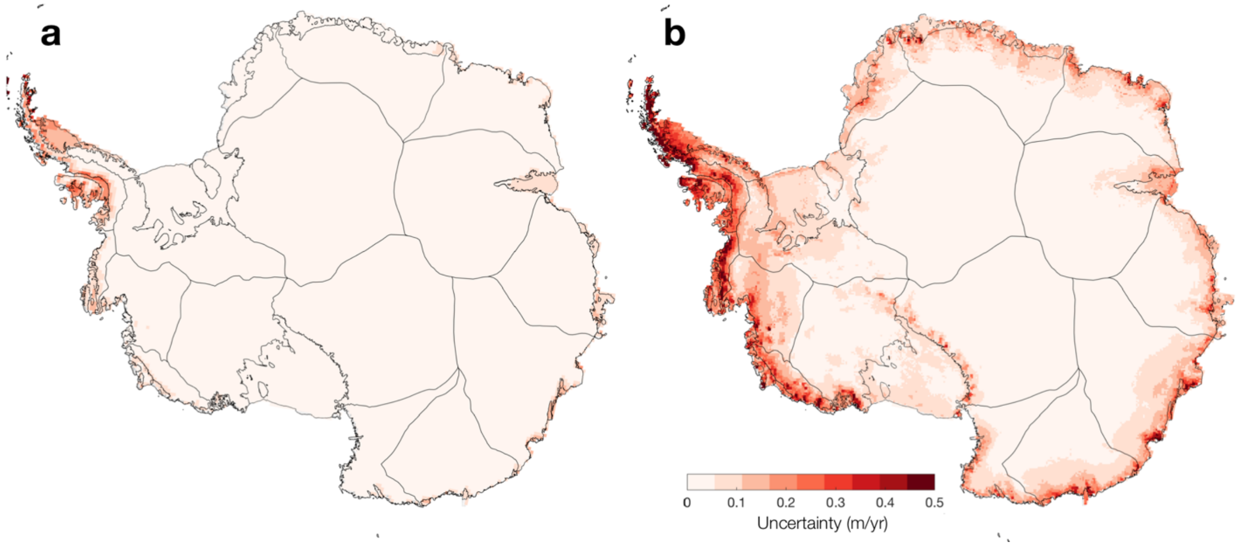

Figure S7. Uncertainties in changes in firn air content. Uncertainties in changes in firn air content in m of firn air per year at annual time scales. (a) Uncertainty from steady-state assumption in climate for firn model spin-up (Pritchard et al., 2012). (b) Uncertainty arising from resolution and errors in model physics, estimated as the differences between the outputs from the GSFC-FDMv0 (forced by the MERRA-2 atmospheric model with mean climate from the M2R12K replay) and the IMAU firn densification model forced by the RACMO2.3p2 regional atmospheric model (Ligtenberg et al., 2011). These uncertainties represent an upper bound and are lower at the longer time scales typically considered in this study.

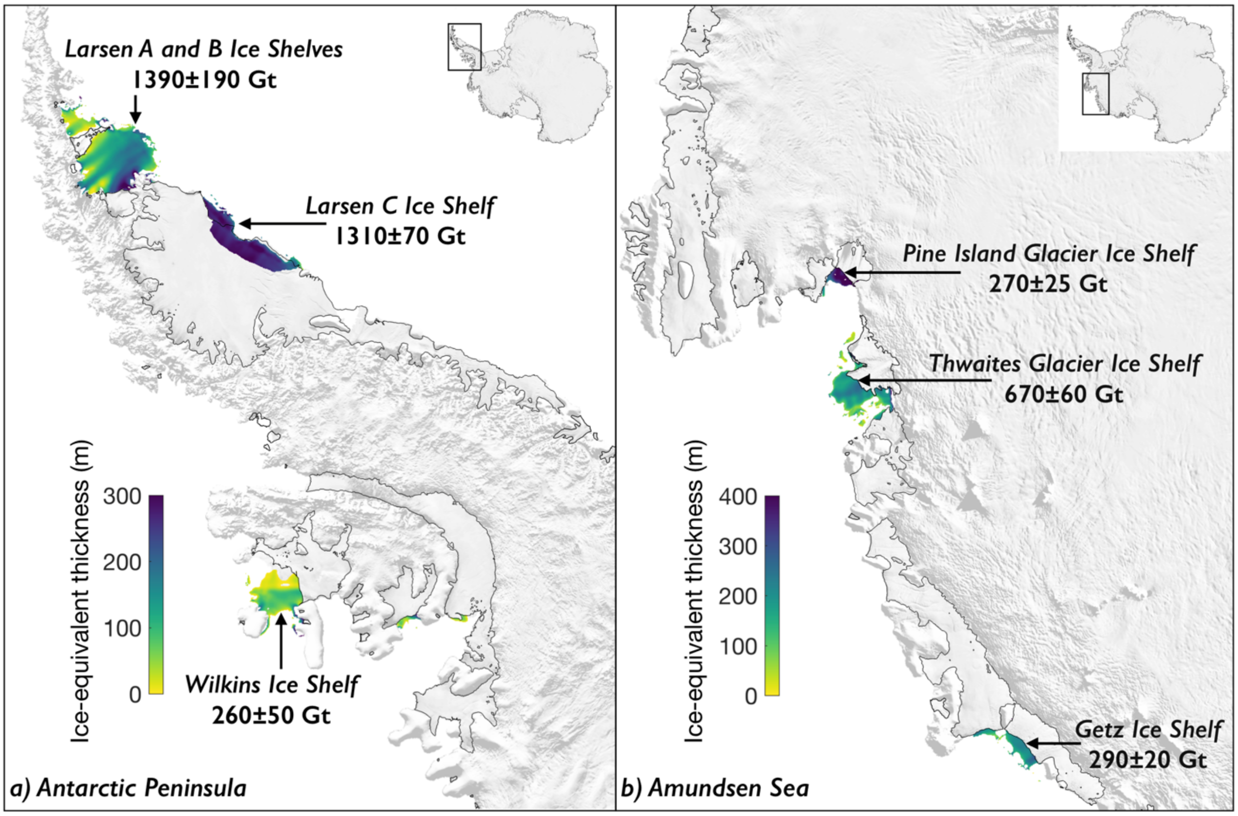

Figure S8. Changes in extent of Antarctic Peninsula and Amundsen Sea sector ice shelves. 1994–2018. Ice-equivalent thickness data from the ERS-1 geodetic phase (1994/1995) are shown for regions that were covered by open ocean or sea ice at any time during the CryoSat-2 period. We only show regions with heights above mean sea level greater than 10 m (Figure 1).

Table 1. Basal melt rates (in m/yr) and meltwater fluxes (in Gt/yr) of ice shelves surveyed in this study. Steady-state mass fluxes can be estimated as the difference between the mean mass flux between 1994 and 2018 and the excess mass flux during the same period. Uncertainties are 95% confidence intervals.

Ice Shelf	Area (km^2)	Latitude	Longitude	Basal melt rate, 1994–2018 (m/yr)	Meltwater flux, 1994–2018 (Gt/yr)	Excess meltwater flux, 1994–2018 (Gt/yr)	Meltwater flux, 2010–2018 (Gt/yr)
George VI	22755	-72.39	-70.24	4.3 ± 2.2	88.8 ± 45.7	16.4 ± 45.7	82.4 ± 45.7
Bach	4444	-72.05	-71.82	3.2 ± 2.1	13.1 ± 8.5	3.2 ± 8.5	11.8 ± 8.5
Wilkins	10390	-70.40	-71.73	2.7 ± 3.4	26.1 ± 32.0	2.5 ± 32.0	23.2 ± 32.0
Stange	7397	-73.29	-76.64	3.7 ± 2.1	25.4 ± 14.2	7.2 ± 14.2	25.9 ± 14.2
Venable	3037	-73.11	-87.33	5.1 ± 2.0	14.3 ± 5.5	7.6 ± 5.6	10.3 ± 5.5
Abbot	27461	-72.94	-94.78	1.5 ± 1.5	37.1 ± 38.1	8.5 ± 38.1	37.9 ± 38.2
Bellingshausen	**75484**	**–**	**–**	**3.0 ± 1.0**	**204.8 ± 69.7**	**45.3 ± 69.7**	**191.4 ± 69.7**
Cosgrove	2964	-73.56	-100.33	1.0 ± 1.5	2.7 ± 4.1	0.0 ± 4.1	4.2 ± 4.1
Pine Island	5950	-74.83	-100.79	14.0 ± 1.6	76.6 ± 8.6	15.8 ± 8.6	76.0 ± 8.7
Thwaites	3352	-75.08	-106.16	26.7 ± 2.4	81.9 ± 7.4	11.6 ± 7.4	81.1 ± 7.4
Crosson	2932	-75.03	-110.51	7.8 ± 1.8	20.9 ± 4.9	10.8 ± 4.9	17.9 ± 4.9
Dotson	5657	-74.70	-112.92	5.4 ± 1.6	28.2 ± 8.5	13.6 ± 8.5	26.1 ± 8.5
Getz	32114	-74.46	-124.49	4.2 ± 1.4	124.1 ± 40.9	61.4 ± 40.9	122.6 ± 40.9
Amundsen	**52969**	**–**	**–**	**6.9 ± 0.9**	**334.5 ± 43.7**	**113.2 ± 43.7**	**327.9 ± 43.8**
Land	587	-75.58	-141.43	20.4 ± 2.7	11.0 ± 1.5	2.3 ± 1.5	10.9 ± 1.5
Nickerson	6001	-75.81	-145.84	1.2 ± 1.4	6.5 ± 7.9	-0.1 ± 7.9	8.0 ± 7.9
Sulzberger	11229	-77.08	-148.58	1.5 ± 1.3	15.7 ± 13.3	1.6 ± 13.3	18.5 ± 13.3
Withrow	341	-77.15	-157.17	3.3 ± 1.8	1.0 ± 0.6	0.0 ± 0.6	0.9 ± 0.6
Ross West	198293	-80.37	-160.13	0.3 ± 0.4	45.8 ± 68.3	-32.4 ± 68.3	26.6 ± 69.2
Ross East	135261	-80.70	168.59	0.3 ± 0.4	34.3 ± 45.2	-40.2 ± 45.2	31.0 ± 45.3
Drygalski	2168	-75.38	163.16	1.9 ± 0.9	3.8 ± 1.7	0.5 ± 1.7	3.8 ± 1.7
Nansen	1835	-74.86	163.15	1.6 ± 1.1	2.8 ± 1.8	-0.3 ± 1.8	2.2 ± 1.8
Mariner	2354	-73.32	168.09	1.1 ± 1.7	2.3 ± 3.6	-0.3 ± 3.6	2.4 ± 3.6
Ross	**358068**	**–**	**–**	**0.4 ± 0.3**	**123.3 ± 83.5**	**-68.7 ± 83.5**	**104.3 ± 84.2**
Moscow University	4145	-66.88	121.07	7.4 ± 2.1	28.3 ± 8.0	3.8 ± 8.0	25.8 ± 8.0
Rennick	3123	-70.61	161.69	1.9 ± 1.4	5.5 ± 3.9	1.3 ± 3.9	5.7 ± 3.9
Cook	3408	-68.54	152.78	1.3 ± 1.6	3.9 ± 5.1	-1.0 ± 5.1	4.6 ± 5.1
Mertz	3243	-67.30	145.19	5.0 ± 2.4	14.8 ± 7.1	1.2 ± 7.1	13.8 ± 7.1
Holmes	1717	-66.76	127.26	13.3 ± 2.9	20.9 ± 4.5	0.6 ± 4.5	17.7 ± 4.5
Totten	6078	-67.05	116.12	11.5 ± 2.0	64.0 ± 11.0	8.4 ± 11.0	59.4 ± 11.0
Shackleton	26182	-66.06	97.90	1.8 ± 1.9	44.0 ± 44.8	12.8 ± 44.8	40.7 ± 44.8
West	15306	-66.96	85.00	1.4 ± 1.8	20.1 ± 25.1	2.9 ± 25.1	15.7 ± 25.1
Wilkes	**63202**	**–**	**–**	**3.5 ± 0.9**	**201.4 ± 54.1**	**30.0 ± 54.1**	**183.5 ± 54.1**
Amery	**60228**	**–**	**–**	**0.8 ± 0.7**	**45.6 ± 40.0**	**-2.5 ± 40.0**	**48.9 ± 39.9**
Prince Harald	4067	-69.24	35.25	2.3 ± 1.9	8.6 ± 7.2	0.1 ± 7.2	7.4 ± 7.1
Brunt_Stancomb	34573	-75.10	-22.51	0.6 ± 0.8	18.0 ± 24.6	0.2 ± 24.6	17.3 ± 24.7
Riiser-Larsen	42644	-72.91	-15.31	0.5 ± 0.8	19.4 ± 30.0	3.2 ± 30.0	16.2 ± 30.0
Quar	2076	-71.20	-10.86	0.4 ± 0.8	0.7 ± 1.6	0.2 ± 1.6	0.9 ± 1.6
Ekstrom	6754	-71.05	-8.55	1.0 ± 1.2	6.4 ± 7.2	1.0 ± 7.2	6.4 ± 7.2
Baudouin	32789	-69.96	28.47	1.0 ± 1.0	28.8 ± 29.1	0.8 ± 29.1	34.5 ± 29.1
Borchgrevink	21368	-70.32	20.38	0.8 ± 1.0	15.5 ± 20.3	3.0 ± 20.3	14.4 ± 20.3
Lazarev	8456	-69.92	14.45	0.8 ± 0.8	6.3 ± 6.2	1.9 ± 6.2	7.4 ± 6.3
Fimbul	40600	-70.57	1.55	1.0 ± 0.8	36.2 ± 29.0	-0.5 ± 29.0	32.7 ± 29.1
Nivl	7275	-70.25	11.29	1.1 ± 1.1	7.0 ± 7.2	0.6 ± 7.2	7.4 ± 7.2
Vigrid	2071	-70.23	8.33	1.2 ± 1.0	2.3 ± 1.8	0.2 ± 1.8	2.3 ± 1.9
Atka	1780	-70.61	-6.84	1.0 ± 1.2	1.6 ± 1.9	0.3 ± 1.9	1.5 ± 1.9
Jelbart	10756	-70.97	-4.33	1.0 ± 1.1	9.9 ± 11.3	1.6 ± 11.3	9.9 ± 11.3
Queen Maud	**215208**	**–**	**–**	**0.8 ± 0.3**	**160.7 ± 62.8**	**12.6 ± 62.8**	**158.4 ± 62.8**
Ronne	311968	-78.96	-65.57	0.2 ± 0.4	47.2 ± 119.3	10.5 ± 119.3	21.2 ± 119.9
Filchner	83304	-80.56	-41.02	0.4 ± 0.4	34.2 ± 29.6	-1.3 ± 29.6	33.5 ± 29.6
Filchner-Ronne	**395271**	**–**	**–**	**0.2 ± 0.3**	**81.4 ± 122.9**	**9.2 ± 122.9**	**54.8 ± 123.5**
Larsen D	18282	-70.72	-61.64	1.8 ± 1.9	30.8 ± 31.3	3.9 ± 31.3	35.3 ± 31.8
Larsen C	42384	-67.33	-63.44	2.0 ± 2.5	77.9 ± 98.7	15.9 ± 98.7	64.6 ± 98.8
Larsen B	1985	-65.87	-61.82	2.2 ± 2.3	3.9 ± 4.2	1.6 ± 4.2	3.9 ± 4.2
Larsen	**75800**	**–**	**–**	**1.6 ± 1.5**	**112.7 ± 103.6**	**21.4 ± 103.6**	**103.8 ± 103.8**
All ice shelves	**1296230**	**–**	**–**	**1.1 ± 0.1**	**1264.3 ± 147.4**	**160.5 ± 147.4**	**1173.1 ± 148.5**

Chapter 4, in full, is a reprint of the material as it appears in the journal Nature Geoscience. Adusumilli, S., Fricker, H. A., Medley, B., Padman, L., & Siegfried, M. R. (2020). Interannual variations in meltwater input to the Southern Ocean from Antarctic ice shelves. *Nature Geoscience*, 13(9), 616-620. The dissertation author was the primary investigator and author of this paper.

4.7 References

Adusumilli, S., Fricker, H. A., Siegfried, M. R., Padman, L., Paolo, F. S., & Ligtenberg, S. R. M. (2018). Variable Basal Melt Rates of Antarctic Peninsula Ice Shelves, 1994–2016. Geophysical Research Letters, 45(9), 4086–4095.

Alley, K. E., Scambos, T. A., Anderson, R. S., Rajaram, H., Pope, A., & Haran, T. M. (2018). Continent-wide estimates of Antarctic strain rates from Landsat 8-derived velocity grids. Journal of Glaciology, 64(244), 321–332.

Andersen, O., Knudsen, P., & Stenseng, L. (2016). The DTU13 MSS (Mean Sea Surface) and MDT (Mean Dynamic Topography) from 20 Years of Satellite Altimetry. In S. Jin & R. Barzaghi (Eds.), IGFS 2014 (pp. 111–121). Springer International Publishing.

Arthern, R. J., Vaughan, D. G., Rankin, A. M., Mulvaney, R., & Thomas, E. R. (2010). In situ measurements of Antarctic snow compaction compared with predictions of models. Journal of Geophysical Research: Earth Surface, 115(F3).

Boyer, Tim P.; Antonov, John I.; Baranova, Olga K.; Coleman, Carla; Garcia, Hernan E.; Grodsky, Alexandra; Johnson, Daphne R.; Locarnini, Ricardo A.; Mishonov, Alexey V.; O'Brien, Todd D.; Paver, Christopher R.; Reagan, James R.; Seidov, Dan; Smolyar, Igor V.; Zweng, Melissa M. (2018). NCEI Standard Product: World Ocean Database (WOD).

Brockley, D. J., Baker, S., Féménias, P., Martínez, B., Massmann, F., Otten, M., Paul, F., Picard, B., Prandi, P., Roca, M., Rudenko, S., Scharroo, R., & Visser, P. (2017). REAPER: Reprocessing 12 Years of ERS-1 and ERS-2 Altimeters and Microwave Radiometer Data. IEEE Transactions on Geoscience and Remote Sensing, 55(10), 5506–5514.

Budillon, G., Castagno, P., Aliani, S., Spezie, G., & Padman, L. (2011). Thermohaline variability and Antarctic bottom water formation at the Ross Sea shelf break. Deep Sea Research Part I: Oceanographic Research Papers, 58(10), 1002–1018.

Carrère, L., & Lyard, F. (2003). Modeling the barotropic response of the global ocean to atmospheric wind and pressure forcing—Comparisons with observations. Geophysical Research Letters, 30(6).

Castagno, P., Capozzi, V., DiTullio, G. R., Falco, P., Fusco, G., Rintoul, S. R., Spezie, G., & Budillon, G. (2019). Rebound of shelf water salinity in the Ross Sea. Nature Communications, 10(1), 5441.

Cook, A. J., & Vaughan, D. G. (2010). Overview of areal changes of the ice shelves on the Antarctic Peninsula over the past 50 years. The Cryosphere, 22.

Depoorter, M. A., Bamber, J. L., Griggs, J. A., Lenaerts, J. T. M., Ligtenberg, S. R. M., van den Broeke, M. R., & Moholdt, G. (2013). Calving fluxes and basal melt rates of Antarctic ice shelves. Nature, 502(7469), 89–92.

Dinniman, M. S., Klinck, J. M., & Smith, W. O. (2011). A model study of Circumpolar Deep Water on the West Antarctic Peninsula and Ross Sea continental shelves. Deep Sea Research Part II: Topical Studies in Oceanography, 58(13), 1508–1523.

Dunn, J. R., & Ridgway, K. R. (2002). Mapping ocean properties in regions of complex topography. Deep Sea Research Part I: Oceanographic Research Papers, 49(3), 591–604.

Dutrieux, P., Vaughan, D. G., Corr, H. F. J., Jenkins, A., Holland, P. R., Joughin, I., & Fleming, A. H. (2013). Pine Island glacier ice shelf melt distributed at kilometre scales. The Cryosphere, 7(5), 1543–1555.

Dutrieux, Pierre, Rydt, J. D., Jenkins, A., Holland, P. R., Ha, H. K., Lee, S. H., Steig, E. J., Ding, Q., Abrahamsen, E. P., & Schröder, M. (2014). Strong Sensitivity of Pine Island Ice-Shelf Melting to Climatic Variability. Science, 343(6167), 174–178.

Egbert, G. D., & Erofeeva, S. Y. (2002). Efficient Inverse Modeling of Barotropic Ocean Tides. Journal of Atmospheric and Oceanic Technology, 19(2), 183–204.

Eyring, V., Bony, S., Meehl, G. A., Senior, C. A., Stevens, B., Stouffer, R. J., & Taylor, K. E. (2016). Overview of the Coupled Model Intercomparison Project Phase 6 (CMIP6) experimental design and organization. Geoscientific Model Development, 9(5), 1937–1958.

Fogwill, C. J., Phipps, S. J., Turney, C. S. M., & Golledge, N. R. (2015). Sensitivity of the Southern Ocean to enhanced regional Antarctic ice sheet meltwater input. Earth’s Future, 3(10), 317–329.

Foldvik, A. (2004). Ice shelf water overflow and bottom water formation in the southern Weddell Sea. Journal of Geophysical Research, 109(C2).

Förste, C., Bruinsma, S., Abrikosov, O., Flechtner, F., Marty, J.-C., Lemoine, J.-M., Dahle, C., Neumayer, H., Barthelmes, F., König, R., & others. (2014). EIGEN-6C4-The latest combined global gravity field model including GOCE data up to degree and order 1949 of GFZ Potsdam and GRGS Toulouse. EGU General Assembly Conference Abstracts, 16.

Fricker, H. A., Popov, S., Allison, I., & Young, N. (2001). Distribution of marine ice beneath the Amery Ice Shelf. Geophysical Research Letters, 28(11), 2241–2244.

Fürst, J. J., Durand, G., Gillet-Chaulet, F., Tavard, L., Rankl, M., Braun, M., & Gagliardini, O. (2016). The safety band of Antarctic ice shelves. Nature Climate Change, 6(5), 479–482.

Gardner, A. S., Moholdt, G., Scambos, T., Fahnstock, M., Ligtenberg, S., Broeke, M. van den, & Nilsson, J. (2018). Increased West Antarctic and unchanged East Antarctic ice discharge over the last 7 years. The Cryosphere, 12(2), 521–547.

Gelaro, R., McCarty, W., Suárez, M. J., Todling, R., Molod, A., Takacs, L., Randles, C. A., Darmenov, A., Bosilovich, M. G., Reichle, R., Wargan, K., Coy, L., Cullather, R., Draper, C., Akella, S., Buchard, V., Conaty, A., da Silva, A. M., Gu, W., Zhao, B. (2017). The Modern-Era Retrospective Analysis for Research and Applications, Version 2 (MERRA-2). Journal of Climate, 30(14), 5419–5454.

Goldberg, D. N., Gourmelen, N., Kimura, S., Millan, R., & Snow, K. (2019). How Accurately Should We Model Ice Shelf Melt Rates? Geophysical Research Letters, 46(1), 189–199.

Golledge, N. R., Keller, E. D., Gomez, N., Naughten, K. A., Bernales, J., Trusel, L. D., & Edwards, T. L. (2019). Global environmental consequences of twenty-first-century ice-sheet melt. Nature, 566(7742), 65–72.

Gourmelen, N., Goldberg, D. N., Snow, K., Henley, S. F., Bingham, R. G., Kimura, S., Hogg, A. E., Shepherd, A., Mouginot, J., Lenaerts, J. T. M., Ligtenberg, S. R. M., & Berg, W. J. van de. (2017). Channelized Melting Drives Thinning Under a Rapidly Melting Antarctic Ice Shelf. Geophysical Research Letters, 44(19), 9796–9804.

Griggs, J. A., & Bamber, J. L. (2011). Antarctic ice-shelf thickness from satellite radar altimetry. Journal of Glaciology, 57(203), 485–498.

Herraiz-Borreguero, L., Lannuzel, D., Merwe, P. van der, Treverrow, A., & Pedro, J. B. (2016). Large flux of iron from the Amery Ice Shelf marine ice to Prydz Bay, East Antarctica. Journal of Geophysical Research: Oceans, 121(8), 6009–6020.

Holland, P. R., Bracegirdle, T. J., Dutrieux, P., Jenkins, A., & Steig, E. J. (2019). West Antarctic ice loss influenced by internal climate variability and anthropogenic forcing. Nature Geoscience, 12(9), 718–724.

Holland, P. R., Feltham, D. L., & Jenkins, A. (2007). Ice Shelf Water plume flow beneath Filchner-Ronne Ice Shelf, Antarctica. Journal of Geophysical Research: Oceans, 112(C5).

Howard, S. L., Padman, L., & Erofeeva, S. Y. (2019). CATS2008: Circum-Antarctic Tidal Simulation version 2008 [Data set]. U.S. Antarctic Program (USAP) Data Center.

Jacobs, S. S., Helmer, H. H., Doake, C. S. M., Jenkins, A., & Frolich, R. M. (1992). Melting of ice shelves and the mass balance of Antarctica. Journal of Glaciology, 38(130), 375–387.

Jenkins, A., Shoosmith, D., Dutrieux, P., Jacobs, S., Kim, T. W., Lee, S. H., Ha, H. K., & Stammerjohn, S. (2018). West Antarctic Ice Sheet retreat in the Amundsen Sea driven by decadal oceanic variability. Nature Geoscience, 11(10), 733–738.

Joughin, I., & Vaughan, D. G. (2004). Marine ice beneath the Filchner–Ronne Ice Shelf, Antarctica: A comparison of estimated thickness distributions. Annals of Glaciology, 39, 511–517.

Jourdain, N. C., Asay-Davis, X., Hattermann, T., Straneo, F., Seroussi, H., Little, C. M., & Nowicki, S. (2019). A protocol for calculating basal melt rates in the ISMIP6 Antarctic ice sheet projections. The Cryosphere Discuss., 2019, 1–33.

Kimura, S., Jenkins, A., Regan, H., Holland, P. R., Assmann, K. M., Whitt, D. B., Wessem, M. V., Berg, W. J. van de, Reijmer, C. H., & Dutrieux, P. (2017). Oceanographic Controls on the Variability of Ice-Shelf Basal Melting and Circulation of Glacial Meltwater in the Amundsen Sea Embayment, Antarctica. Journal of Geophysical Research: Oceans, 122(12), 10131–10155.

Lambrecht, A., Sandhäger, H., Vaughan, D. G., & Mayer, C. (2007). New ice thickness maps of Filchner–Ronne Ice Shelf, Antarctica, with specific focus on grounding lines and marine ice. Antarctic Science, 19(4), 521–532.

Lane-Serff, G. F. (1995). On meltwater under ice shelves. Journal of Geophysical Research: Oceans, 100(C4), 6961–6965.

Lewis, E. L., & Perkin, R. G. (1986). Ice pumps and their rates. Journal of Geophysical Research: Oceans, 91(C10), 11756–11762.

Ligtenberg, S. R. M., Helsen, M. M., & Broeke, M. R. van den. (2011). An improved semi-empirical model for the densification of Antarctic firn. The Cryosphere, 5(4), 809–819.

MacGregor, J. A., Catania, G. A., Markowski, M. S., & Andrews, A. G. (2012). Widespread rifting and retreat of ice-shelf margins in the eastern Amundsen Sea Embayment between 1972 and 2011. Journal of Glaciology, 58(209), 458–466.

Malyarenko, A., Robinson, N. J., Williams, M. J. M., & Langhorne, P. J. (2019). A Wedge Mechanism for Summer Surface Water Inflow Into the Ross Ice Shelf Cavity. Journal of Geophysical Research: Oceans, 124(2), 1196–1214.

McDougall, T. J., Barker, P. M., Feistel, R., & Galton-Fenzi, B. K. (2014). Melting of Ice and Sea Ice into Seawater and Frazil Ice Formation. Journal of Physical Oceanography, 44(7), 1751–1775.

McDougall, Trevor J., & Barker, Paul M. (2011). Getting started with TEOS-10 and the Gibbs Seawater (GSW) oceanographic toolbox. SCOR/IAPSO WG, 127, 1–28.

McMillan, M., Shepherd, A., Sundal, A., Briggs, K., Muir, A., Ridout, A., Hogg, A., & Wingham, D. (2014). Increased ice losses from Antarctica detected by CryoSat-2. Geophysical Research Letters, 41(11), 3899–3905.

Merino, N., Jourdain, N. C., Le Sommer, J., Goosse, H., Mathiot, P., & Durand, G. (2018). Impact of increasing antarctic glacial freshwater release on regional sea-ice cover in the Southern Ocean. Ocean Modelling, 121, 76–89.

Moffat, C., Beardsley, R. C., Owens, B., & van Lipzig, N. (2008). A first description of the Antarctic Peninsula Coastal Current. Deep Sea Research Part II: Topical Studies in Oceanography, 55(3), 277–293.

Moholdt, G., Padman, L., & Fricker, H. A. (2014). Basal mass budget of Ross and Filchner-Ronne ice shelves, Antarctica, derived from Lagrangian analysis of ICESat altimetry. Journal of Geophysical Research: Earth Surface, 119(11), 2361–2380.

Morlighem, M., Rignot, E., Binder, T., Blankenship, D., Drews, R., Eagles, G., Eisen, O., Ferraccioli, F., Forsberg, R., Fretwell, P., Goel, V., Greenbaum, J. S., Gudmundsson, H., Guo, J., Helm, V., Hofstede, C., Howat, I., Humbert, A., Jokat, W., Young, D. A. (2020). Deep glacial troughs and stabilizing ridges unveiled beneath the margins of the Antarctic ice sheet. Nature Geoscience, 13(2), 132–137.

Motyka, R. J., Dryer, W. P., Amundson, J., Truffer, M., & Fahnestock, M. (2013). Rapid submarine melting driven by subglacial discharge, LeConte Glacier, Alaska. Geophysical Research Letters, 40(19), 5153–5158.

Mouginot, J., Rignot, E., & Scheuchl, B. (2014). Sustained increase in ice discharge from the Amundsen Sea Embayment, West Antarctica, from 1973 to 2013. Geophysical Research Letters, 41(5), 1576–1584.

Mouginot, J, Scheuchl, B, & Rignot, E. (n.d.). MEaSUREs Antarctic Boundaries for IPY 2007-2009 from Satellite Radar, Version 2. NASA National Snow and Ice Data Center Distributed Active Archive Center.

Mouginot, Jeremie, Rignot, E., Scheuchl, B., & Millan, R. (2017). Comprehensive Annual Ice Sheet Velocity Mapping Using Landsat-8, Sentinel-1, and RADARSAT-2 Data. Remote Sensing, 9(4), 364.

Nakayama, Y., Timmermann, R., Rodehacke, C. B., Schröder, M., & Hellmer, H. H. (2014). Modeling the spreading of glacial meltwater from the Amundsen and Bellingshausen Seas. Geophysical Research Letters, 41(22), 7942–7949.

Nerem, R. S., Beckley, B. D., Fasullo, J. T., Hamlington, B. D., Masters, D., & Mitchum, G. T. (2018). Climate-change–driven accelerated sea-level rise detected in the altimeter era. Proceedings of the National Academy of Sciences, 115(9), 2022–2025.

Nicholls, K. W. (1997). Predicted reduction in basal melt rates of an Antarctic ice shelf in a warmer climate. Nature, 388(6641), 460–462.

Nicholls, K. W., & Østerhus, S. (2004). Interannual variability and ventilation timescales in the ocean cavity beneath Filchner-Ronne Ice Shelf, Antarctica. Journal of Geophysical Research: Oceans, 109(C4).

Nicolas, J. P., Vogelmann, A. M., Scott, R. C., Wilson, A. B., Cadeddu, M. P., Bromwich, D. H., Verlinde, J., Lubin, D., Russell, L. M., Jenkinson, C., Powers, H. H., Ryczek, M., Stone, G., & Wille, J. D. (2017). January 2016 extensive summer melt in West Antarctica favoured by strong El Niño. Nature Communications, 8(1), 1–10.

Padman, L., Fricker, H. A., Coleman, R., Howard, S., & Erofeeva, L. (2002). A new tide model for the Antarctic ice shelves and seas. Annals of Glaciology, 34, 247–254.

Paolo, F. S., Fricker, H. A., & Padman, L. (2015). Volume loss from Antarctic ice shelves is accelerating. Science, 348(6232), 327–331.

Paolo, F. S., Padman, L., Fricker, H. A., Adusumilli, S., Howard, S., & Siegfried, M. R. (2018). Response of Pacific-sector Antarctic ice shelves to the El Niño/Southern Oscillation. Nature Geoscience, 11(2), 121–126.

Paolo, Fernando S., Fricker, H. A., & Padman, L. (2016). Constructing improved decadal records of Antarctic ice shelf height change from multiple satellite radar altimeters. Remote Sensing of Environment, 177, 192–205.

Pauling, A. G., Smith, I. J., Langhorne, P. J., & Bitz, C. M. (2017). Time-Dependent Freshwater Input From Ice Shelves: Impacts on Antarctic Sea Ice and the Southern Ocean in an Earth System Model. Geophysical Research Letters, 44(20), 10,454-10,461.

Petty, A. A., Holland, P. R., & Feltham, D. L. (2014). Sea ice and the ocean mixed layer over the Antarctic shelf seas. The Cryosphere, 8(2), 761–783.

Porter, D. F., Springer, S. R., Padman, L., Fricker, H. A., Tinto, K. J., Riser, S. C., & Bell, R. E. (2019). Evolution of the Seasonal Surface Mixed Layer of the Ross Sea, Antarctica, Observed With Autonomous Profiling Floats. Journal of Geophysical Research: Oceans, 124(7), 4934–4953.

Pritchard, H. D., Ligtenberg, S. R. M., Fricker, H. A., Vaughan, D. G., van den Broeke, M. R., & Padman, L. (2012). Antarctic ice-sheet loss driven by basal melting of ice shelves. Nature, 484(7395), 502–505.

Reese, R., Gudmundsson, G. H., Levermann, A., & Winkelmann, R. (2018). The far reach of ice-shelf thinning in Antarctica. Nature Climate Change, 8(1), 53–57.

Rignot, E., Jacobs, S., Mouginot, J., & Scheuchl, B. (2013). Ice-Shelf Melting Around Antarctica. Science, 341(6143), 266–270.

Rignot, Eric, Mouginot, J., & Scheuchl, B. (2017). MEaSUREs InSAR-Based Antarctica Ice Velocity Map, Version 2. NASA National Snow and Ice Data Center Distributed Active Archive Center.

Rintoul, S. R. (2018). The global influence of localized dynamics in the Southern Ocean. Nature, 558(7709), 209–218.

Rye, C. D., Naveira Garabato, A. C., Holland, P. R., Meredith, M. P., George Nurser, A. J., Hughes, C. W., Coward, A. C., & Webb, D. J. (2014). Rapid sea-level rise along the Antarctic margins in response to increased glacial discharge. Nature Geoscience, 7(10), 732–735.

Scambos, T. A., Bohlander, J. A., Shuman, C. A., & Skvarca, P. (2004). Glacier acceleration and thinning after ice shelf collapse in the Larsen B embayment, Antarctica. Geophysical Research Letters, 31(18).

Scambos, T., Fricker, H. A., Liu, C.-C., Bohlander, J., Fastook, J., Sargent, A., Massom, R., & Wu, A.-M. (2009). Ice shelf disintegration by plate bending and hydro-fracture: Satellite observations and model results of the 2008 Wilkins ice shelf break-ups. Earth and Planetary Science Letters, 280(1), 51–60.

Schaffer, J., Timmermann, R., Arndt, J. E., Kristensen, S. S., Mayer, C., Morlighem, M., & Steinhage, D. (2016). A global, high-resolution data set of ice sheet topography, cavity geometry, and ocean bathymetry. Earth System Science Data, 8(2), 543–557.

Schlosser, P., Bayer, R., Foldvik, A., Gammelsrød, T., Rohardt, G., & Münnich, K. O. (1990). Oxygen 18 and helium as tracers of ice shelf water and water/ice interaction in the Weddell Sea. Journal of Geophysical Research, 95(C3), 3253.

Smethie, W. M., & Jacobs, S. S. (2005). Circulation and melting under the Ross Ice Shelf: Estimates from evolving CFC, salinity and temperature fields in the Ross Sea. Deep Sea Research Part I: Oceanographic Research Papers, 52(6), 959–978.

Smith, B. E., Fricker, H. A., Joughin, I. R., & Tulaczyk, S. (2009). An inventory of active subglacial lakes in Antarctica detected by ICESat (2003–2008). Journal of Glaciology, 55(192), 573–595.

Smith, B., Fricker, H. A., Gardner, A. S., Medley, B., Nilsson, J., Paolo, F. S., Holschuh, N., Adusumilli, S., Brunt, K., Csatho, B., Harbeck, K., Markus, T., Neumann, T., Siegfried, M. R., & Zwally, H. J. (2020). Pervasive ice sheet mass loss reflects competing ocean and atmosphere processes. Science.

Soussi, B, Urien, S, Picard, B, Muir, A, Roca, M, & Garcia, P. (2018). ENVISAT Altimetry Level 2 Product Handbook. European Space Agency. ftp://ra2-ftp-ds.eo.esa.int/ENVISAT_RA2

Stevens, C. M., Verjans, V., Lundin, J. M. D., Kahle, E. C., Horlings, A. N., Horlings, B. I., &

Waddington, E. D. (2020). The Community Firn Model (CFM) v1.0. Geoscientific Model Development Discussions, 1–37.

Stewart, C. L., Christoffersen, P., Nicholls, K. W., Williams, M. J. M., & Dowdeswell, J. A. (2019). Basal melting of Ross Ice Shelf from solar heat absorption in an ice-front polynya. Nature Geoscience, 12(6), 435–440.

The IMBIE team. (2018). Mass balance of the Antarctic Ice Sheet from 1992 to 2017. Nature, 558(7709), 219–222.

Thomas, R. H., Sanderson, T. J. O., & Rose, K. E. (1979). Effect of climatic warming on the West Antarctic ice sheet. Nature, 277(5695), 355–358.

Tinto, K. J., Padman, L., Siddoway, C. S., Springer, S. R., Fricker, H. A., Das, I., Tontini, F. C., Porter, D. F., Frearson, N. P., Howard, S. L., Siegfried, M. R., Mosbeux, C., Becker, M. K., Bertinato, C., Boghosian, A., Brady, N., Burton, B. L., Chu, W., Cordero, S. I., Bell, R. E. (2019). Ross Ice Shelf response to climate driven by the tectonic imprint on seafloor bathymetry. Nature Geoscience, 12(6), 441–449.

Turner, J., Orr, A., Gudmundsson, G. H., Jenkins, A., Bingham, R. G., Hillenbrand, C.-D., & Bracegirdle, T. J. (2017). Atmosphere-ocean-ice interactions in the Amundsen Sea Embayment, West Antarctica. Reviews of Geophysics, 55(1), 235–276.

Washam, P., Nicholls, K. W., Münchow, A., & Padman, L. (2019). Summer surface melt thins Petermann Gletscher Ice Shelf by enhancing channelized basal melt. Journal of Glaciology, 65(252), 662–674.

Wessem, J. M. van, Berg, W. J. van de, Noël, B. P. Y., Meijgaard, E. van, Amory, C., Birnbaum, G., Jakobs, C. L., Krüger, K., Lenaerts, J. T. M., Lhermitte, S., Ligtenberg, S. R. M., Medley, B., Reijmer, C. H., Tricht, K. van, Trusel, L. D., Ulft, L. H. van, Wouters, B., Wuite, J., & Broeke, M. R. van den. (2018). Modelling the climate and surface mass balance of polar ice sheets using RACMO2 – Part 2: Antarctica (1979–2016). The Cryosphere, 12(4), 1479–1498.

Williams, G. D., Herraiz-Borreguero, L., Roquet, F., Tamura, T., Ohshima, K. I., Fukamachi, Y., Fraser, A. D., Gao, L., Chen, H., McMahon, C. R., Harcourt, R., & Hindell, M. (2016). The suppression of Antarctic bottom water formation by melting ice shelves in Prydz Bay. Nature Communications, 7(1), 1–9.

Wingham, D. J. (2002). CryoSat: A mission to determine fluctuations in the Earth's ice fields. IEEE International Geoscience and Remote Sensing Symposium, 3, 1750–1752 vol.3.

Chapter 5

Atmospheric River Precipitation Contributed to Rapid Increases in Surface Height of the West Antarctic Ice Sheet in 2019

Abstract

Estimating the relative contributions of the atmospheric and dynamic components of ice-sheet mass balance is critical for improving projections of future sea level rise. Existing estimates of changes in Antarctic ice-sheet height, which can be used to infer changes in mass, are only accurate at multiyear time scales. However, NASA's Ice, Cloud, and land Elevation Satellite-2 (ICESat-2) laser altimetry mission now allows us to accurately measure changes in ice-sheet height at subannual time scales. Here, we use ICESat-2 data to estimate height changes over Antarctica between April 2019 and June 2020. These data show widespread increases in surface height over West Antarctica during the 2019 austral winter. Using climate reanalysis data, we show that 41% of increases in height during winter were from snow accumulation via extreme precipitation events—63% of these events were associated with landfalling atmospheric rivers (ARs) which occurred only 5.1% of the time.

5.1 Introduction

The net mass balance of the Antarctic Ice Sheet is the result of mass gains and losses from competing processes due to interactions between ice, ocean, and atmosphere acting on decadal to centennial time scales, and ultimately contributes to sea level (Smith et al., 2020a). Ongoing mass loss is occurring due to increased ice flow into the ocean driven by excess ocean-driven melting of its floating ice shelves (Adusumilli et al., 2020; Gudmundsson et al., 2019), which is partially offset by increased snowfall over the interior (Medley & Thomas, 2019). Improvements in projections of future mass loss require observational constraints on these processes, which can be estimated using a variety of satellite-based techniques (e.g., IMBIE Team, 2018).

Satellite altimeters make precise measurements of changes in ice sheet height at high spatial resolution; height changes can occur due to surface processes (e.g., Helsen et al., 2008) or changes in ice flow (e.g., Gardner et al., 2018). Separating these components is critical for understanding the atmosphere and ocean drivers of mass loss, and requires estimates of height change due to surface processes that are typically made using models of the atmosphere and near-surface firn (e.g., Ligtenberg et al., 2011). Although several studies have used a combination of satellite altimetry and firn models to measure changes over the ice sheet at interannual to decadal time scales (e.g., Shepherd et al., 2019; Smith et al., 2020a), changes at shorter periods, such as those due to extreme precipitation, have not been adequately considered. Field observations, model outputs, and some remote sensing measurements have shown that large height changes can occur over the ice sheet at short-period time scales. For example, atmospheric rivers (ARs) can drive large amounts of snowfall (Gorodetskaya et al., 2014) and snowmelt (Wille et al., 2019) over a period of days, and changes in ocean forcing can drive changes in ice flux within a span of months (Christianson et al., 2016).

The Ice, Cloud and land Elevation Satellite-2 (ICESat-2) was launched in September 2018 and carries a laser altimeter (the Advanced Topographic Laser Altimeter System; ATLAS), which provides near-complete coverage of the ice sheets up to 88° latitude. The high precision of the altimeter, the small footprint of the ATLAS beam, and the minimal penetration of the green laser into the snowpack provide an unambiguous height measurement over the ice sheets. Here, we use data from the ICESat-2 mission to estimate height changes over the Antarctic Ice Sheet between April 2019 and June 2020. We focus on the West Antarctic Ice Sheet (WAIS), where we observe large increases in surface height. Using model outputs from the Modern-Era Retrospective Analysis for Research and Applications, Version 2 (MERRA-2) reanalysis (Gelaro et al., 2017), we show that these height increases were due to several short-duration extreme (top 5%) precipitation events occurring primarily in the austral winter of 2019. Around half of all extreme precipitation coincided with landfalling ARs, suggesting that ARs could have a major influence on the surface mass balance of WAIS.

5.2. Atmospheric drivers of ice sheet change

5.2.1 Atmospheric forcing of height and mass changes over West Antarctica

Atmospheric processes play a major role in determining changes in surface height and mass over WAIS. These impacts can be direct, through changes in precipitation and snowmelt, or indirect, such as through changes in firn compaction or through atmospheric forcing of changes in ocean-induced ice shelf basal melt (e.g., Paolo et al., 2018; Thoma et al., 2008; Turner et al., 2017). Precipitation over WAIS mainly occurs through a combination of clear-sky snowfall from “diamond dust” (e.g., Sato et al., 1981) and intrusions of marine air that can provide a large quantity of snow over a short period of time (e.g., Turner et al., 2019). Marine air intrusions, sometimes occurring through landfalling ARs, can also increase snowmelt over the ice sheet (e.g., Nicolas et al., 2017; Scott et al., 2019; Wille et al., 2019), which can cause a relative decrease in the height of the snow surface (e.g., Pritchard et al., 2012).

Atmospheric conditions over WAIS are strongly influenced by the strength and location of the Amundsen Sea Low (ASL), a low-pressure system whose climatological center is typically located off the coast of WAIS. The ASL changes seasonally: it is typically weaker and its center is located over the west of the Antarctic Peninsula in the summer, and is stronger and north of Ross Ice Shelf in the winter (Fogt et al., 2012). This seasonal pattern in ASL is responsible for increased winter precipitation over WAIS (Hosking et al., 2013). Major drivers of changes in the ASL include the Southern Annular Mode, a leading mode of atmospheric variability in the Southern Hemisphere, and teleconnections from the tropical Pacific associated with the El Niño-Southern Oscillation (e.g., Ding et al., 2011; Fogt et al., 2011; Thompson & Wallace, 2000; Turner, 2004).

5.2.2. Atmospheric rivers in polar regions

ARs are long, narrow bands of anomalously high moisture transport, typically contained in the lowest 4 km of the atmosphere, and often associated with extratropical cyclones (e.g., Ralph et al., 2017). ARs can be detected using measurements made from ground-based, airborne, and satellite platforms and regional models (e.g., O'Brien et al., 2020; Ralph et al., 2019; Wick et al., 2013). However, most studies over polar regions have used outputs from atmospheric reanalysis because of a lack of observations. In reanalysis data, ARs can be identified as regions where there is an exceptional amount of moisture being advected horizontally in the lower portions of the troposphere concentrated in long (typically >2,000 km) but narrow regions (e.g., Ralph et al., 2019). The techniques used to detect ARs in midlatitude or subtropical regions differ from those used near the ice sheets because of the lower saturation capacity of the troposphere in polar regions and the strong katabatic winds present near the ice sheet surface (Gorodetskaya et al., 2014). ARs can deliver large amounts of snowfall over both ice sheets: for Antarctica, the frequency of landfalling ARs and the associated amount of snowfall can be highly variable (Gorodetskaya et al., 2014; Mattingly et al., 2018; Wille et al., 2020). At the same time, ARs can also drive increased snowmelt in both Antarctica (Wille et al., 2020) and Greenland (Mattingly et al., 2018), with the hypothesis that increased cloud liquid and ice water content in ARs enhances downward longwave radiation (e.g., Bennartz et al., 2013). Therefore, it is necessary to quantify the competing influences of ARs on the surface mass balance of the ice sheets.

5.3. ICESat-2 Detection of Height Changes

5.3.1. ICESat-2 Data and Repeat-track Analysis

ICESat-2's ATLAS instrument was designed to provide estimates of surface height using three pairs of green laser beams (Markus et al., 2017). On the ground, the two beams within a beam pair are separated by around 90 m and each beam pair is separated by around 3.3 km. During typical ICESat-2 operation over the ice sheet, the central beam pair straddles a reference ground track (RGT). Data were collected along the same RGTs every 91 days. Each ICESat-2 cycle constitutes data collection for all of its 1387 RGTs, starting with 1, over a 91-day period. The laser altimeter started pointing to the RGTs in March 2019, before the planned acquisition of data over RGT 1 in Cycle 3.

We estimated height changes over the Antarctic Ice Sheet using ATL06 data from five 91-day cycles (Cycle 3 to Cycle 7; May 2019 to May 2020) of the ICESat-2 mission. We first removed all data flagged by the "ATL06 quality summary", which highlights segments with high surface slope or roughness, high uncertainty in surface height, unreliable higher-level data, or cloudy conditions. We also removed ATL06 segments over which repeat data were not available within a distance of 22 m (approximately two times the ATLAS beam footprint). For any two given cycles, denoted ‘a’ and ‘b’, we used the ATL06 estimates of surface height, h_a and h_b, across-track slope for each beam pair, s_a and s_b, and the absolute value of the distance from the RGT, d_a and d_b,to estimate the height change Δh using

$$\Delta h= (h_b- h_a) + (d_b- d_a)\, s_b, \text{ if } d_b \geq d_a$$
$$\Delta h= (h_b- h_a) + (d_a- d_b)\, s_a, \text{ if } d_a > d_b.$$

We removed all ATL06 segments for which Δh over the 91-day period (Δt) exceeded a rate of 50 m/yr, or if the difference in $\Delta h/\Delta t$ between neighbouring segments exceeded 10 m/yr. We also removed all segments for which there was not a neighbouring segment with valid data.

5.3.2. Changes in ice sheet height, 2019–2020

ICESat-2's high-resolution high-precision repeat-track measurements of height change over the Antarctic Ice Sheet reveal new signals, and detect detailed patterns of change previously unresolved by other instruments. Because there is negligible penetration of the laser into the snowpack, height change estimates from ICESat-2 can be unambiguously linked to surface and dynamic processes. Similar to previous laser altimetry studies (e.g., Smith et al., 2020b), spatial patterns of height change between Cycle 3 (May 2019; month representing the central month of the 91-day acquisition period) and Cycle 7 (May 2020) show the combined influence of atmospheric processes and ice sheet dynamics (Figure 1). The largest decreases in height occurred at the Amundsen and Bellingshausen coasts in West Antarctica, likely a response to changes in ocean forcing of ice shelf melt (e.g., Adusumilli et al., 2020; Jenkins et al., 2018) in those sectors. In contrast, there were smaller increases in surface height in the interior of WAIS due to increases in the rate of snowfall minus evaporation (S − E).

Shorter-period (3 months) changes between consecutive ICESat-2 cycles over WAIS (defined in this study as the region shown within the inset box in Figure 1) showed significant spatial and temporal variability (Figures 2a–2c), and contrasts between seasons. In this study, we define austral winter as the period between May and October and austral summer as the period between November and April. During the austral winter between Cycle 3 (May 2019) and Cycle 4 (August 2019), there was a widespread increase in surface height across the ice sheet, with the largest increases occurring closer to the coast. Between Cycle 4 (August 2019) and Cycle 5 (November 2019), representing the transition between austral winter and austral summer, many regions showed decreases in height. This was followed by a widespread decrease in height across the WAIS during the austral summer between Cycle 5 (November 2019) and Cycle 6 (February 2020).

5.4. Drivers of observed changes in ice sheet height over West Antarctica

5.4.1. Atmospheric forcing of observed height changes

We can examine the relative contribution of atmospheric drivers to the observed height changes using models of firn layer thickness change ($\varDelta h_{firn}$). These models can incorporate a wide range of complexity, from a simple scaling of changes in $S - E$ to a full firn densification model (FDM) that includes processes such as compaction of the entire firn column and surface melt. Here, we use three estimates of $\varDelta h_{firn}$, from (1) changes in MERRA-2 $S - E$scaled using a constant surface snow density of $\rho_{350} = 350$ kg/m^3 (2) changes in MERRA-2 $S - E$ scaled using a map of spatially varying surface snow density $\rho(x, y)$ derived using in situ firn depth-density measurements (Medley et al., 2020), and (3) version 1 of the GSFC-FDM (Smith et al., 2020a; Medley et al., 2020). Estimates from (2) are shown in Figure 2d-f. For (1) and (2), we use MERRA-2 $S - E$ to estimate height changes because surface melt is not a direct output of MERRA-2 and we do not expect rainfall to drive increases in height of the snow surface. For (3), GSFC-FDM simulates changes in the firn column at 5 day temporal sampling using a calibrated Arthern et al. (2010) densification scheme implemented through the Community Firn Model (Stevens et al., 2020). The FDM is forced using precipitation minus evaporation, skin temperature and meltwater flux from a degree-day model using outputs derived from a combination of the MERRA-2 reanalysis and an offline 12.5 km resolution MERRA-2 'replay' (Smith et al., 2020a). For consistency, we sampled the estimates of Δh_{firn} to the same acquisition times and locations as the ICESat-2 data.

The widespread increase in the altimeter-derived height change ($\Delta h/\Delta t$) over WAIS during austral winter was due to increased $\Delta h_{firn}/\Delta t$ during that period (Figure 2d). The magnitudes of $\Delta h_{firn}/\Delta t$ for the time periods represented by the subsequent two cycle-to-cycle height change estimates were smaller (Figure 2e-f). The difference between $\Delta h/\Delta t$ and $\Delta h_{firn}/\Delta t$ for all three cases (Figure 2g-i) reveals height changes due to changes in ice dynamics and inadequacies of our Δh_{firn} estimate, including errors in the MERRA-2 reanalysis, in fully representing the height changes due to atmospheric and densification processes.

To evaluate the efficacy of the three techniques described above in representing height changes of the snow surface, we used a metric based on variance reduction, defined here as 1 - $var(\Delta h - \Delta h_{firn})/var(\Delta h)$. In all cases, subtracting Δh_{firn} from Δh reduced the variance in the gridded data (Figure 2g-i). For height changes between cycle 3 and cycle 4, the variance reduction was 62% for estimates of Δh_{firn} from both the FDM and $S - E$ scaled using $\rho(x, y)$, but decreased to 58% when $S - E$ was scaled using ρ_{350}. For height changes between cycle 4 and cycle 5, the variance reduction increased from 3% for the estimates that use ρ_{350} to 6% for the estimates that use $\rho(x, y)$, and to 17% for estimates from the FDM. For height changes between cycle 5 and cycle 6, the FDM could not be sampled because data were only available until the end of 2019, but the variance reduction was similar between the estimates that use ρ_{350} (42%) and those that use $\rho(x, y)$ (40%). For height changes between cycle 6 and cycle 7 (not shown in Figure 2), variance reduction increased from 2% for the estimates that use ρ_{350} to 10% for the estimates that use $\rho(x, y)$. From this evaluation, we find that using a full FDM is preferable over using only $S - E$ to estimate Δh_{firn}, with a relative impact that depends on the time period in consideration. If a full FDM is not available, Δh_{firn} estimates made by scaling $S - E$values using a spatially variable surface snow density field are preferable over estimates scaled using a constant density.

5.4.2. Atmospheric river detection

We examined the contributions of ARs toward the observed height changes. The technique we used to detect ARs landfalling over WAIS is nearly identical to that described by Wille et al., (2019). Detections are based on vertically integrated water vapor (*IWV*), which we calculate at 6-hourly intervals using specific humidity (*q*) from the MERRA-2 reanalysis summed over the 300–900 hPa pressure levels:

$$IWV = \frac{1}{g} \int_{300\ hPa}^{900\ hPa} q\, dp,$$

where g is the acceleration due to gravity and $dp$is the spacing of the pressure levels in the reanalysis data. We calculated IWV values between 2000 and 2020 for regions between 45S–90S and 60W–180W. We catalogued an AR if IWV values in a region that spanned at least 20° (>2200 km) in the meridional direction, allowing for discontinuities no larger than 1°, and were in the top 2% of monthly averaged MERRA-2 climatologies. For each month, the climatologies represented all 6h IWV values between 2000 and 2019. In our analysis, we only considered periods during which AR conditions intersected with the grounded portion of WAIS. Another frequently used metric to detect ARs is the vertically integrated vapor transport (*IVT*), which includes the role of moisture transport by winds in the lower troposphere (e.g., Ralph et al., 2019). The number of ARs detected in 2019 using *IVT* differed from the number detected using *IWV* by around 60%, which is consistent with differences over WAIS for previous years (Wille et al., 2019). However, the choice of metrics for AR detection did not affect the major conclusions of this study in any substantial way, as discussed below.

5.4.3. Contribution of atmospheric rivers to mass balance over West Antarctica

We detected AR conditions over WAIS during 3.9% of the 2019 calendar year (Figure 3a). The duration over which an AR can influence precipitation across a region depends on a variety of factors including AR intensity and orography (e.g., Hecht & Cordeira, 2017; Lamjiri et al., 2017, 2018). ARs have been observed to influence precipitation for up to 3 days in East Antarctica (Gorodetskaya et al., 2014). If we conservatively assume that an AR can influence precipitation during the AR detection period and 24 h following landfall, 19% of total precipitation in 2019 occurred through landfalling ARs (Figure 3a). Under this assumption, 55% of the periods with extreme (top 5%) precipitation followed AR landfalls in 2019. For ARs detected using IVT instead of IWV, 37% of the periods with extreme precipitation followed landfalls. A majority of the ARs (67%) and extreme precipitation events (78%) that occurred in 2019 were detected between May and October (austral winter). During this period, there was an 18 cm increase in surface height due to $S - E$ anomalies, and extreme precipitation events contributed to 41% of these increases. The subset of ARs that led to extreme precipitation contributed to 26% of total increases and the remaining ARs contributed to 9% of increases.

In addition to changes in $P - E$, ARs also contributed to increased surface melt in both summer and winter (Figure 3c). Here, we diagnosed surface melt using the percent area of the ice sheet with 2m air temperatures (T_{2m}) greater than $T_{melt} = 270.5$ K. The temperature of 270.5 K as a threshold for melt is an optimized value derived in Medley et al., (2020). This was obtained by minimizing r^2 and Root-mean-square error in a regression between remote sensing estimates of surface melt from Trusel et al., (2013) and T_{2m}-T_{melt} from MERRA-2. Using this metric, we find that around 90% of summer ARs and 10% of winter ARs coincided with potential surface melt over WAIS (Figure 3c). For ARs detected using IVT, around 70% of summer events and 5% of winter events coincided with potential melt. To estimate this, we upheld the assumption that ARs can influence atmospheric conditions until 24h after landfall. Increased surface melt from AR activity could lead to decreases in surface height. However, increases in h_{firn} from the FDM following ARs (Figure 3b) suggests that the increased precipitation, rather than the increased rate of surface melt, dominated the AR contribution towards surface height change. This is evident as increases in surface height following ARs throughout the year (Figure 3b). This could change in the future if the frequency or duration of ARs that make landfall over Antarctica increase as predicted (e.g., Payne et al., 2020).

We examined the associated synoptic conditions during June–September 2019 to investigate the atmospheric forcing of increases in $P - E$ and surface height during that period (Figure 3a, Figure 4). Anomalies in 500 hPa geopotential heights show a seasonally persistent ridge, higher than climatological values, centered near the Antarctic Peninsula. Additionally, a seasonally persistent low between Victoria Land and New Zealand was also present (see also Clem et al., 2020) and 60 m deeper than the 1980-2019 mean. This amplified, persistent, dipole pattern aided in the advection of positively anomalous moisture through AR activity, indicated by the enhanced AR activity, toward WAIS, resulting in anomalously high precipitation. This dipole was also present in sea level pressure anomalies (not shown here), indicating a westward motion and deepening of the ASL that enhanced seasonal precipitation over WAIS.

5.4.4 Longer-term context for mass changes in 2019

To place our results of inferred mass changes in 2019 into a longer-term context, we compared them with a longer period time series that we compiled for 2003–2019 from MERRA-2 $P - E$ and the GRACE/GRACE-FO missions (e.g., Velicogna et al., 2020). We estimated net mass balance from GRACE/GRACE-FO using mass concentration solutions from the Center for Space Research provided on a geodetic grid at an approximate spacing of 120 km (Save et al., 2016), which are designed to reduce "spatial leakage" of the mass balance signal compared to previous solutions. These solutions include corrections for some low-order spherical harmonic components of gravity change using satellite laser ranging (Loomis et al., 2019), and a correction for glacial isostatic adjustment using the ICE6G-D model (Peltier et al., 2018). These estimates show an increase in mass between June and September 2019 over WAIS (Figure 3d). This increase in mass was followed by a decrease that lasted at least until the end of 2019. The magnitude of mass gain was similar to the magnitude of increases in $P - E$ (Figure 3e). There was a 5.4 cm increase in $P - E$ and a 1.7 cm decrease in net mass in 2019. These values are higher than the average annual increase of 1.1 cm in $P - E$ and decrease of 3.9 cm in net mass between 2003 and 2019, and support our results that there was anomalously high austral winter precipitation over WAIS in 2019 (see also Lenaerts et al., 2020). We conclude that the presence of a seasonally persistent dipole near the Antarctic Peninsula in 2019 (Figure 4) was a likely driver of the observed increases in $P - E$ and net mass balance relative to past years.

5.5. Summary

We have used over a year of data from the ICESat-2 laser altimetry mission to estimate short-term (3 monthly) changes in height over the Antarctic Ice Sheet between April 2019 and June 2020. These data allow us to measure accurately changes at the snow interface with near complete coverage over the entire continent four times a year at high along-track spatial resolution. This represents a major improvement over previous height change estimates from satellite radar altimetry, whose measurements represent changes occurring at an ambiguous interface within the firn column, or previous airborne and spaceborne laser altimeters, which did not have sufficient spatial or temporal resolution for precise estimates of subannual height changes.

We found large increases in surface height over WAIS during the 2019 austral winter. We show that these signals were driven by increased snow accumulation during that period, with extreme precipitation events contributing to 41% of total increases in height driven by surface processes. Using reanalysis data, we show that over half of these extreme precipitation events occurred during or shortly after AR landfalls. This is significant because the frequency of ARs landfalling over Antarctica is expected to increase in the 21st century (Espinoza et al., 2018; Payne et al., 2020), which can change the contributions of precipitation and surface melt toward height and mass changes over the ice sheet. Ensuring that such events are well represented in firn models will be critical for accurately separating surface processes from ice dynamics using satellite altimetry, which is necessary to understand the drivers behind the Antarctic Ice Sheet contribution to sea level rise.

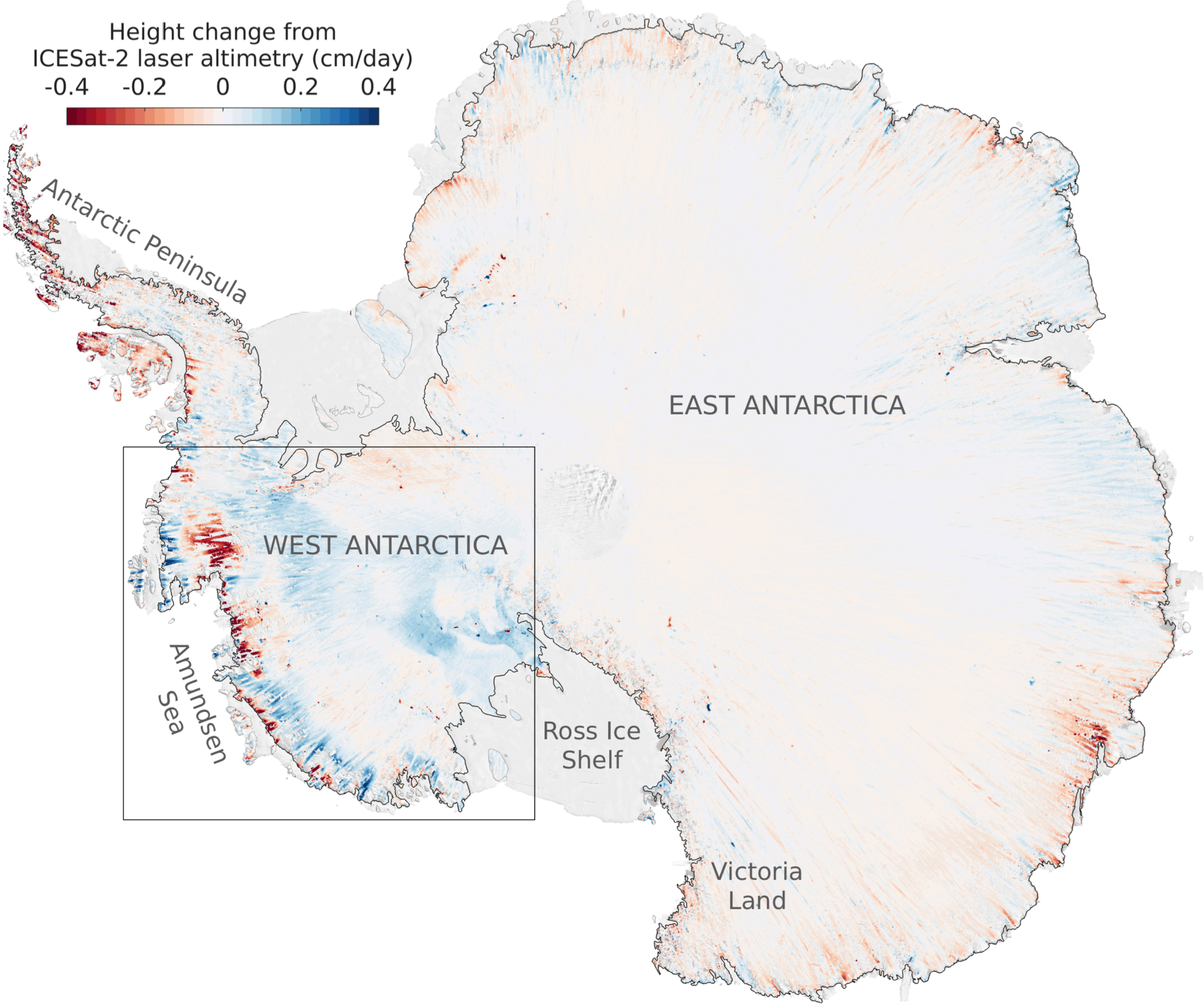

Figure 1: Surface height change over Antarctica between Cycle 7 (March 26, 2020 to June 25, 2020) and Cycle 3 (March 29, 2019 to June 26, 2019) estimated from ICESat-2 repeat-track laser altimetry.

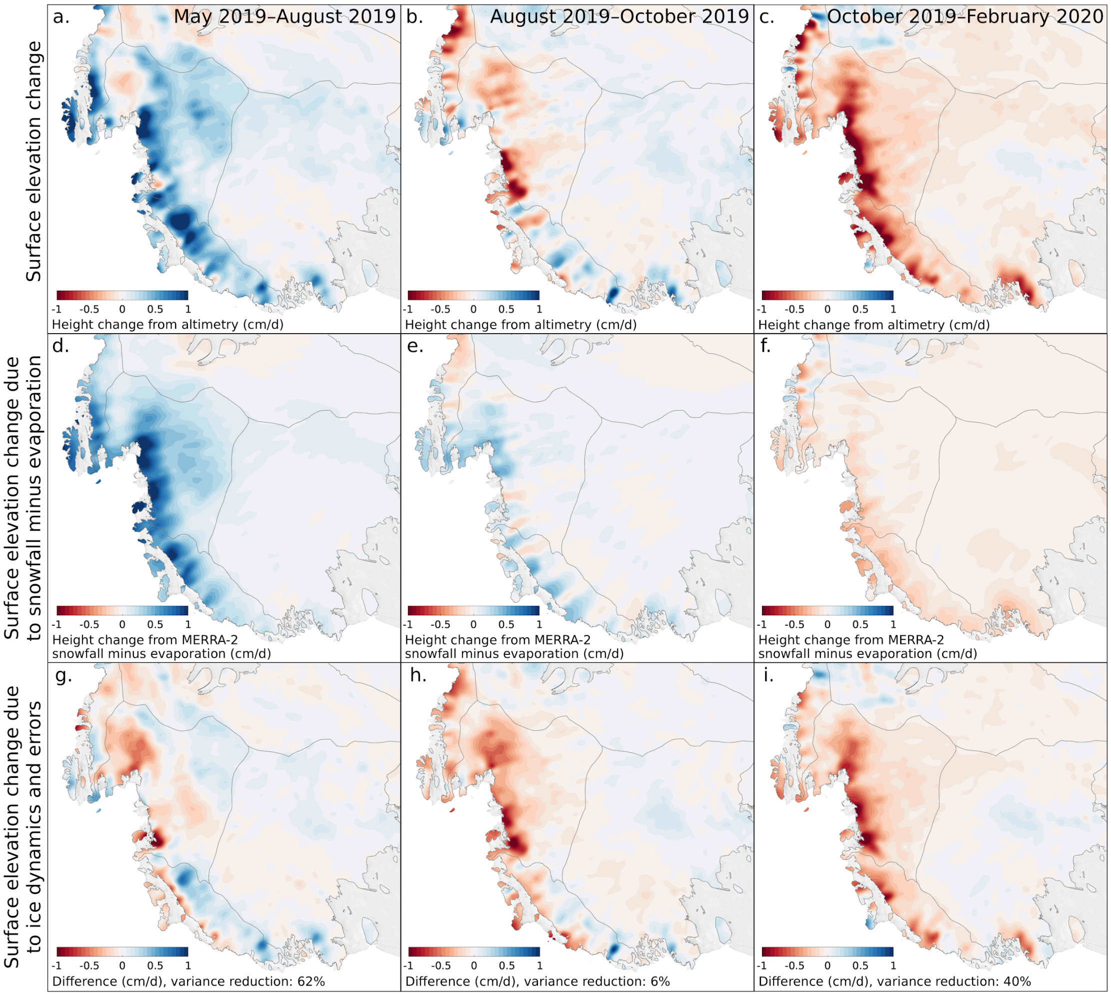

Figure 2: Surface height change over WAIS from (a–c) ICESat-2 repeat-track laser altimetry and (d–f) changes in snowfall minus evaporation ($S - E$) from the MERRA-2 reanalysis scaled using a map of spatially varying surface snow density. The reanalysis data were interpolated to the acquisition times and locations of the ICESat-2 data. (g–i) Differences between the height changes shown in (a–c) and those shown in (d–f), and the associated variance reduction. Here, we define the variance reduction as one minus the ratio of the altimeter-derived height changes corrected for changes in $S - E$ (g–i) and the altimeter-derived height changes (a–c). All maps were smoothed using a Gaussian filter with a 15-km diameter.

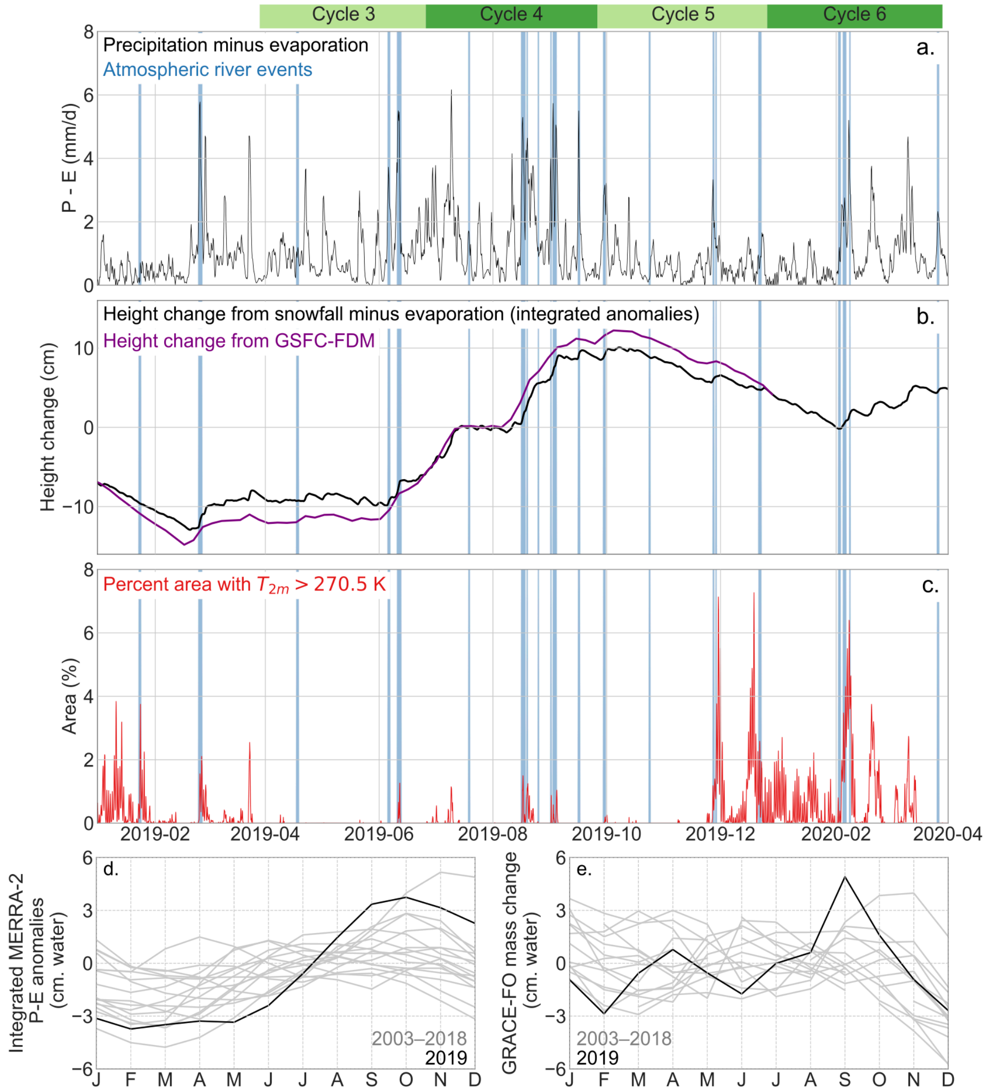

Figure 3: Changes in atmospheric conditions, inferred surface height, and mass balance over grounded ice in WAIS, defined here as the region within the inset box in Figure 1. (a) Precipitation minus evaporation (P − E) from the MERRA-2 reanalysis in mm of water equivalent per day at 6-h intervals. The green bars above (a) show the periods of acquisition of ICESat-2 data for Cycles 3–6. (b) Time series of expected surface height change from (1) integrated MERRA-2 snowfall minus evaporation anomalies relative to the 1980–2019 mean (black line) and (2) GSFC-FDM (purple line). Data from GSFC-FDM were only available until the end of 2019. (c) The percentage of grounded ice area with 2 m air temperatures exceeding 270.5 K, intended as a diagnostic of the ice sheet area with potential surface melt. The blue vertical bars in (a–c) show the time periods during which landfalling ARs were detected over WAIS. (d) Changes in integrated anomalies precipitation minus evaporation (P – E) anomalies relative to the 2003–2019 mean value from the MERRA-2 reanalysis. (e) Seasonal changes in ice-sheet mass from the GRACE/GRACE-FO missions for the 2003–2019 period.

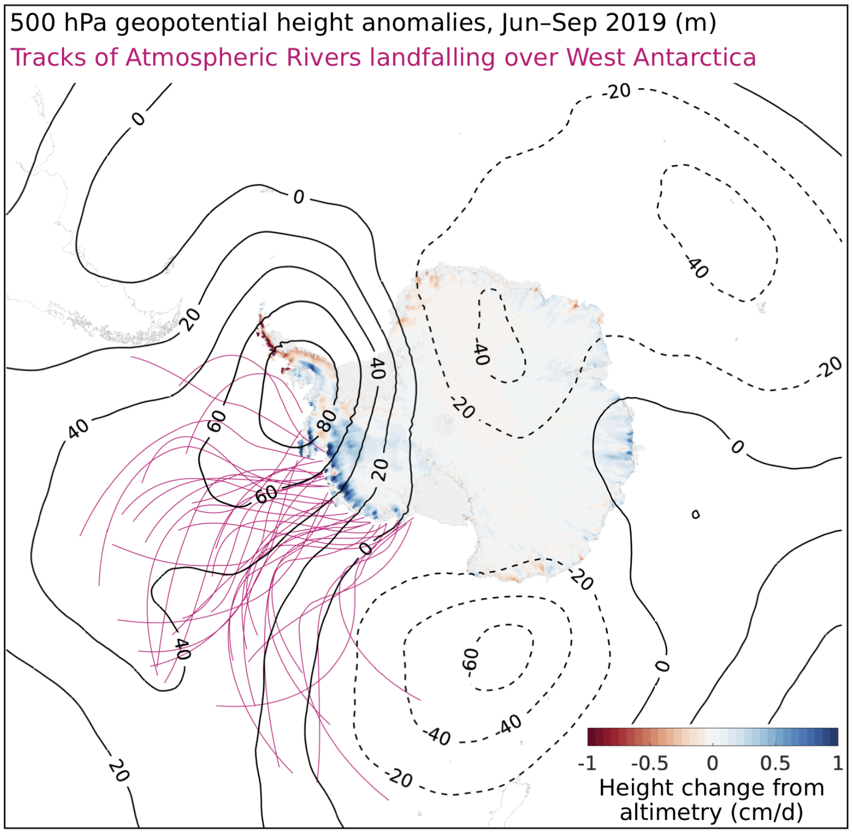

Figure 4: 500 hPa geopotential height anomalies from MERRA-2 for June to September 2019 relative to the 1980–2019 monthly mean values in m. Tracks of atmospheric rivers landfalling over WAIS (defined here as the region within the inset box in Figure 1) are shown as red lines. Height changes from ICESat-2 laser altimetry between Cycle 3 (April–June 2019) and Cycle 7 (July–September 2019) over Antarctic grounded ice are also shown.

Chapter 5, in full, is a reprint of the material as it appears in the journal Geophysical Research Letters. Adusumilli, S., Fish, M. A., Fricker, H. A., & Medley, B. (2021). Atmospheric river precipitation contributed to rapid increases in surface height of the West Antarctic Ice Sheet in 2019. *Geophysical Research Letters*, 48. The dissertation author was the primary investigator and author of this paper.

5.6 References

Adusumilli, S., Fricker, H. A., Medley, B., Padman, L., & Siegfried, M. R. (2020). Interannual variations in meltwater input to the Southern Ocean from Antarctic ice shelves. Nature geoscience, 13(9), 616-620.

Adodo, F. I., Remy, F., & Picard, G. (2018). Seasonal variations of the backscattering coefficient measured by radar altimeters over the Antarctic Ice Sheet. The Cryosphere, 12(5), 1767.

Bennartz, R., Shupe, M.D., Turner, D.D., Walden, V.P., Steffen, K., Cox, C.J., Kulie, M.S., Miller, N.B. and Pettersen, C. (2013). July 2012 Greenland melt extent enhanced by low-level liquid clouds. Nature, 496(7443), pp.83-86.

Brunt, K. M., Neumann, T. A., & Smith, B. E. (2019). Assessment of ICESat-2 ice sheet surface heights, based on comparisons over the interior of the Antarctic ice sheet. Geophysical Research Letters, 46(22), 13072-13078.

Christianson, K., Bushuk, M., Dutrieux, P., Parizek, B.R., Joughin, I.R., Alley, R.B., Shean, D.E., Abrahamsen, E.P., Anandakrishnan, S., Heywood, K.J. and Kim, T.W. (2016). Sensitivity of Pine Island Glacier to observed ocean forcing. Geophysical Research Letters, 43(20).

K. R. Clem, S. Barreira, R. L. Fogt, S. Colwell, L. M. Keller, M. A. Lazzara, and D. Mikolajczyk, 2020: Atmospheric circulation and surface observations [in "State of the Climate in 2019"]. Bull. Amer. Meteor. Soc., 101 (8), S304–S306.

Ding, Q., Steig, E. J., Battisti, D. S., & Küttel, M. (2011). Winter warming in West Antarctica caused by central tropical Pacific warming. Nature Geoscience, 4(6), 398-403.

Fogt, R. L., Bromwich, D. H., & Hines, K. M. (2011). Understanding the SAM influence on the South Pacific ENSO teleconnection. Climate Dynamics, 36(7-8), 1555-1576.

Fogt, R. L., Wovrosh, A. J., Langen, R. A., & Simmonds, I. (2012). The characteristic variability and connection to the underlying synoptic activity of the Amundsen-Bellingshausen Seas Low. Journal of Geophysical Research: Atmospheres, 117(D7).

Gardner, A. S., Moholdt, G., Scambos, T., Fahnstock, M., Ligtenberg, S., Van Den Broeke, M., & Nilsson, J. (2018). Increased West Antarctic and unchanged East Antarctic ice discharge over the last 7 years. Cryosphere, 12(2), 521-547.

Gelaro, R., McCarty, W., Suárez, M.J., Todling, R., Molod, A., Takacs, L., Randles, C.A., Darmenov, A., Bosilovich, M.G., Reichle, R. and Wargan, K. (2017). The modern-era retrospective analysis for research and applications, version 2 (MERRA-2). Journal of Climate, 30(14), pp.5419-5454.

Gorodetskaya, I. V., Tsukernik, M., Claes, K., Ralph, M. F., Neff, W. D., & Van Lipzig, N. P. (2014). The role of atmospheric rivers in anomalous snow accumulation in East Antarctica. Geophysical Research Letters, 41(17), 6199-6206.

Hecht, C.W. and Cordeira, J.M., 2017. Characterizing the influence of atmospheric river orientation and intensity on precipitation distributions over North Coastal California. Geophysical Research Letters, 44(17), pp.9048-9058.

Helsen, M. M., Van Den Broeke, M. R., Van De Wal, R. S., Van De Berg, W. J., Van Meijgaard, E., Davis, C. H., & Goodwin, I. (2008). Elevation changes in Antarctica mainly determined by accumulation variability. science, 320(5883), 1626-1629.

Hosking, J. S., Orr, A., Marshall, G. J., Turner, J., & Phillips, T. (2013). The influence of the Amundsen–Bellingshausen Seas low on the climate of West Antarctica and its representation in coupled climate model simulations. Journal of Climate, 26(17), 6633-6648.

Huning, L. S., Margulis, S. A., Guan, B., Waliser, D. E., & Neiman, P. J. (2017). Implications of detection methods on characterizing atmospheric river contribution to seasonal snowfall across Sierra Nevada, USA. Geophysical Research Letters, 44(20), 10-445.

Jenkins, A., Shoosmith, D., Dutrieux, P., Jacobs, S., Kim, T.W., Lee, S.H., Ha, H.K. and Stammerjohn, S. (2018). West Antarctic Ice Sheet retreat in the Amundsen Sea driven by decadal oceanic variability. Nature Geoscience, 11(10), pp.733-738.

J. Lenaerts, E. Keenan, M. Maclennan and T. Gorte, 2020: Surface mass balance of the ice sheet [in "State of the Climate in 2019"]. Bull. Amer. Meteor. Soc., 101 (8), S304–S306, https://doi.org/10.1175/BAMS-D-20-0090.1.

Landerer, F.W., Flechtner, F.M., Save, H., Webb, F.H., Bandikova, T., Bertiger, W.I., Bettadpur, S.V., Byun, S.H., Dahle, C., Dobslaw, H. and Fahnestock, E. (2020). Extending the global mass change data record: GRACE Follow-On instrument and science data performance. Geophysical Research Letters, 47(12).

Lamjiri, M. A., Dettinger, M. D., Ralph, F. M., & Guan, B. (2017). Hourly storm characteristics along the US West Coast: Role of atmospheric rivers in extreme precipitation. Geophysical Research Letters, 44(13), 7020-7028.

Lamjiri, M. A., Dettinger, M. D., Ralph, F. M., Oakley, N. S., & Rutz, J. J. (2018). Hourly analyses of the large storms and atmospheric rivers that provide most of California's precipitation in only 10 to 100 hours per year. San Francisco Estuary and Watershed Science, 16(4).

Ligtenberg, S. R. M., Helsen, M. M., & Van den Broeke, M. R. (2011). An improved semi-empirical model for the densification of Antarctic firn. The Cryosphere, 5, 809-819.

Loomis, B. D., Rachlin, K. E., & Luthcke, S. B. (2019). Improved Earth oblateness rate reveals increased ice sheet losses and mass-driven sea level rise. Geophysical Research Letters, 46(12), 6910-6917.

Markus, T., Neumann, T., Martino, A., Abdalati, W., Brunt, K., Csatho, B., Farrell, S., Fricker, H., Gardner, A., Harding, D. and Jasinski, M. (2017). The Ice, Cloud, and land Elevation Satellite-2 (ICESat-2): science requirements, concept, and implementation. Remote sensing of environment, 190, pp.260-273.

Mattingly, K. S., Mote, T. L., & Fettweis, X. (2018). Atmospheric river impacts on Greenland Ice Sheet surface mass balance. Journal of Geophysical Research: Atmospheres, 123(16), 8538-8560.

Medley, B., & Thomas, E. R. (2019). Increased snowfall over the Antarctic Ice Sheet mitigated twentieth-century sea-level rise. Nature Climate Change, 9(1), 34-39.

Medley, B., Neumann, T. A., Zwally, H. J., & Smith, B. E. (2020). Forty-year Simulations of Firn Processes over the Greenland and Antarctic Ice Sheets. The Cryosphere Discussions, 1-35.

Nicolas, J. P., Vogelmann, A. M., Scott, R. C., Wilson, A. B., Cadeddu, M. P., Bromwich, D. H., & Powers, H. H. (2017). January 2016 extensive summer melt in West Antarctica favoured by strong El Niño. Nature Communications, 8, 15799.

O'Brien, T.A., Payne, A.E., Shields, C.A., Rutz, J., Brands, S., Castellano, C., Chen, J., Cleveland, W., DeFlorio, M.J., Goldenson, N. & Gorodetskaya, I.V. (2020). Detection uncertainty matters for understanding atmospheric rivers. Bulletin of the American Meteorological Society, 101(6), pp.E790-E796.

Payne, A. E., Demory, M. E., Leung, L. R., Ramos, A. M., Shields, C. A., Rutz, J. J., & Ralph, F. M. (2020). Responses and impacts of atmospheric rivers to climate change. Nature Reviews Earth & Environment, 1-15.

Peltier, R. W., Argus, D. F., & Drummond, R. (2018). Comment on "An Assessment of the ICE-6G_C (VM5a) Glacial Isostatic Adjustment Model". Journal of Geophysical Research: Solid Earth, 123(2), 2019-2028.

Pritchard, H. D., Arthern, R. J., Vaughan, D. G., & Edwards, L. A. (2009). Extensive dynamic thinning on the margins of the Greenland and Antarctic ice sheets. Nature, 461(7266), 971-975.

Ralph, F. M., Wilson, A. M., Shulgina, T., Kawzenuk, B., Sellars, S., Rutz, J. J., & Nardi, K. M. (2019). ARTMIP-early start comparison of atmospheric river detection tools: How many atmospheric rivers hit northern California's Russian River watershed?. Climate Dynamics, 52(7-8), 4973-4994.

Raphael, M. N., Marshall, G. J., Turner, J., Fogt, R. L., Schneider, D., Dixon, D. A., & Hobbs, W. R. (2016). The Amundsen sea low: variability, change, and impact on Antarctic climate. Bulletin of the American Meteorological Society, 97(1), 111-121.

Rignot, E., Mouginot, J., Scheuchl, B., van den Broeke, M., van Wessem, M.J. and Morlighem, M. (2019). Four decades of Antarctic Ice Sheet mass balance from 1979–2017. Proceedings of the National Academy of Sciences, 116(4), pp.1095-1103.

Sato, N., Kikuchi, K., Barnard, S. C., & Hogan, A. W. (1981). Some characteristic properties of ice crystal precipitation in the summer season at South Pole Station, Antarctica. Journal of the Meteorological Society of Japan. Ser. II, 59(5), 772-780.

Save, H., S. Bettadpur, and B.D. Tapley (2016), High resolution CSR GRACE RL05 mascons, J. Geophys. Res. Solid Earth, 121.

Scambos, T.A., Bell, R.E., Alley, R.B., Anandakrishnan, S., Bromwich, D.H., Brunt, K., Christianson, K., Creyts, T., Das, S.B., DeConto, R. & Dutrieux, P. (2017). How much, how fast?: A science review and outlook for research on the instability of Antarctica's Thwaites Glacier in the 21st century. Global and Planetary Change, 153, pp.16-34.

Scott, R. C., Nicolas, J. P., Bromwich, D. H., Norris, J. R., & Lubin, D. (2019). Meteorological drivers and large-scale climate forcing of West Antarctic surface melt. Journal of Climate, 32(3), 665-684.

Shepherd, A., Ivins, E., Rignot, E., Smith, B., Van Den Broeke, M., Velicogna, I., Whitehouse, P., Briggs, K., Joughin, I., Krinner, G. and Nowicki, S. (2018). Mass balance of the Antarctic Ice Sheet from 1992 to 2017. Nature, 558, pp.219-222.

Shepherd, A., Gilbert, L., Muir, A. S., Konrad, H., McMillan, M., Slater, T., & Engdahl, M. E. (2019). Trends in Antarctic Ice Sheet elevation and mass. Geophysical Research Letters, 46(14), 8174-8183.

Smith, B. E., Fricker, H. A., Joughin, I. R., & Tulaczyk, S. (2009). An inventory of active subglacial lakes in Antarctica detected by ICESat (2003–2008). Journal of Glaciology, 55(192), 573-595.

Smith, B., Fricker, H. A., Holschuh, N., Gardner, A. S., Adusumilli, S., Brunt, K. M., & Nilsson, J. (2019). Land ice height-retrieval algorithm for NASA's ICESat-2 photon-counting laser altimeter. Remote Sensing of Environment, 233, 111352.

Smith, B., Fricker, H.A., Gardner, A.S., Medley, B., Nilsson, J., Paolo, F.S., Holschuh, N., Adusumilli, S., Brunt, K., Csatho, B. & Harbeck, K. (2020). Pervasive ice sheet mass loss reflects competing ocean and atmosphere processes. Science, 368(6496), pp.1239-1242.

Smith, B., H. A. Fricker, A. Gardner, M. R. Siegfried, S. Adusumilli, B. M. Csathó, N. Holschuh, J. Nilsson, F. S. Paolo, & the ICESat-2 Science Team. 2020b. ATLAS/ICESat-2

L3A Land Ice Height, Version 3. Boulder, Colorado USA. NASA National Snow and Ice Data Center Distributed Active Archive Center. [Date accessed: September 2020].

Thoma, M., Jenkins, A., Holland, D., & Jacobs, S. (2008). Modelling circumpolar deep water intrusions on the Amundsen Sea continental shelf, Antarctica. Geophysical Research Letters, 35(18).

Thompson, D. W., & Wallace, J. M. (2000). Annular modes in the extratropical circulation. Part I: Month-to-month variability. Journal of climate, 13(5), 1000-1016.

Trusel, L. D., Frey, K. E., Das, S. B., Munneke, P. K., & Van Den Broeke, M. R. (2013). Satellite-based estimates of Antarctic surface meltwater fluxes. Geophysical Research Letters, 40(23), 6148-6153.

Turner, J. (2004). The el nino–southern oscillation and antarctica. International Journal of Climatology: A Journal of the Royal Meteorological Society, 24(1), 1-31.

Turner, J., Orr, A., Gudmundsson, G. H., Jenkins, A., Bingham, R. G., Hillenbrand, C. D., & Bracegirdle, T. J. (2017). Atmosphere-ocean-ice interactions in the Amundsen Sea embayment, West Antarctica. Reviews of Geophysics, 55(1), 235-276.

Turner, J., Phillips, T., Thamban, M., Rahaman, W., Marshall, G. J., Wille, J. D., & van den Broeke, M. (2019). The dominant role of extreme precipitation events in Antarctic snowfall variability. Geophysical Research Letters, 46(6), 3502-3511.

Velicogna, I., Mohajerani, Y., Landerer, F., Mouginot, J., Noel, B., Rignot, E., & Wiese, D. (2020). Continuity of Ice Sheet Mass Loss in Greenland and Antarctica From the GRACE and GRACE Follow-On Missions. Geophysical Research Letters, 47(8), e2020GL087291.

Wick, G. A., Neiman, P. J., Ralph, F. M., & Hamill, T. M. (2013). Evaluation of forecasts of the water vapor signature of atmospheric rivers in operational numerical weather prediction models. Weather and Forecasting, 28(6), 1337-1352.

Wille, J. D., Favier, V., Dufour, A., Gorodetskaya, I. V., Turner, J., Agosta, C., & Codron, F. (2019). West Antarctic surface melt triggered by atmospheric rivers. Nature Geoscience, 12(11), 911-916.

Chapter 6

Conclusions

The objective of the research described in this dissertation was to quantify the variability in ice sheet height and mass using satellite radar and laser altimetry at sub-annual to interannual time scales, and to separate the contributions of the atmosphere and the ocean to the observed changes. Previous studies have shown considerable variability in the atmosphere and ocean surrounding Antarctica at these time scales, and incorporating the influence of this variability on ice sheet mass in models is critical for improving projections of future sea level rise. Despite this, most previous studies using satellite data to monitor ice sheet mass have only reported the total change that occurred over the satellite record and have not provided long, continuous time series that are more insightful for comparisons with climate records.

Background: In Chapter 2, we described the various satellite laser and radar altimeter missions used in this dissertation to estimate time series of changes in ice sheet height and mass for the period 1992-2020. We documented the techniques used to convert altimeter data to the heights over the grounded ice sheet, and the heights of ice shelves above the ocean surface. We described how we account for various contributions to height change using ancillary datasets so that changes in ocean-driven basal melting can be isolated. We also discussed the differences between how ice sheet heights are derived from radar and laser altimetry data, and how these differences affect the results presented in this dissertation.

We used satellite radar and laser altimetry data to study different mass budget processes over the floating and grounded portions of the Antarctic Ice Sheet, on various time scales, as follows:

Surface processes and basal melting – Antarctic Peninsula ice shelves – ERS-Envisat-CryoSat-2 radar altimetry, 1994-2016: In Chapter 3, we used satellite radar altimetry data collected between 1994 and 2016 to estimate changes in height of the floating ice shelves around the Antarctic Peninsula. We found decreases in the height of Larsen C Ice Shelf, the largest ice shelf in the Antarctic Peninsula, between 1994 and 2009 followed by an increase between 2009 and 2016; we validated these observations using airborne laser altimetry. Using a model of the atmosphere and the near-surface firn layer, we showed that these increases were primarily due to an increase in the firn air content driven by reduced surface melting. For ice shelves on the west side of the Antarctic Peninsula in the Bellingshausen Sea, we found an overall decline in mass during our record due to higher rates of ocean-driven basal melting than those required to keep the thickness of the ice shelf constant. There is a larger ocean influence on ongoing mass loss on the west side of the Antarctic Peninsula, while atmospheric forcing of changes in the properties of the surface snow layer affects ice shelf mass loss on both sides. These results provide a demonstration of how satellite altimetry data can be used to identify the influences of atmospheric and oceanic forcing of ice shelf change over the past two decades in a region that has changed rapidly during that period.

Basal melting –Antarctic ice shelves – ERS-Envisat-CryoSat-2 radar altimetry, 1994-2018: In Chapter 4, we used the same radar altimetry data used in Chapter 3, extended in time to 2018, to estimate changes in the rates of ocean-driven basal melting over nearly all Antarctic ice shelf areas between 1994 and 2018. In addition to that, we took advantage of the new technology used in the newest polar-orbiting radar altimeter, CryoSat-2 (launched in 2010), and its improved spatial sampling, to estimate the rate of basal melting of ice shelves between 2010–2018 at high spatial resolution. Together, these two datasets represent a major advance from previous continent-wide melt rate estimates, which were low spatial resolution averages for a 5-year period (2003-2008), and did not include any insights into temporal variability. Using these new data, we found large variations in basal melt rates integrated across the continent at interannual time scales. The highest values occurred in the late 2000s and led to net ice-shelf thinning. We also quantified mass loss due declines in ice shelf extent in the Antarctic Peninsula and some portions of West Antarctica between 1994 and 2018; this mass loss was similar in magnitude to that from thinning of ice shelves over the same time period. We identified the depths at which melting or refreezing was occurring, and highlighted the distinct oceanographic processes that determine melting at different depths. This is important because the depth at which melting occurs plays a major role in how the resulting meltwater affects the surrounding atmosphere, ocean, and ecosystems.

Surface accumulation – Antarctic Ice Sheet – ICESat-2 laser altimetry, 2019-2020: In Chapter 5, we used laser altimetry data from the Ice Cloud and land Elevation Satellite-2 (ICESat-2), launched in September 2018, to estimate changes in the height of grounded ice at seasonal timescales between April 2019 and June 2020. We found large increases in the surface height of the West Antarctic Ice Sheet during the 2019 austral winter (May–October), which occurred primarily due to higher rates of snowfall over the ice sheet during that period. Using outputs from atmospheric reanalysis models, we showed that nearly half of all increases in height during winter occurred due to snowfall delivered through extreme precipitation events—around half of these events were associated with landfalling atmospheric rivers, which are long and narrow bands of anomalously high moisture transport in the atmosphere. This study demonstrates how unambiguous measurements of changes in the snow surface using laser altimetry can be used to measure changes in snowfall over the ice sheet at seasonal and longer time scales, which can help reduce uncertainties in projections of sea level rise by improving the representation of snowfall in climate models.

Summary: These three studies show how satellite radar and laser altimeter data can be used to examine the large influence of changes in atmospheric and ocean conditions on processes affecting the Antarctic Ice Sheet at seasonal to interannual time scales. They provide new insights into the mass budget processes driving ongoing ice sheet change, and the techniques described here will help with the continued development of key observational datasets at continent-wide scales.

Future work: Future work in this research area would ideally focus on using satellite altimetry data to improve model projections of sea level rise. This is already possible using the datasets described in this dissertation; however, some advances in instrumentation and data processing to improve the accuracy, precision, and coverage of these data would increase their relevance further. First, improvements in the accuracy of height changes retrieved from radar altimeters could be possible through detailed analyses of the interactions between the radar signal and the snow surface. There has already been some progress toward this using data from airborne platforms; although power limitations on spaceborne platforms result in reduced precision of returns from the surface and subsurface, there is potential for extracting further information from satellite data using more advanced data processing techniques. The simultaneous operation of the ICESat-2 and CryoSat-2 satellite missions, together with the previous simultaneous operation of the ICESat and Envisat missions, will also help quantify the accuracy of height retrievals from radar altimetry. The accuracy of ice sheet mass changes estimated from height changes measured using radar and laser altimeters is ultimately limited by the accuracy of the firn models used to correct for surface processes over the ice sheet.

Therefore, any work towards improving the characterization of the ice surface using radar altimetry should be performed in conjunction with work towards improving firn models.

The rates of ocean-driven ice shelf melting described in Chapters 3 and 4 will be useful toward improving the representation of ice shelf melt in models and model parameterisations. However, because these data are only valid over ice shelf areas that are in hydrostatic balance, they are not yet available in grounding zones, where the ice sheet transitions from being fully grounded to freely floating. This is despite several studies that have showed that the accuracy of ice sheet models is disproportionally affected if there was large disagreement between observations and models in grounding zones compared to other ice shelf areas. Therefore, extending satellite-derived melt rate estimates into grounding zones using corrections for ice shelf flexure in those areas is of critical importance.

The ability of ICESat-2's laser altimeter to obtain seasonal measurements of changes at the snow surface across the entire ice sheet provides a unique opportunity to improve the treatment of snowfall over the ice sheet in the next generation of reanalysis and climate models. This is important because uncertainties in future snowfall and snowmelt are a major contributor to uncertainties in future sea level rise. Chapter 5 provides a demonstration of how ICESat-2 data can be used to evaluate the ability of models to represent surface height changes over the West Antarctic Ice Sheet. Studies such as these should be extended to the entire ice sheet in the future, and improvements in temporal sampling are also possible in the ice sheet interior where the altimeter has better coverage.

Finally, extensive field measurements are necessary to further validate all of the satellite-derived datasets described here, and to identify changes over the ice sheet occurring over the full range of spatial and temporal scales represented in the current generation of models.